Simulation Study of Self-Consistent Potential Formation in Edge Plasmas

LE THI QUYNH TRANG

Doctor of Philosophy

Department of Fusion Science
School of Physical Sciences
The Graduate University for Advanced Studies,
SOKENDAI

2022 School Year

Abstract

As they are lighter and have higher thermal velocities than ions, electrons are lost faster than ions on an open field line. The electric potential structure is self-consistently induced in the edge plasma by breaking the charge neutrality. In the edge plasma region where the L-H transition occurs, the radial electric field, E_r, affects ion losses and the $\mathbf{E} \times \mathbf{B}$ shear flow, which is necessary for the suppression of turbulence. Understanding the radial electric field is necessary to enable better control of the edge transport and to improve the core plasma confinement. There exists a strong relationship between the magnetic field and potential profile because particles move along the magnetic field line in magnetized plasma. The magnetic field affects the orbit of particle; in other words, it affects particle transport, and therefore, influences the formation of the potential. If the magnetic topology is externally changed, such as stochastic field, a responded electric field must be presented. Therefore, the electric potential structure is a key issue for elucidating the magnetic structure. Recently, in many fusion plasma experiment devices, probes have been used to measure the potential profile or radial electric field in the presence of a magnetic field. Through these experiments, the relation between the magnetic and electric fields has been summarized. However, theoretical and modeling works remain limited. Therefore, to better understand the relationship between the magnetic field and self-consistent potential structure, we need to develop a new theory and numerical code based on the fully kinetic description.

In this work, we developed a numerical code based on the particle-in-cell (PIC) method. The PIC model is a method where the fully kinetic model

description is used to model the electrical potential structure self-consistently. Unlike the fluid model, PIC simulation can deal with drift explicitly. To consider the effect of the magnetic field on the potential formation or the radial electric field, a PIC with two spatial dimensions and three velocity coordinates (2D3V) is necessary to account for the plasma behaviors. Instead of directly writing the 2D3V PIC code, we begin our work by developing the one spatial dimension and three velocity coordinates (1D3V) PIC code to verify the scale and performance of our PIC code. The 2D3V PIC code is an extension of the 1D3V code. Parallelization of the code is also included in our work to investigate the entire edge region.

It has been suggested that the magnetic field can affect the flux to the wall. The magnetic field changes the particle transport, which, in turn, influences the fluxes to the wall. Injecting current filaments can change the magnetic structure of the system, which influences the particle flux to the wall target. We applied our PIC model to study the effects of the external magnetic field generated from the current filaments on the particle and heat fluxes to the wall targets. In a one-dimensional consideration, where injecting the current filament is unrealistic, the external magnetic field is added by using the analytic function, which can produce the localized-reversed magnetic field, forming a magnetic mirror in the system. By performing the simulation using the 1D3V PIC model, we found that this localized reversed magnetic field traps the particles in the simulation domain and then reduces the particle and heat fluxes to the wall targets. Further, the reduction of fluxes originates from the particle reflection at the locations of the strongly localized magnetic field. Based on the modeling results, external localized-reversed magnetic fields can control the particle and heat fluxes to the wall under a one-dimensional consideration. To understand the effects of the external localized magnetic field in a more qualitative manner, in other words, the current filaments, we performed simulations using the 2D3V PIC model. The localized plasma flow enters the simulation box at the source region and is fully absorbed at the wall. We inject current filaments in the direction perpendicular to the simulation plane to change the magnetic field structure. A magnetic mirror is formed in between the current filaments. In comparison with the case where the current filaments were not injected, we found that the trapped electrons and ions in the magnetic mirror altered the particle and heat transport. Therefore, the high particle and heat fluxes to the wall are reduced and transferred along the wall. Consequently, injecting current filaments is a good option for reducing the high heat flux to the material. The mechanism of heat flux reduction arises from the reflection of particles in the magnetic mirrors and the expansion caused by the diffuse magnetic structure, regardless of the boundary condition at the wall. Each device has a different condition for the wall, which may not be the floating potential condition. These boundaries do not affect the tendency of flux reduction by the current filaments. These results can be applied for shielding high energy ion and electron fluxes to a divertor tokamak, satellites or spacecraft.

To study the relationship between the magnetic field and potential formation in the edge plasma, we used the 2D3V PIC code to model a flow of plasma consisting of ions and electrons on a boundary between closed and opened field lines. We considered a small region inside and outside the last closed flux surface (LCFS) to study the formation of the potential. The two dimensional slab geometry, which is a transfer of the torus configuration, was used in our work. For verifying the code and boundary conditions, two dimensional magnetic fields, including poloidal and toroidal magnetic fields were added initially. The magnetic field used in the slab geometry for modeling the magnetic field in the torus geometry contained the curvature and toroidal gradient. We found that the radial electric field has a tendency similar to that of the experimental results and theoretical prediction, which is negative and localized in the edge region and increases from the edge to the scrape-off layer (SOL) region. On changing the particle temperatures, their Larmor radii vary. Consequently, this is reflected in the change of the particle fluxes near the LCFS. The higher the temperature of the particles, the deeper is the negative potential at the closed magnetic field line region. We also determined that the asymmetry of the potential profiles depends on the values of the inverse aspect ratio. Starting from the system with a symmetric magnetic field, the potential structure becomes asymmetric for a larger inverse aspect ratio. These results provide a better understanding regarding potential formation by using the PIC simulation method, as compared with other numerical models; this is the advantage of using the PIC model in comparison with fluid models. After verifying the code, the radial magnetic field was added to prepare the magnetic islands in the simulation domain. In a slab geometry, it is difficult to ensure that the magnetic islands are identical to those in the torus. For simplicity, we added the current filaments into the simulation system to form the islands. The magnetic islands affect the potential formation through a change in the particle transport and resulting particle fluxes in the simulation. The size and shape of the magnetic island can be adjusted by the strength of the current filaments. The strengthened current forms the magnetic island more clearly, causing significant changes in the particle transport and fluxes near the islands. Therefore, the potential structure is largely modified under these effects. Further more, additional details regarding the stochastic boundary were studied, which means that some separatrices were overlapped. By injecting some nearby current filaments near the main island to create an overlap, we studied the effects of the stochastic field on the potential formation. The particle transport near these overlapped regions was changed. The particles were trapped in the magnetic island. Their movements were altered along both the radial and poloidal directions. The magnetic islands, finally, changed the potential in two dimensions.

In summary, we developed a PIC simulation to study the self-consistent formation of potential in edge plasmas. We applied the PIC simulation in a study on the reduction in heat flux to the material. We developed methods using the localized-reversed magnetic field or current filaments, which serves as a good candidate to reduce the burden of high heat fluxes to the wall. The relationship between potential formation and magnetic field is presented. This is the initial prior work for the research on potential formation in edge plasmas using PIC simulation. This is an important result that provides a deeper understanding of the relationship between potential formation and magnetic fields in edge plasmas.

Contents

List of Figures

List of Tables

Chapter 1

Introduction

1.1 Overview

In an open magnetic field line, highly energetic particles leave the confined plasma and collide with the surrounding wall. The impurities and neutrals from the first wall may be extracted and enter the core region. This process will reduce the performance of the fusion devices. The plasma core should be separated from the first wall as far as possible for achieving high plasma confinement. From the core to the first wall, the magnetic field line changes from a closed field line to an open field line. This topological change makes the physics properties of particle transport in the plasma edge complicated.

Usually, in the edge of the fusion plasma the magnetic field lines are opened. If the fusion plasma on the closed magnetic field line directly touches the first wall of the device, many impurities and neutrals from materials of the first wall come into the fusion plasma. The radiative interaction between fusion plasma and impurities cools down the temperature of the fusion plasma. That means the fusion reaction rate is reduced. To avoid that, the magnetic field should be diverted from the first wall. Therefore, the physics in the plasma edge is very complicated because the magnetic topology changes from the closed field line to open field lines with a small spatial scale. To understand the physics in the plasma edge, sophisticated experimental and theoretical studies are necessary. In the magnetically confined fusion, high-energy ions and electrons are confined by the magnetic field because charged particles move along the magnetic field lines with the gyro motion. The magnetic configuration plays an important role in the particle transport. The movement of the plasma flow may be affected if the magnetic structure changes.

1.2 Magnetic field and particle transport in the edge plasma

In the straight magnetic field line system, particle transport parallel to the magnetic field is the dominant component, forcing the particles to hit the surrounding wall. Once the magnetic structure changes, the trajectory of a particle changes. The magnetic field can uniformly change in space, or form magnetic islands and stochastic fields. One of the examples for a non-straight magnetic field line in the tokamak is the resonant magnetic perturbations (RMPs) which is generated by the perturbation coils. The RMP fields are applied into the edge to stabilize plasmas with high energy confinement with respect to edge-localized modes (ELMs) [1]. It has been demonstrated that the RMPs have a close relation with the particle transport in the edge [2, 3, 4]. When the overlapping magnetic islands appear, particles move from one stochastic region to another. This transaction affects the radial component of the edge electric field, E_r, [2, 5, 6]. The sign of the radial magnetic field may change in the presence of the stochastic field or the magnetic island [7]. The stochastic magnetic field also has strong impact on the parallel and perpendicular flow of particles [8]. Created by the stochastic magnetic field, the perpendicular ion flux is more important than the parallel ion flow.

The transport of particles becomes different once the magnetic field is altered. The particle orbit change associated with the change of magnetic field leads to the change of particle flux in the edge region. The formation of potential or the radial electric field in the edge also changes. The radial electric field plays an important role in understanding the edge plasma physics. Because of unequal particle losses between electrons and ions in the open field line due to unbalance of mass and thermal velocity, the radial electric field is self-consistently induced in the edge region. The radial electric field is related with the edge transport. In the presence of the radial electric field, an ion is only trapped when the parallel velocity of the ion is sufficient large to cancel the electric field drift. Therefore, the number of trapped ions is reduced with the increase in the radial electric field [9]. The radial electric field also affects the $\mathbf{E} \times \mathbf{B}$ shear flow [10, 11, 12]. Once E_r is sufficiently strong, the poloidal $\mathbf{E} \times \mathbf{B}$ flow acquires a large shear. This shear not only is necessary for suppression of the edge turbulence by decorrelation but also helps to reduce the losses of both energy and particles across the magnetic field line. Understanding the radial electric field helps to generate a better ideas for controlling the edge plasma transport and improving the core plasma confinement.

Particle motion depends on the magnetic field configuration. The magnetic field affects particle transport, and changes the formation of the potential. If the topology of the magnetic field is externally changed, the potential must be reflected. Therefore, the magnetic field has a strong relationship with the potential formation or the radial electric field. Various studies have been conducted on the relationship between the radial electric field (or potential profile) and the stochastic magnetic field. In the experimental works, emissive probes and heavy ion beam probes are mainly used to measure the potential profile or radial electric field in the presence of the magnetic field. In these experiments, the relation between the magnetic field and electric field was summarized [13, 14, 15, 16]. The potential profile in the presence of the stochastic field was measured in the Texas Experimental Tokamak (TEXT) using heavy ion beam probes [17]. In this work, the applied perturbing magnetic fields were produced by using the saddle coils of the ergodic magnetic limiter (EML). The perturbing magnetic fields increased linearly with increasing saddle coil current, producing magnetic islands. Both the radial electric field and potential profile were found to be increased at the edge. By increasing the perturbing current, the region where the potential profile was positive was expanded. In the Large Helical Device (LHD), Kamiya and his group used the charge exchange recombination spectroscopy diagnostic to determine the radial electric shear [14]. It was found that the region where the radial electric field shear became strong corresponded to the stochastic field. The losses of electrons in the ergodic layer for various magnetic configurations might be different because of the variation in the connection length of the magnetic field. This difference leads to the positive potential profile in the scrape-off layer (SOL) region.

Numerical simulation of the edge plasma is very important for understanding the physics behaviors in this region. In numerical studies, the fluid and kinetic models are widely used for studying the edge plasma. Rozhansky st al. used the fluid model to compute the radial electric field in the presence of the RMPs in the MAST L-mode [18]. In their work, they tried to add the electron radial current and considered the $\mathbf{E} \times \mathbf{B}$ drift to compute the radial electric field E_r. Some studied used magnetohydrodynamics (MHD) codes where the screening of the perturbed magnetic field might take place [19, 20, 21]. However, the radial electric field in these codes was not self-consistently computed [18]. Takizuka's group developed the PARASOL package, which used the kinetic model for studying the SOL region [22, 23, 24, 25]. The PARASOL code is fundamentally a time-dependent electrostatic particle-in-cell (PIC) code employing a binary collision model [22]. In this code, they used the guiding center motion equations for the electrons and the kinetic equations for the ions. The PARASOL is a good model to reproduce the SOL flow precisely, but it does not consider the effect of the radial electric field.

In the previous numerical works, the relationship between the potential formation and the magnetic field in the edge plasma has not been clearly proposed. Due to the code limitations, the transport model cannot include the drift effects or deal with a small scale length. It is necessary to develop a completely new numerical code for studying the self-consistent potential formation in the edge plasma. In this new code, the electric field or the potential structure must be self-consistently calculated. The relationship between magnetic field and potential formation should be clearly proposed in this new model. Drift and Larmor motion play important roles in driving particle transport. Therefore, the effects of drifts and Larmor radius on particle motion can be easily shown using this new model.

1.3 Magnetic field and heat flux reduction

The magnetic field plays an importance role in plasma confinement and transport. In spacecraft propulsion with plasma thruster and magnetic nozzle, which constitute the converging-diverging magnetic field that guides and accelerates plasma into vacuum, thrust is generated through transformation of thermal energy in the plasma into kinetic energy [26, 27]. In fusion plasma, the closed magnetic field lines help to shape and confine the plasma in the desired region, while the open lines lead the particles to escape from the core region [28, 29].

In those devices, the behavior of high energetic particles is one of the important topics for research. In satellites or spacecraft, the high energetic ions may lead to a single event upset and single event latch-up in the space electronic system, which can cause software faults and damages the device [30]. High energy electrons can penetrate satellites and spacecraft, and accumulate a charge on the surfaces of the conductor. A higher rate of penetration causes internal charging and discharging pulses, and finally damages the electronic systems or causes failure of various spacecraft components [30, 31, 32]. Therefore, high energy particles may damage material surfaces, or deposit harmful charges into electronic components. Several methods have been proposed for shielding the spacecraft and satellites from high energy particles, such as active shielding, a chaotic magnetic field, or multi-layer shielding [33].

Reduction of the high energy particles reaching the wall is also a critical issue in fusion engineering. Particles move along the magnetic fields in the divertor leg to hit the divertor plates, and then, particle fluxes are localized on a small region in the divertor targets [34]. These high heat fluxes damage the material of the divertor plates. The question is how to reduce these high heat fluxes to minimize the damage as much as possible [35, 36]. In recent studies, various approaches have been proposed, such as the radiating divertor and RMPs. They have been proposed for reducing the heat flux to the divertor [37, 38]. These methods are powerful techniques to reduce the high energy fluxes to the material; however, they still have some remaining limitations related with technical challenges or physical issues [33, 39, 38]. Some experimental results found that RMPs can be effective to suppress or mitigate the edge-localized models (ELMs) in the tokamak and control the edge plasma transport [40, 41, 42]. The idea comes from the effects of the magnetic field on the transport of particles. The magnetic field affects the change in particle transport which, therefore, changes the potential structure in the SOL region, and then influences the fluxes to the divertor. The Experimental Advanced Superconducting Tokamak (EAST) has proposed the possibility of injecting current filaments, which can change the magnetic field, and then can reduce the particle and heat fluxes to the divertor [43, 44]. Starting from the idea of high heat flux reduction in fusion plasma, we aimed to find a solution that can be applied for shielding spacecraft and satellite from high energy particles.

1.4 Objective

Based on these main necessary conditions, we aim to develop a completely new numerical PIC code, which uses fully kinetic description. The PIC simulation can solve the electrical potential structure self-consistently under a given magnetic field and initial and boundary conditions, and can deal with drift explicitly in comparison with the fluid model. PIC simulation is a useful and powerful tool for the numerical study of plasma physics. Many numerical studies have used PIC simulation for research on fusion [22, 45] and space [46, 47, 48]. We developed a PIC code to study the control of high energy flux to the wall. We propose a solution for high heat flux reduction which can be applied in satellite, spacecraft, and fusion studies using current filaments. This PIC code can also be used to study the self-consistent potential formation in the edge plasma. We study the relationship between the magnetic field and potential formation in the edge plasma. The effects of drifts and

Larmor motion on particle transport are considered in our work. Our PIC simulation code can solve all the requirements presented in previous sections. In this our work, the self-consistent potential, drifts, and Larmor motions are included. These considerations distinguish our work from previous studies on the edge plasma. Our research does not use any experimental data or parameters of any real devices, but is a fundamental research using PIC simulation to understand the plasma physics in the edge plasma. It provides a basic explanation for the study of a complex phenomenon.

1.5 Outline

In our work, we develop a numerical code based on the PIC method. The PIC model is a method that uses a fully kinetic model description to solve the electrical potential structure self-consistently. Our work focuses on studying the formation of potential in the poloidal cross section of the edge region, where the radial and poloidal transports are mainly discussed. To this end, a PIC with two spatial dimensions and three velocity coordinates (2D3V) is necessary. The two spacial dimensions correspond to the radial and poloidal directions. All three components of velocity are included to compute the particle orbit exactly and satisfy energy conservation accurately. This 2D3V PIC code is a verification for studying the effects of the three dimensional magnetic field (radial, poloidal, and toroidal magnetic field) on potential formation. Because the boundary conditions and purposes are different, our code is a completely new developed PIC code, which is not based on any present codes. Therefore, to develop a 2D3V PIC code that can precisely simulate the edge region, we started by programming the one dimension and three velocity coordinates (1D3V) PIC code. Then, the 2D3V code was extended based on the 1D model. The reason why the 2D3V code was not directly developed was that we wanted to ensure that the code ran correctly. Therefore, the step-by-step development was an easier way for verifying the performance of the code. PIC simulation is a powerful tool for simulation, but because it solves the simulation domain in a very small time step and space grid scale, PIC requires huge computer memories and consumes a large amount of time for running. To improve these points, code parallelization was applied to optimize the code for application in the study of the entire edge plasma region. The details of how PIC simulation works is provided in Chapter 2. The basic equations that have been used in the simulation are mentioned in this chapter.

The story of our code development is presented in the last chapters.

At the beginning, as mentioned before, we started by developing the 1D3V PIC code. Here, we applied our 1D3V code in studying the control of particle and heat fluxes to the target using the external magnetic field. This part is presented in Chapter 3. The localized-reversed external magnetic field is added, forming the strong magnetic mirrors. The magnetic mirrors trap the particles in the simulation domain. The particle flux to the target, subsequently, is reduced by using the external field.

From the 1D3V code, an expansion to a 2D code is proposed in Chapter 4. The control of particle and heat fluxes is still discussed in this chapter. For the two dimensional consideration, current filaments are injected in the simulation domain instead of using a reversed-localized external magnetic field, as in the one dimensional view. The details of how current filaments reduce the high heat fluxes to the target are presented in this chapter.

Having the 2D3V PIC code, parallelization and verification of the code are added to study the edge region. In the edge region, the magnetic field has radial, poloidal and, toroidal components. Once the radial magnetic field is assumed to be zero, only the poloidal and toroidal magnetic fields are considered (2D magnetic field). The parallel transport becomes the dominant in the system. Perpendicular or radial transport might occur in the presence of drift effects or collisions. We studied how the 2D magnetic field affects the particle transport and potential formation, as presented in Chapter 5. In this Chapter, the effects of grad-B drift and Larmor radius on the formation of potential is discussed.

Adding radial components to the magnetic field, the magnetic island is realized in the simulation region. In this simulation, the three components of the magnetic field were taken into account (3D magnetic field). Chapter 6 shows how to form the magnetic island in the simulation. The relationship between magnetic island or stochastic field and formation of potential is proposed in this chapter.

The discussion and conclusions are presented in Chapter 7.

Chapter 2

Method

2.1 Outline of particle-in-cell (PIC)

Particle-in-cell (PIC) simulation is a model developed based on the idea of chasing the motion of each individual charged particle to simulate the behavior of plasma [49, 50]. Because the number of particles in the real plasma is extremely large, it is impossible to store all the information of the real particles in any computer memory. PIC uses the concept of super-particle which

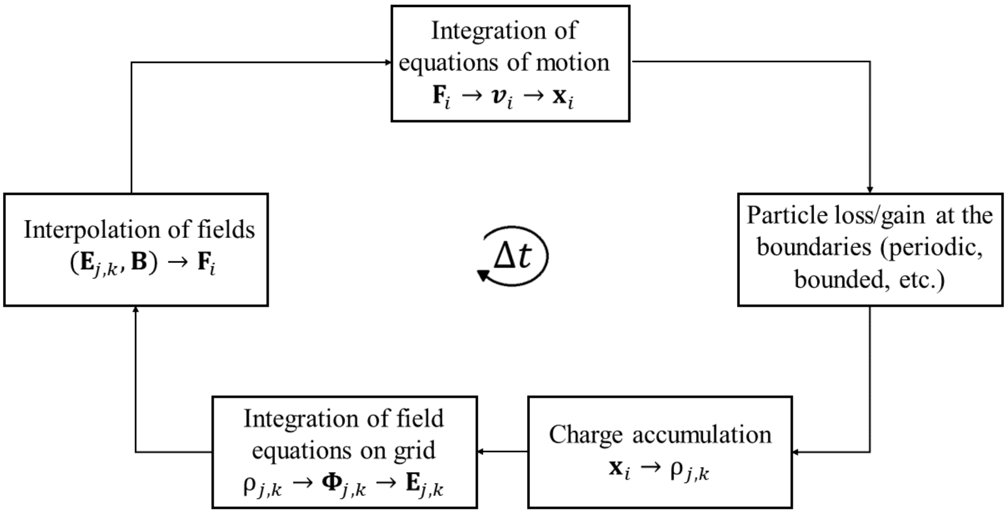

Figure 2.1: Schematic diagram of particle-in-cell (PIC) Simulation

is a group of single particles, to reduce the memory size of the computer. The number of simulated particles is reduced while the statistical properties of the plasma are still satisfied. The PIC model also proposes the concept of a spacial grid on which the fields are calculated. The spatial grid is usually sufficiently small to resolve a Debye length in order to measure the charge density and calculate the electric field precisely. The PIC simulation tracks the trajectory of the simulated particles by solving a collection of differential equations. The process of the simulation in each time step Δt is shown in Figure 2.1. The PIC cycle starts by assigning the initial values of positions and velocities for the particles. The loss or gain of the particles is estimated based on the boundary conditions of the system. Next, the charge density on the grid is calculated using the weighting method to link the particle position with the nearest grid points (NGPs). Once the charge density is accumulated, the electric field and potential profile are obtained by solving the Poisson's equation. The fields are interpolated from the grids to the particles to compute the force acting on each particle, and then the velocity and position of particle are updated to move to the new position with the new velocity.

The basic equations for the dynamics of the plasma used in PIC simulation consist of two main groups of equations. These are the motion and field equations. The equations of motion to be used separately for each particle are

$$\frac{\mathrm{d}\mathbf{x}}{\mathrm{d}t} = \mathbf{v} \tag{2.1}$$

and

$$m\frac{\mathrm{d}\mathbf{v}}{\mathrm{d}t} = q(\mathbf{E} + \mathbf{v} \times \mathbf{B}), \tag{2.2}$$

where $\mathbf{x}$, $\mathbf{v}$, q, and m are the position, velocity, charge and mass of the particle, respectively. $\mathbf{E}$ and $\mathbf{B}$ represent the electric and the magnetic fields, respectively. The field equations are given as

$$\mathbf{E} = -\nabla\phi \tag{2.3}$$

and

$$\nabla \cdot \mathbf{E} = \frac{\rho}{\epsilon_0}, \tag{2.4}$$

which are combined to obtain *Poisson's equation*

$$\nabla^2\phi = -\frac{\rho}{\epsilon_0}, \tag{2.5}$$

where ϕ and ρ are the electric potential and charge density, respectively.

In the code, all of the parameters are normalized as follows:

$$\begin{aligned}
\hat{\mathbf{x}} &\leftarrow \frac{\mathbf{x}}{\lambda_{De0}}, \\
\hat{t} &\leftarrow \omega_{pe0}t, \\
\hat{v} &\leftarrow \frac{v}{v_{e0}}, \\
\hat{q} &\leftarrow \frac{q}{e}, \\
\hat{m} &\leftarrow \frac{m}{m_e}, \\
\hat{\mathbf{E}} &\leftarrow \frac{e\mathbf{E}}{m_e\omega_{pe0}v_{e0}}, \\
\hat{\mathbf{B}} &\leftarrow \frac{e\mathbf{B}}{m_e\omega_{pe0}}, \\
\hat{\rho} &\leftarrow \frac{\rho}{n_0 e}, \\
\hat{\phi} &\leftarrow \frac{e\phi}{m_e v_{e0}^2},
\end{aligned} \tag{2.6}$$

where $\lambda_{De0} = \left(\frac{\epsilon_0 kT_{e0}}{n_0 e^2}\right)^{1/2}$, $\omega_{pe0} = \left(\frac{n_0 e^2}{\epsilon_0 m_e}\right)^{1/2}$, $\omega_{ce0} = \frac{e\mathbf{B}}{m_e}$, and v_{e0} are the Debye length, plasma frequency, cyclotron frequency, and thermal velocity, respectively. e, m_e, and n_0 are the electric charge, mass, and density of electrons, respectively.

In this work, the electrostatic PIC code is studied, in which the electric field is self-consistently solved and the magnetic field is constant in time. The positions and velocities of the particles may take all the values in the $\mathbf{x}$ and $\mathbf{v}$ space. The field quantities will be obtained on the spacial grids, known only at the discrete points in the space labeled with index j and k, such as $\mathbf{E}_{j,k}$. Ngx and Ngy are the number of grids, and L_x and L_y are the system length in the x and y directions, respectively. The name of the particles is given by the index i. The indexes j and k are the grid points, and $\Delta x = L_x/Ngx$ and $\Delta y = L_y/Ngy$ are the spacial grid sizes in the x and y directions, respectively.

2.2 Integration of equations of motion

The motion equations can be replaced by the finite-difference equations [49]

$$m\frac{\mathbf{v}_{new}-\mathbf{v}_{old}}{\Delta t}=\mathbf{F}_{old}, \tag{2.7}$$

$$\frac{\mathbf{x}_{new}-\mathbf{x}_{old}}{\Delta t}=\mathbf{v}_{new}, \tag{2.8}$$

where $\mathbf{F}$ is the Lorentz force given as $\mathbf{F}=q(\mathbf{E}+\mathbf{v}\times\mathbf{B})$. The flow in time and notation is shown in Figure 2.2, in which the time-centering technique is displayed. First, the center-difference for the Newton equations of motion can be re-written as

$$m\frac{\mathbf{v}(t+\Delta t/2)-\mathbf{v}(t-\Delta t/2)}{\Delta t}=q\left(\mathbf{E}+\frac{\mathbf{v}(t+\Delta t/2)-\mathbf{v}(t-\Delta t/2)}{2}\times\mathbf{B}\right). \tag{2.9}$$

The simulation will advance $\mathbf{v}(t-\Delta t/2)$ to $\mathbf{v}(t+\Delta t/2)$ and $\mathbf{x}(t)$ to $\mathbf{x}(t+\Delta t)$. This leap-frog scheme showing time-centering of position and velocity is illustrated in Figure 2.2. The leap-frog method is used in PIC simulation because it is simple to develop and quite accurate when dealing with a large number of of particles. The explicit Boris rotation is a good candidate to solve these different equations [51]. Boris [49] separated the forces from the electric and magnetic fields completely, by substituting

$$\begin{aligned}\mathbf{v}(t-\Delta t/2)&=\mathbf{v}^{-}-\frac{q\mathbf{E}(t)}{m}\frac{\Delta t}{2},\\ \mathbf{v}(t+\Delta t/2)&=\mathbf{v}^{+}+\frac{q\mathbf{E}(t)}{m}\frac{\Delta t}{2}.\end{aligned} \tag{2.10}$$

into Eq. 2.9. The $\mathbf{E}$ term is canceled, yielding

$$\frac{\mathbf{v}^{+}-\mathbf{v}^{-}}{\Delta t}=\frac{q}{2m}(\mathbf{v}^{+}+\mathbf{v}^{-})\times\mathbf{B}, \tag{2.11}$$

which is a rotation of $\mathbf{v}^{-}$ to $\mathbf{v}^{+}$ by the angle of rotation θ where

$$\left|\tan\frac{\theta}{2}\right|=\frac{q\mathbf{B}}{m}\frac{\Delta t}{2}=\frac{\omega_c\Delta t}{2}, \tag{2.12}$$

and $\omega_c=\dfrac{q\mathbf{B}}{m}$ is the cyclotron frequency. Equation 2.11 produces a rotation through the angle θ, which has less than 1% error for $\omega_c\Delta t<0.35$. When

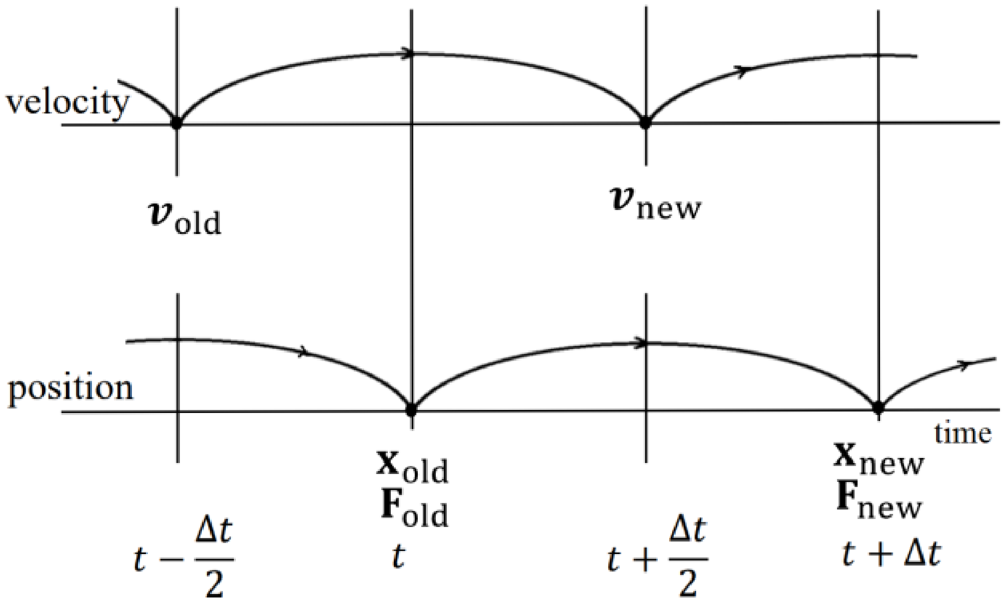

Figure 2.2: Leap-frog method to update positions and velocities

the directions of $\mathbf{B}$ and $\mathbf{v}^-$ are arbitrary, the $\mathbf{v}^+$ can be incremented by the geometry projection on the perpendicular to $\mathbf{B}$, given as

$$\begin{aligned} \mathbf{v}^{'} &= \mathbf{v}^- + \mathbf{v}^- \times \mathbf{t}, \\ \mathbf{v}^+ &= \mathbf{v}^- + \mathbf{v}^{'} \times \mathbf{s}, \end{aligned} \tag{2.13}$$

where $\mathbf{t} = \dfrac{q\mathbf{B}\Delta t}{2m}$ and $\mathbf{s} = \dfrac{2\mathbf{t}}{1 + \mathbf{t}^2}$, respectively. After accelerating the velocity, the particle position can be updated as

$$\frac{\mathbf{x}(t + \Delta t) - \mathbf{x}(t)}{\Delta t} = \mathbf{v}(t + \Delta t/2). \tag{2.14}$$

2.3 Particle and force weighting

The charge density on the discrete grid points from the continuous particle positions can be computed using the weighting method. The same weighting is used for both density and force calculations to avoid a self-force [49]. In the two-dimension system, the area weighting method has been used owing to its geometric interpretation, as shown in Fig. 2.3. The weighting function W_m (where $m = 1, 2, 3, 4$) is the area of each particular region, defined as

$$\begin{aligned} W_1 &= \frac{(\Delta x - (x_i - X_j))(\Delta y - (y_i - Y_k))}{\Delta x \Delta y}, \\ W_2 &= \frac{X(\Delta y - (y_i - Y_k))}{\Delta x \Delta y}, \\ W_3 &= \frac{(\Delta x - (x_i - X_j))(y_i - Y_k)}{\Delta x \Delta y}, \\ W_4 &= \frac{(x_i - X_j)(y_i - Y_k)}{\Delta x \Delta y}, \end{aligned} \tag{2.15}$$

where $X_j = j\Delta x$ and $Y_k = k\Delta y$. x_i and y_i denote the position of the particle in the x and y directions, respectively. The charge density ρ at the NGPs, thereafter, is computed as

$$\begin{aligned} \rho_{j,k} &= \rho_{cell} W_1, \\ \rho_{j+1,k} &= \rho_{cell} W_2, \\ \rho_{j,k+1} &= \rho_{cell} W_3, \\ \rho_{j+1,k+1} &= \rho_{cell} W_4, \end{aligned} \tag{2.16}$$

where $\rho_{cell} = \dfrac{q}{V_{cell}}$ is the charge density in a cell, in which the volume of a cell is defined as V_{cell}. The field weighting operates in the same manner. The force acting on each particle coming from the field at the NGPs can be computed as in the charge accumulation. For a particle at (x_i, y_i), the electric field is given as

$$\mathbf{E}(x_i, y_i) = \mathbf{E}_{j,k} W_1 + \mathbf{E}_{j+1,k} W_2 + \mathbf{E}_{j,k+1} W_3 + \mathbf{E}_{j+1,k+1} W_4. \tag{2.17}$$

2.4 Integration of field equations on grid and boundary conditions

Once the charge density ρ is known at all of the grid-points, the electric potential ϕ can be obtained by solving the Poisson's equation (Eq. 2.22). However, the boundary conditions are necessary for solving the Poisson's

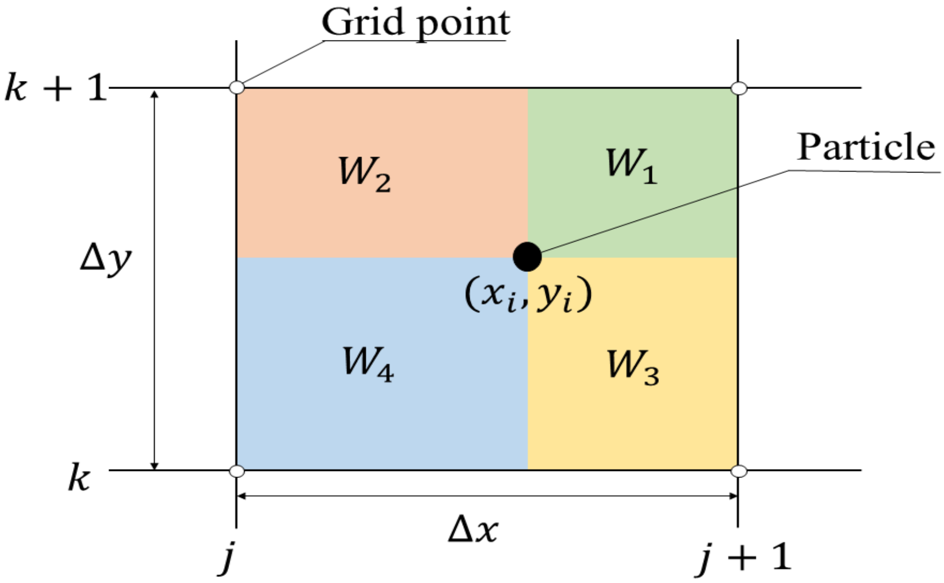

Figure 2.3: Area weighting method

equation. In a bounded (non-periodic) system, the charge accumulated on the grid point at the boundary is only half of the charge accumulated at the grid point that is not at the boundary if the physical charge density is the same at these two points [49, 52]. σ_L and σ_R are the surface charge densities at the left-hand side and the right-hand side boundaries, respectively, which are given as

$$\begin{aligned} \sigma_L &= \epsilon_0 E(0), \\ \sigma_R &= -\epsilon_0 E(L). \end{aligned} \tag{2.18}$$

According to the Gauss's law, the electric field at the boundary becomes

$$E(L) - E(0) = \frac{1}{\epsilon_0}\int_0^L \rho(\mathbf{r})\mathrm{d}\mathbf{r}, \tag{2.19}$$

in which

$$\int_0^L \rho(\mathbf{r})\mathrm{d}\mathbf{r} + \sigma_{\mathrm{L}} + \sigma_{\mathrm{R}} = 0. \tag{2.20}$$

The total charge of the system including the boundaries is zero. Using the idea of conservation of total electrostatic energy in the system in any choice of the reference potential, the Poisson's equation at the boundary is

$$\begin{aligned} \frac{\phi_0 - \phi_1}{\Delta r} &= \frac{1}{\epsilon_0}\left(\sigma_L + \frac{\rho_0}{2}\Delta r\right), \\ \frac{\phi_N - \phi_{N-1}}{\Delta r} &= \frac{1}{\epsilon_0}\left(\sigma_R + \frac{\rho_N}{2}\Delta r\right), \end{aligned} \tag{2.21}$$

where N is the number of grids in the $\mathbf{r}$ direction.

The potential in the simulation except at the boundaries can be computed by the Poisson's equation, which is written in finite-difference form as

$$\frac{\phi_{j-1,k} - 2\phi_{j,k} + \phi_{j+1,k}}{\Delta x^2} + \frac{\phi_{j,k-1} - 2\phi_{j,k} + \phi_{j,k+1}}{\Delta y^2} = -\frac{\rho_{j,k}}{\epsilon_0}. \tag{2.22}$$

Multiplying Eq. 2.22 with Δx^2, we obtained

$$\Phi_{j+1,k} + \Phi_{j-1,k} - 2(1+\beta^2)\Phi_{j,k} + \beta^2(\Phi_{j,k+1} + \Phi_{j,k-1}) = -\frac{\Delta x^2}{\epsilon_0}\rho_{j,k}, \tag{2.23}$$

where $\beta = \dfrac{\Delta x}{\Delta y}$. Equation 2.22 is written in the matrix form as

$$\begin{bmatrix} D & I & & & \\ I & D & I & & \\ & \ddots & \ddots & \ddots & \\ & & \ddots & \ddots & \ddots \\ & & & I & D \end{bmatrix} \begin{bmatrix} \Phi_{j,0} \\ \Phi_{j,1} \\ \vdots \\ \vdots \\ \Phi_{j,Ngy-1} \end{bmatrix} = \begin{bmatrix} d_{j,0} \\ d_{j,1} \\ \vdots \\ \vdots \\ d_{j,Ngy-1} \end{bmatrix}, \tag{2.24}$$

where $\mathbf{I}$ is the identity matrix, and the matrix D is given as

$$\text{D=} \begin{bmatrix} -2(1+\beta^2) & \beta^2 & & & \beta^2 \\ \beta^2 & -2(1+\beta^2) & \beta^2 & & \\ & \ddots & \ddots & \ddots & \\ & & \ddots & \ddots & \ddots \\ \beta^2 & & & \beta^2 & -2(1+\beta^2) \end{bmatrix}. \tag{2.25}$$

The matrix in the right-hand side of Eq. 2.24 is

$$\begin{aligned} d_{j,k} = -\frac{\Delta x^2}{\epsilon_0}\rho_{j,k}, \quad &\text{and} \quad d_{j,Ngy-1} = -\frac{\Delta x^2}{\epsilon_0}\rho_{j,Ngy-1} - \Phi_{Ngx}, \\ \forall_{j,k} \quad : \quad j = 1, 2, \ldots, Ngx-1; \quad &\text{and} \quad k = 0, 1, \ldots, Ngy-1. \end{aligned} \tag{2.26}$$

Equation 2.24 is solved using successive-over relaxation (SOR) method. The residual $Res(j,k)$ at the node (j,k) is defined as

$$Res^m_{j,k} = \frac{\Phi_{j+1,k} + \Phi_{j-1,k} - 2(1+\beta^2)\Phi_{j,k} + \beta^2(\Phi_{j,k+1} + \Phi_{j,k-1}) + \frac{\Delta x^2}{\epsilon_0}\rho_{j,k}}{2(1+\beta^2)}. \tag{2.27}$$

The value of the residual at the m^{th} iteration, denoted by $Res^m_{j,k}$, is the correction which is added to $\Phi_{j,k}$ to make $\Phi_{j,k}$ near to the correct value as

$$\Phi^{m+1}_{j,k} = \Phi^m_{j,k} + \omega Res^m_{j,k}. \tag{2.28}$$

The parameter ω, which is the relaxation factor and lies between 1 and 2, helps to improve the rate of convergence. Once the $Res^m_{j,k}$ tends to zero, the values of potential is achieved.

The electric field $\mathbf{E}$ is obtained from the electric potential ϕ as

$$E_{x,j,k} = \frac{\phi_{j-1,k} - \phi_{j+1,k}}{2\Delta x}, \tag{2.29}$$

and a similar differential equation for E_y.

2.5 Parallel particle-in-cell (PIC)

To study the whole edge region, parallel programming is necessary for reducing the computation time and memory size of the computer. The two main strategies often applied for parallel computing are particle decomposition and domain decomposition. Particle decomposition distributes the particles among the processes while assigning the entire domain for each process. Domain decomposition divides the simulation box into smaller regions, which will be assigned for each process. For a large system length, as that in this study, domain decomposition is a better choice for parallel computing. In this work, the domain is divided into equally small regions. Communication between each process for pushing the particle into a different domain is required. The Poisson's equation is solved in each small domain, and the time consumed for the field solver is shorter when using a large number of processes. Figure 2.4 shows the dependence of computation time for solving

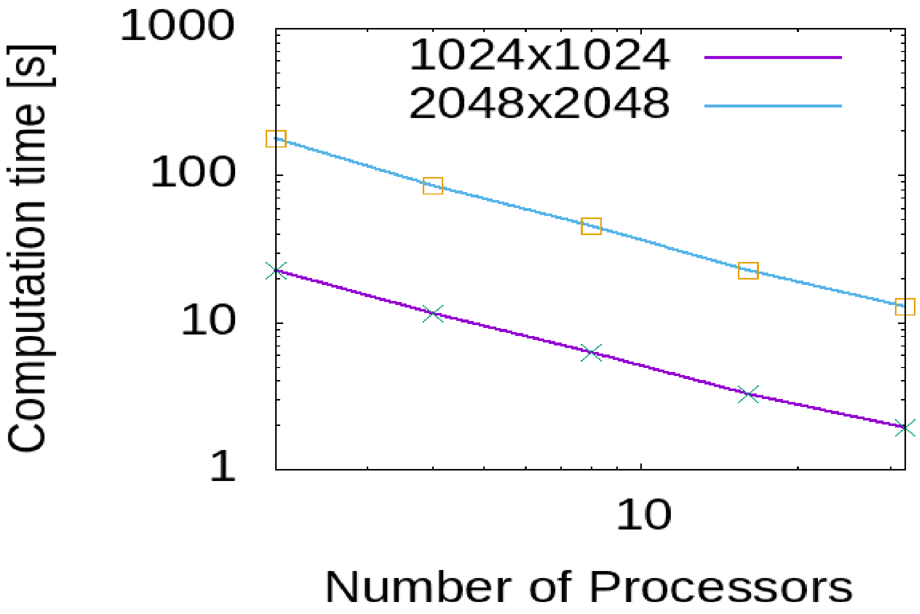

Figure 2.4: Computation time for solving Poisson's equation using successive-over relaxation (SOR) method with different number of processes.

Poisson's equation using the SOR method by using different number of processes for 1024×1024 and 2048×2048 grids. The computation time reduces when using a higher number of processes while using the same residual value for tolerance $R_{res} = 1.0 \times 10^{-7}$.

Chapter 3

Controlling the particle and heat flux to the wall by external magnetic field

3.1 Introduction

High heat flux reduction is one of the critical issues in the study of plasma physics and space discovery. It has been suggested that the magnetic field can affect the transport of particles, and then control the particle flux to the wall. The current filament is injected in the EAST tokamak devices. There is a possibility of heat flux reduction by using the current filament. High energy particles are also a big issue in satellites and spacecraft. We aimed to study a method to shield the satellites and spacecraft from high high energetic particles based on the idea of heat flux reduction in fusion plasma.

We propose a new solution to control the particle flux by using the external magnetic field. In one-dimensional consideration, the external magnetic fields is added in the y direction, which is perpendicular to the plasma flow, by using an analytic function. This analytic function creates the localized-reversed magnetic field that can produce the magnetic mirrors in the system. The direction of the external magnetic field is switched at the strongest magnetic field locations. The plasma enters from the left side (i.e., the source region) and is absorbed at the right side (i.e., the conductor wall) of the simulation. This chapter shows how the localized-reversed magnetic field changes the particle and heat fluxes using the 1D3V PIC simulation model.

3.2 Simulation model

We study a small simple region, as in linear devices. The plasma comes from the upstream region and is fully absorbed at the downstream region [53, 54]. The electrostatic PIC is used in this simulation in which the magnetic field is constant in time and the electric field is self-consistently computed. The simulation length was set to be $L_x = 0.1\,\mathrm{m}$ from the source to the conductor wall. $x = 0$ is defined as the source region where plasma is injected into the simulation domain, and $x = L_x$ is the conductor wall where particles are absorbed. We consider only ions and electrons. No neutral particle has been taken into account. This work does not include any collision process between particles. The background magnetic field $\mathbf{B}$ is in the x (i.e., the direction toward the wall) and z (i.e., the direction is perpendicular to the plasma flow and the wall) directions. The magnetic field in these directions, B_x and B_z, is assumed to be constant in time and space.

The system begins free of plasma. There is no particle in the system at the initial stage. Particles are injected during each time step Δt of the simulation around $x = 0$. Being lighter and having higher thermal velocity than the ions, electrons move faster than ions. To satisfy the charge neutrality at the source boundary, we assumed that the particle density at $x = 0$ is always constant in time. The electron density is set to be equal to the ion density in this boundary. The velocities of injected ions and electrons follow the Maxwellian distribution function, which satisfies $v_{||} > 0$. We perform the simulation using the following parameters: ion-electron mass ratio $m_i/m_e = 1836$, electron source temperature $T_{\mathrm{e}0} = 100\,\mathrm{eV}$, ion source temperature $T_{\mathrm{i}0} = 50\,\mathrm{eV}$, the magnetic field $B_x = 0.2\,\mathrm{T}$, and small magnetic field $B_z = 0.02\,\mathrm{T}$. On the right boundary at $x = L_x\,\mathrm{m}$, the wall is assumed to

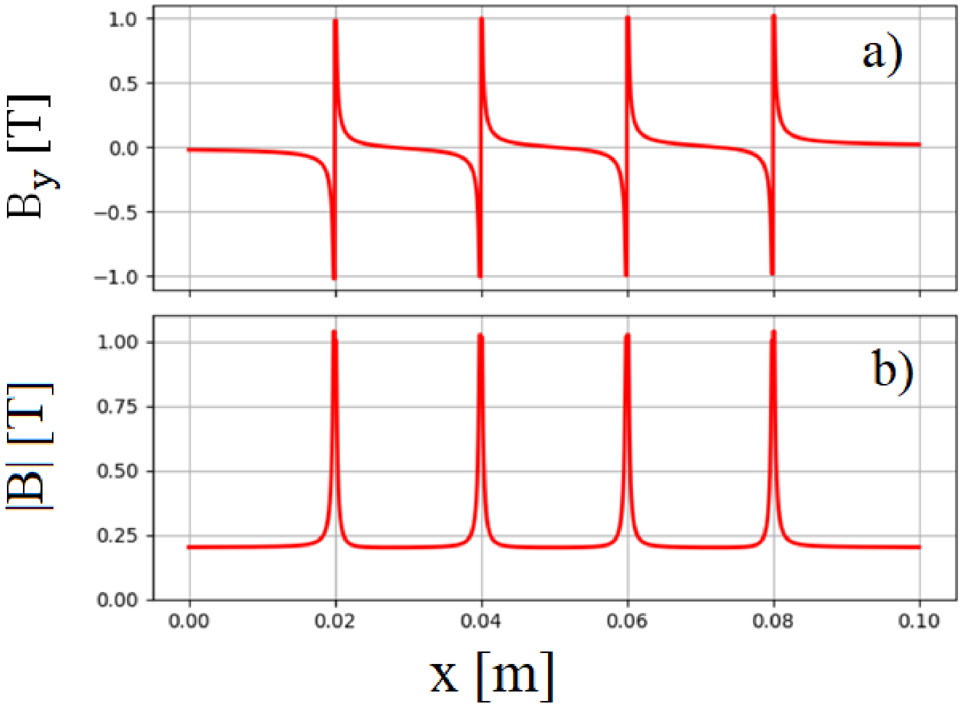

Figure 3.1: a) Analytic function of external magnetic field in y direction and b) absolute value of total magnetic field after adding the external magnetic field in the system. The direction of B_y is opposite at four "imaginary points." By inputting new magnetic fields, four strong magnetic mirrors are formed in the simulation domain.

satisfy the floating potential condition in which particles are fully absorbed. The time step width and the number of cells are set as $\Delta t = 10^{-12}\,\mathrm{s}$ $N_{cell} = 5760$, respectively. These parameters are selected to satisfy the stability conditions of the PIC simulation [50]. In the experiments, the localized-reversed magnetic fields can be generated by injecting current filaments to the devices. The magnitude and direction of the magnetic field produced by a current filament are computed based on the Biot–Savart law. Its values are inversely proportional to the distance to the filaments. In the 1D3V code, the injected current filaments are not realistic. To add a similar profile as the magnetic fields produced by the current filaments, we use the analytic function, as follows:

$$B_{y0,i}(x) = \frac{I}{x - x_i} = \frac{2 \times 10^{-4}}{x - x_i}, \tag{3.1}$$

$$B_{y,i}(x) = \begin{cases} \min(B_{y0,i}(x), 1) & \text{for} \quad x - x_i \geq 0, \\ \max(B_{y0,i}(x), -1) & \text{for} \quad x - x_i < 0, \end{cases} \tag{3.2}$$

$$B_y(x) = \sum_{i=1}^{4} B_{y,i}(x), \tag{3.3}$$

where $x_i = 0.02$, 0.04, 0.06, and 0.08 m. The maximum and minimum functions are added in each location to avoid a singularity of the curve near these locations. The external magnetic field B_y is displayed in Fig. 3.1 a). The magnetic fields B_x and B_z are not changed in this simulation. The magnetic field B_y is small along the simulation domain except for the locations near 2, 4, 6, and 8 cm to the wall, where the amplitudes of the magnetic fields are extremely strong. At these four locations, the direction of B_y is opposite, changing the direction from strong negative direction to strong positive direction. These points can be defined as “imaginary points” for injecting current filaments. Using the above analytic function, four strong localized magnetic fields are created in the simulation domain, as shown in Fig. 3.1 b). This simulation examined how the localized-reversed magnetic fields affect the particle and heat fluxes to the wall. The simulation follows the PIC steps presented in Chapter 2 and stops when the simulation system reaches an equilibrium stage. Starting from $t = 0$ s, where there is no plasma in the simulation, the total number of particles and kinetic energy increase drastically with time owing to the particle injection and remain stable when the system reaches the equilibrium stage. At the equilibrium stage, all of the field quantities remain stable. At this stage, the number of simulated particles defined by a set of 10^{10} real particles in the simulation is approximately $\sim 3 \times 10^6$ particles for each species. The particle density near the source region is approximately equal to $10^{-18}\, m^{-3}$. The value of density in the source affects the amount of fluxes entering the simulation domain, but does not influence the impact of the external magnetic field in heat flux reduction.

3.3 Simulation results

Figure 3.2 illustrates the comparison of potential profile, electron density, and ion density with and without adding the external magnetic field. The potential profile is obtained from Poisson's equation (Eq. 2.5). The electron and ion densities are computed as follows:

$$n_s = \int_{-\infty}^{\infty} dv_x \int_{-\infty}^{\infty} dv_y \int_{-\infty}^{\infty} dv_z f_s(\mathbf{x}, \mathbf{v}, t), \tag{3.4}$$

where f_s is the velocity distribution function of the particle species s in the (x, y, z) directions. In numerical studies, the particle density of species s in the cell j^{th} (at location X_j) is the sum of the weighting function S over all N_s simulated particles of species s in that cell :

$$n_{s,j} = \sum_{i=1}^{N_s} S(X_j - \mathrm{x}_{s,i}). \tag{3.5}$$

The same weighting (first-order weighting) function S is used in densities, fluxes, and force calculations; $\mathrm{x}_{\mathrm{s,i}}$ is the position of the i^{th} particle of species s in the cell. For simplicity, the potential at $x = 0$ is assumed to be equal to zero ($\Phi_0 = 0$). As shown in Fig. 3.2 a), the potential decreases slightly after $x > 0$ and drops quickly near the wall where the sheath has been formed. In front of the wall (at $x = 0.1\,\mathrm{m}$), the sheath potential is self-consistently formed to protect the losses of particles to the conductor wall. Because of the sheath potential effects, electron and ion densities decrease from the source (left) to the wall (right) of the simulation domain, as shown in Figs. 3.2 b) and c). In comparison with the case without changing a magnetic field, adding an external magnetic field reduces the number of particles that reach the wall by pushing particles (i.e., ions, electrons) back to the source region. Using the analytic magnetic field function for B_y as shown in Fig. 3.1, four strong magnetic mirrors appear in the system. When particles tend to be closed to the mirrors, their orbits change. Ions and electrons, which have high perpendicular velocity $v_\perp$, are trapped in the mirror. Meanwhile, only particles that have high parallel velocity can escape the magnetic mirror to reach the wall. Because of these strong magnetic mirrors, particles are

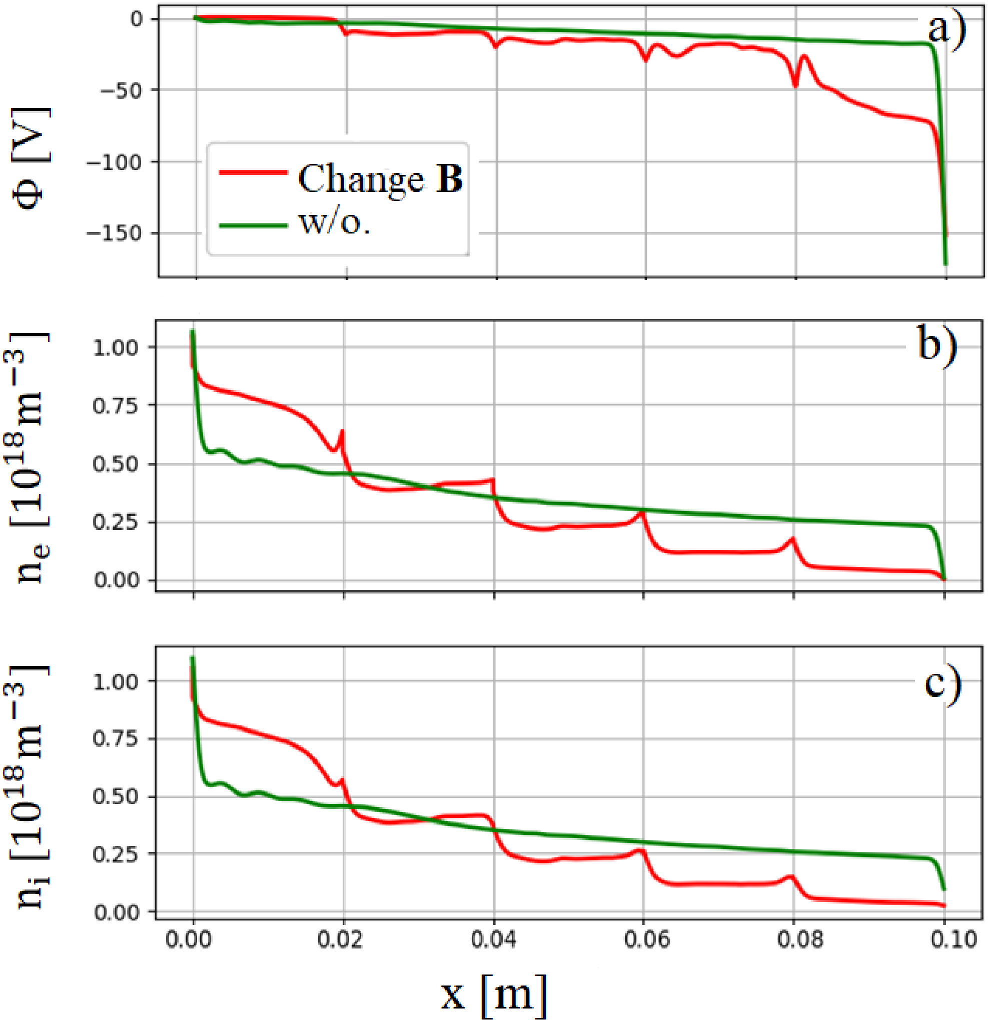

Figure 3.2: Comparison with and without changing the magnetic field of a) potential profile, b) electron densities, and c) and ion densities measured at the equilibrium stage. The red and green lines represent the profiles resulting with and without adding the external magnetic field, respectively. Sheath potential has been formed in front of the target. More ions and electrons are located near the source. The change in magnetic field reduces the number of particles reaching the wall.

mostly trapped in the left-side of magnetic mirror locations. The particle densities have similar profiles as a step downward function. Consequently, fewer particles reach the wall in comparison with the case in which no external magnetic field is added. Further, because of the localized magnetic field, there is a small gain of particles just before the four "imaginary points" in the changing magnetic field profile. Because the potential changes slightly along the simulation region, the parallel electrostatic force is small. Then, the external magnetic field is the key reason causing the reduction in the particle density profile. Localized-reversed magnetic fields affect the particle orbit and distribution, which, subsequently, change the particle and heat fluxes to the wall.

In this study, the important quantities that need to be considered are particle and heat fluxes along the simulation region. The one-dimensional particle flux $\Gamma_{s,x}$ and heat flux $Q_{s,x}$ are defined as:

$$\Gamma_{s,x} = \int_{-\infty}^{\infty} dv_x \int_{-\infty}^{\infty} dv_y \int_{-\infty}^{\infty} dv_z v_x f_s(\mathbf{x}, \mathbf{v}, t), \tag{3.6}$$

$$Q_{s,x} = \int_{-\infty}^{\infty} dv_x \int_{-\infty}^{\infty} dv_y \int_{-\infty}^{\infty} dv_z \frac{m_s}{2}(v_x^2 + v_y^2 + v_z^2) v_x f_s(\mathbf{x}, \mathbf{v}, t), \tag{3.7}$$

where m_s is the mass of the particle species s. In numerical calculations, these fluxes at each cell are computed as:

$$\Gamma_{s,x,j} = \sum_{i=1}^{N_s} v_{x,i} S(X_j - \mathrm{x}_{s,i}), \tag{3.8}$$

$$Q_{s,x,j} = \sum_{i=1}^{N_s} \frac{m_s}{2}(v_{x,i}^2 + v_{y,i}^2 + v_{z,i}^2) v_{x,i} S(X_j - \mathrm{x}_{s,i}). \tag{3.9}$$

Figure 3.3 shows the electron and ion fluxes at the equilibrium stage. Electron and ion densities become smaller near the wall, and then their fluxes decrease from the source to the wall region. Both the electron and ion fluxes along the simulation domain are reduced by adding the external magnetic field. In the presence of the four strong magnetic mirrors added in our simulation, electron and ion fluxes along the simulated zone decrease strongly ($\approx 77.6\%$ for electron flux and $\approx 74.9\%$ for ion flux). When particles move

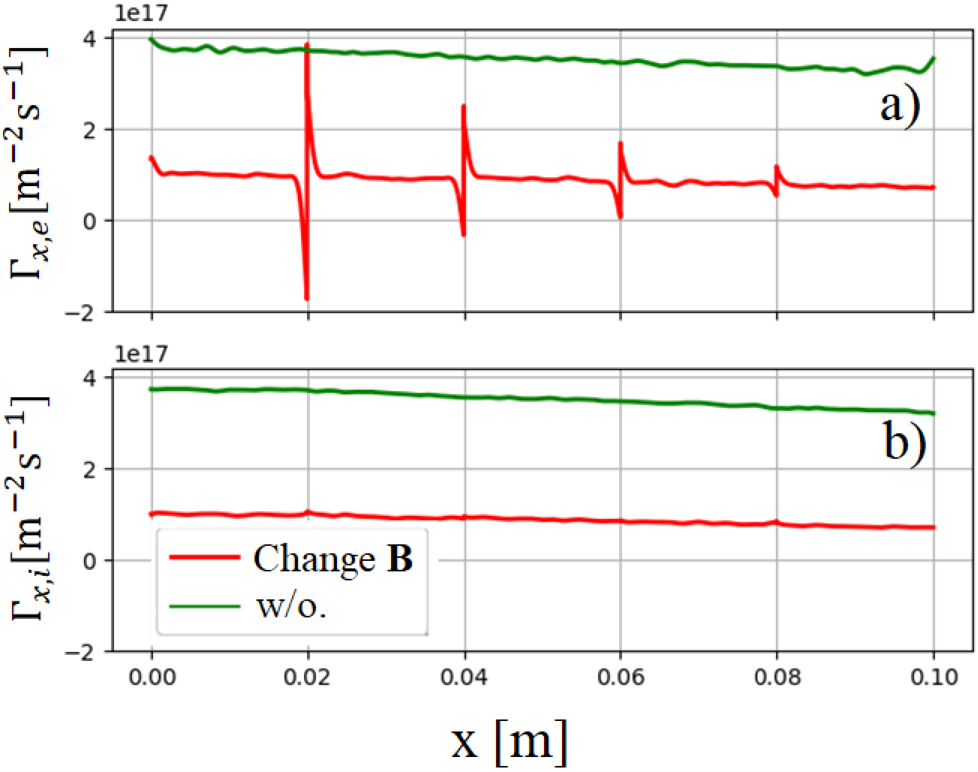

Figure 3.3: Comparison of one-dimensional a) electron flux $\Gamma_{e,x}$ and b) ion flux $\Gamma_{i,x}$ in the case with (red line) and without (green line) changing the magnetic field. Both electron and ion fluxes are reduced by changing the magnetic field.

close to the high negative values B_y region from the left, some of them are trapped, and then are forced to reflect back to the source region. Therefore, the particle flux at the left side of the "imaginary points" has lower value than that at other places. Similarly, when the particles are reflecting back to the source, they are trapped at the right side of the "imaginary points," where B_y has the highest positive values. The particle flux at this location is greater than that at other regions. This tendency results in large differences of the fluxes near the four locally reversed magnetic field locations. From the density figures, it is obvious that most of the particles are located near the source region. The closer to the source region the "imaginary points" are, the larger the gaps of the flux between the left and the right of these points. Because they are lighter and have smaller Larmor radius and higher thermal velocities than ions, electrons are more mobile than ions. The electron density that is just at the left side of these four points is higher than the ion density (Figs. 3.2 b) and c)). Consequently, the gaps of electron flux in these four points are more obvious than that of ions. The change in magnetic field also reduces the electron and ion heat fluxes along the simulation domain by approximately 79.9% and 73.4%, respectively, as displayed in Fig. 3.4. Ions are accelerated to hit the wall while electrons are pushed back to the source region owing to the sheath potential effect. Therefore, more ions are located near the wall than electrons. This transaction results in a reduction in electron heat flux and an increase in ion heat flux. The gain in ion heat flux is nearly equal to the loss in electron heat flux at this location. Similar to the particle flux, electron and ion heat fluxes also have large disparities at the left and right of the "imaginary points" and are clearer for the electron figure. The localized-reversed magnetic field reduces both the electron and ion fluxes to the wall. As a result, it reduces the total particle flux and heat flux to the wall. Figure 3.5 shows a comparison of particle and heat fluxes with and without the changing magnetic field. Except for the small region near the four "imaginary points", the total particle and heat fluxes reduced by approximately 76.2% and 78.9%, respectively. Figure 3.6 displays the electron, ion, and total particle flux using different values for generating external magnetic field. A stronger magnetic field increases the

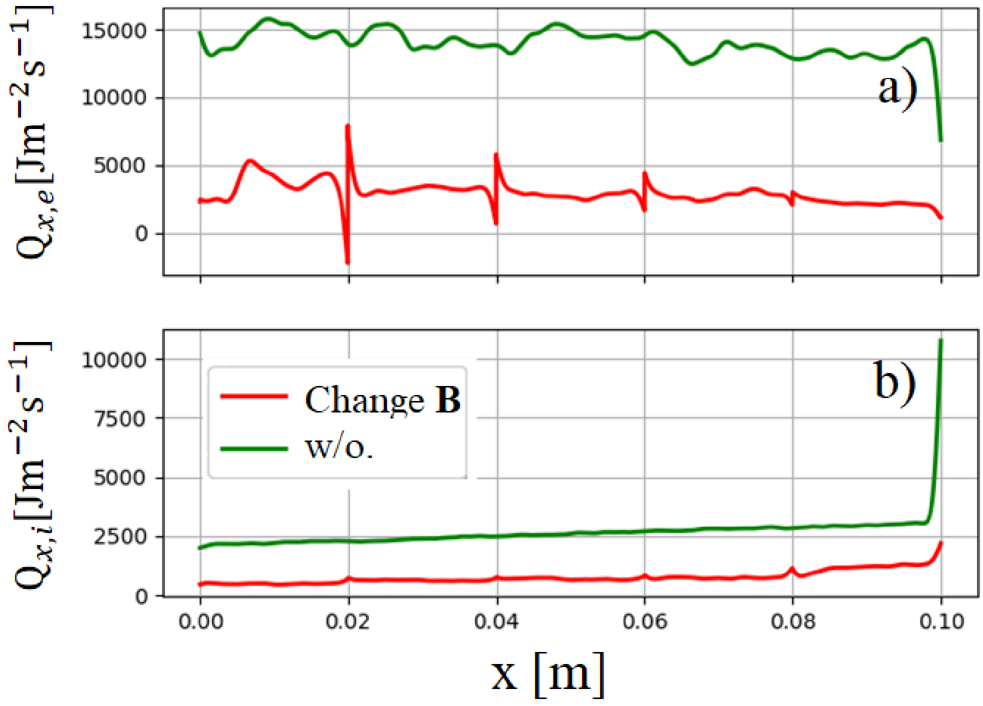

Figure 3.4: Comparison of one-dimensional a) electron heat flux and b) ion heat flux in the case with (red line) and without (green line) changing the magnetic field. By adding the external magnetic field, both electron and ion heat fluxes are reduced.

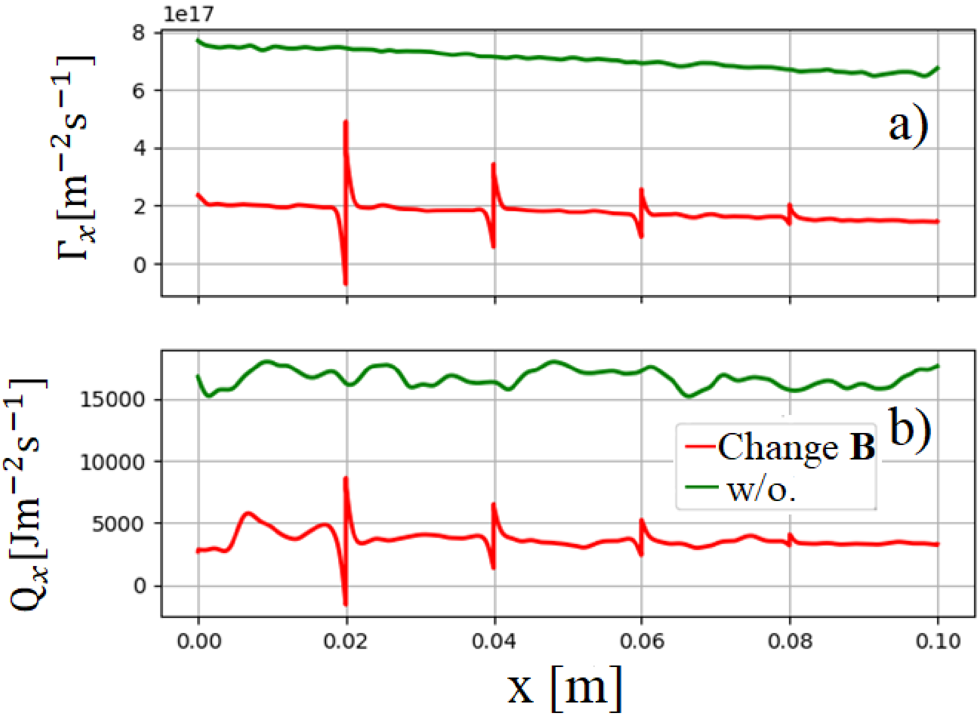

Figure 3.5: Comparison of one-dimensional a) total particle flux and b) heat flux in the case with (red line) and without (green line) changing the magnetic field. The external magnetic field reduces the particle and heat flux to the wall.

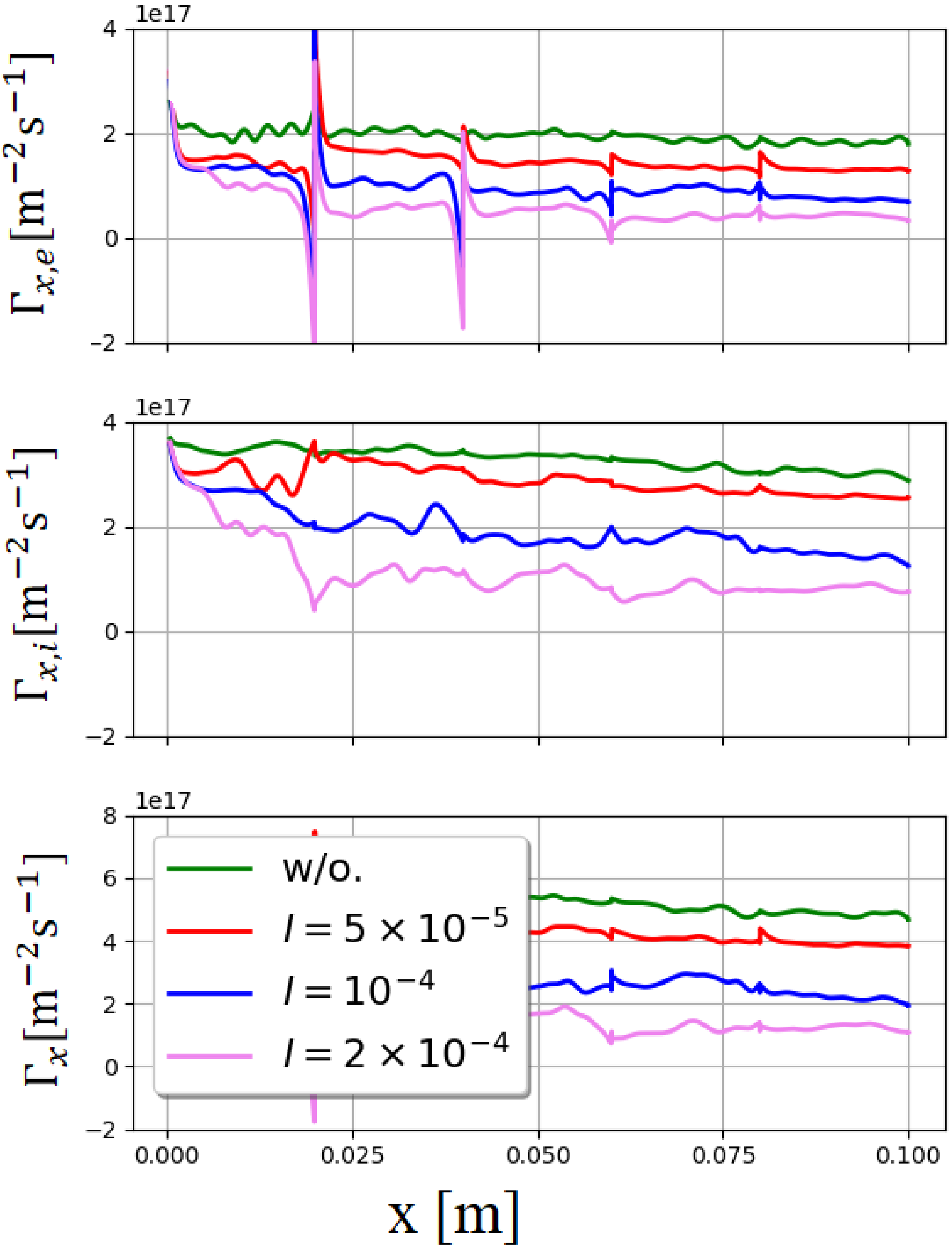

Figure 3.6: Comparison of one-dimensional a) electron, b) ion, and c) total particle fluxes without (green line) and with different values of the external magnetic field. A stronger external field reduces a greater amount of flux to the target.

magnetic mirror effects, and then, can trap a greater amount of particles within the mirrors, thus lowering the number of particle reaching the target. Consequently, the reduction in the particle flux is related to the strength of the external magnetic field.

3.4 Summary and discussion

The study of the effects of a magnetic field on particle and heat fluxes is presented in this chapter. We model a simple system assuming that particles enter from the source and are fully absorbed at the conductor wall. The analytic magnetic function, which can create localized-reversed magnetic fields in the y direction, is considered. The magnetic fields B_x and B_z are unchanged. This modification creates strong magnetic mirror fields and switches the direction of magnetic field B_y at some particular locations. This magnetic field profile is similar to the magnetic field profile generated by injecting current filaments in the performed experiments. Based on the modeling results, it can be concluded that the external magnetic field affects the electron and ion densities. By changing the magnetic field, the number of particles reaching the wall is reduced. Therefore, the application of an external magnetic field can control the particle and heat fluxes to the wall. The reason for heat flux reduction is the effect of the magnetic mirrors generated by inputting the analytic magnetic function. Particles are trapped in the simulation by the magnetic mirror effects rather than moving toward the wall. This idea can apply to the shield of high energy ion and electron fluxes for satellites or spacecraft in the space.

In one-dimensional consideration, an external locally reversed magnetic field is a good candidate for controlling the particle and heat fluxes to the wall. This work can be extended to two dimensional spaces including parallel and perpendicular directions of the wall. Then, the 2D3V PIC code is used to study how the change in magnetic field affects the particle and heat fluxes in both x and y directions. How the particle and heat fluxes distribute along the conductor surface with the external localized magnetic field in the 2D3V

PIC simulation will be discussed in the next chapter.

Chapter 4

Controlling particle and heat flux to wall by current filaments

4.1 Introduction

In the previous chapter, we found that the external localized-reversed magnetic fields can control the particle and heat fluxes to the target in a one-dimensional consideration. Magnetic mirrors were created, and trapped particles in the simulation domain; the number of particles reaching the target was reduced. We aim for studying how the particle flux profiles are affected by the external magnetic field in two dimensional consideration. This external magnetic field profile is added by injecting current filaments into the simulation domain. The 1D3V PIC code is extended into a 2D3V PIC code to consider two spatial dimensions. Apart from the direction parallel to the plasma flow, we consider another direction along the target, that is, the direction perpendicular to the original plasma flow. The injected current filaments have a direction perpendicular to the simulation plane. The localized plasma flow enters the simulation domain from the source region and the particles are fully absorbed at the end target. This chapter discusses how the current filament injection technique affects the particle and heat fluxes to the wall in two dimensional views, using the PIC simulation.

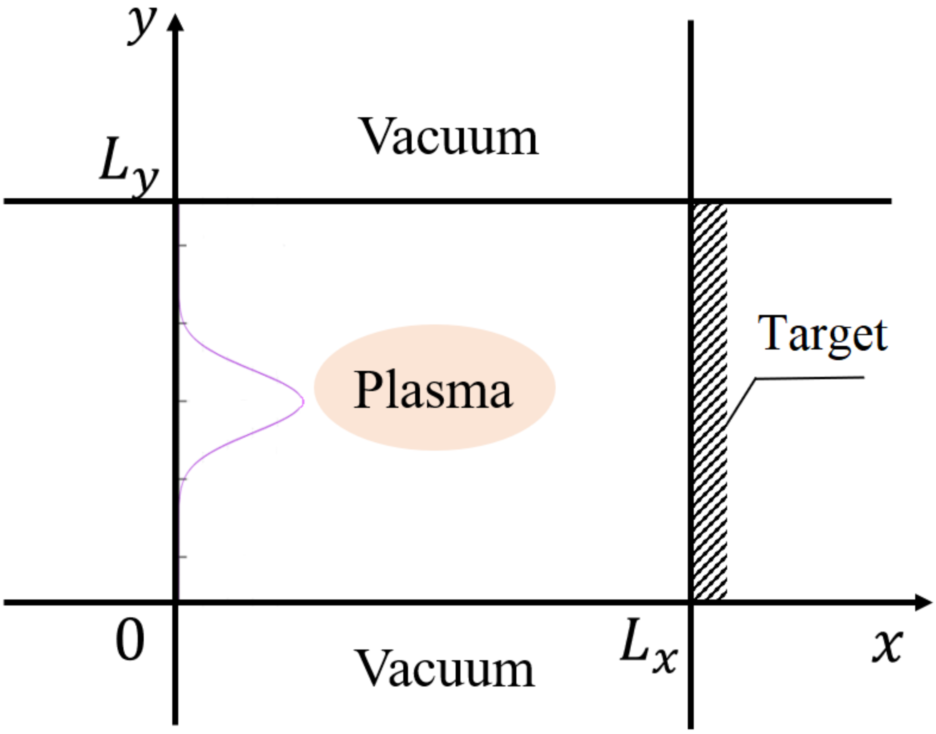

Figure 4.1: Simulation box. The plasma is bounded by vacuum. Particles are injected from the left boundary at $x = 0$ and are fully absorbed at the right boundary where $x = L_x$.

4.2 Simulation model

In this chapter, particle positions and field quantities are considered in two dimensional x and y spaces with three components of velocity (v_x, v_y, v_z) (2D3V). In this small and simple simulation region, the plasma enters from the left boundary at $x = 0$, and is fully absorbed at the right boundary $x = L_x$. The simulation domain has the size $L_x = 0.03\,\text{m}$ from the source to the conductor wall, and $L_y = 0.03\,\text{m}$ in the y direction. We assume that the plasma mainly flows in the middle region of the simulation box, and the particles can not penetrate further to the two end boundaries in the y direction. In other words, the lower and upper boundaries are considered as a vacuum, as shown in Fig. 4.1. If a particle can move out of the simulation box from the upper or lower boundaries at time t, it will be reflected back into the simulation domain, given as $y_t^{refl} = 2L_y - y_t$ for $y_t > L_y$ or $y_t^{refl} = -y_t$ for $y_t < 0$ and $v_t^{y,refl} = -v_t^y$. In this simulation, as that in the previous Chapter, only ions and electrons are included. No collision process or secondary emission is taken into account.

At the initial stage, the simulation is assumed to be empty. There is no plasma inside the system. Particles are injected during each time step in the simulation, around $x = 0$. In this 2D simulation, we test with the condition that the electron and ion fluxes at $x = 0$ are equal to each other, and are constant with time. In the y direction, these fluxes have a Gaussian distribution profile to generate the localized fluxes toward the target. The velocities of the injected particles follow a fully Maxwellian distribution function, which satisfies the condition that the parallel velocity $v_{||} > 0$. As in the previous Chapter, the following parameters are used in the simulation: ion–electron mass ratio $m_i/m_e = 1836$, electron source temperature $T_{\mathrm{e}0} = 100\,\mathrm{eV}$, ion source temperature $T_{\mathrm{i}0} = 50\,\mathrm{eV}$, density $n_0 = 10^{16}\,\mathrm{m}^{-3}$, background magnetic field $B_x = 0.2\,\mathrm{T}$, and $B_z = 0.02\,\mathrm{T}$. No magnetic field in the y direction is given.

The system is started by setting the time step size $\Delta t = 0.02\omega_{pe0}$ and the number of cells $N_{cell} = 300$ in each direction. In the two upper and lower boundaries, the electric field is assumed to be equal to zero. The current filaments are injected into the system in the z direction, which is perpendicular to the system plane. We test the simulation in two cases: in Case 1 the current filaments have the same outward direction, whereas in Case 2 they have the opposite direction. The locations and directions of these filaments are depicted in Fig. 4.2. In both cases, all the filaments have the same current strength. The Biot–Savart law is used to compute the magnitude and direction of the magnetic field generated by a current filament given as follows:

$$B = \frac{\mu_0 I}{2\pi r} = \frac{\mu_0 I}{2\pi\sqrt{(x - x_{fil})^2 + (y - y_{fil})^2}}, \tag{4.1}$$

where $\mu_0 = 4\pi \times 10^{-7}\,\mathrm{Tm/A}$ is the permeability of the free space, $I = 1\,\mathrm{kA}$ is

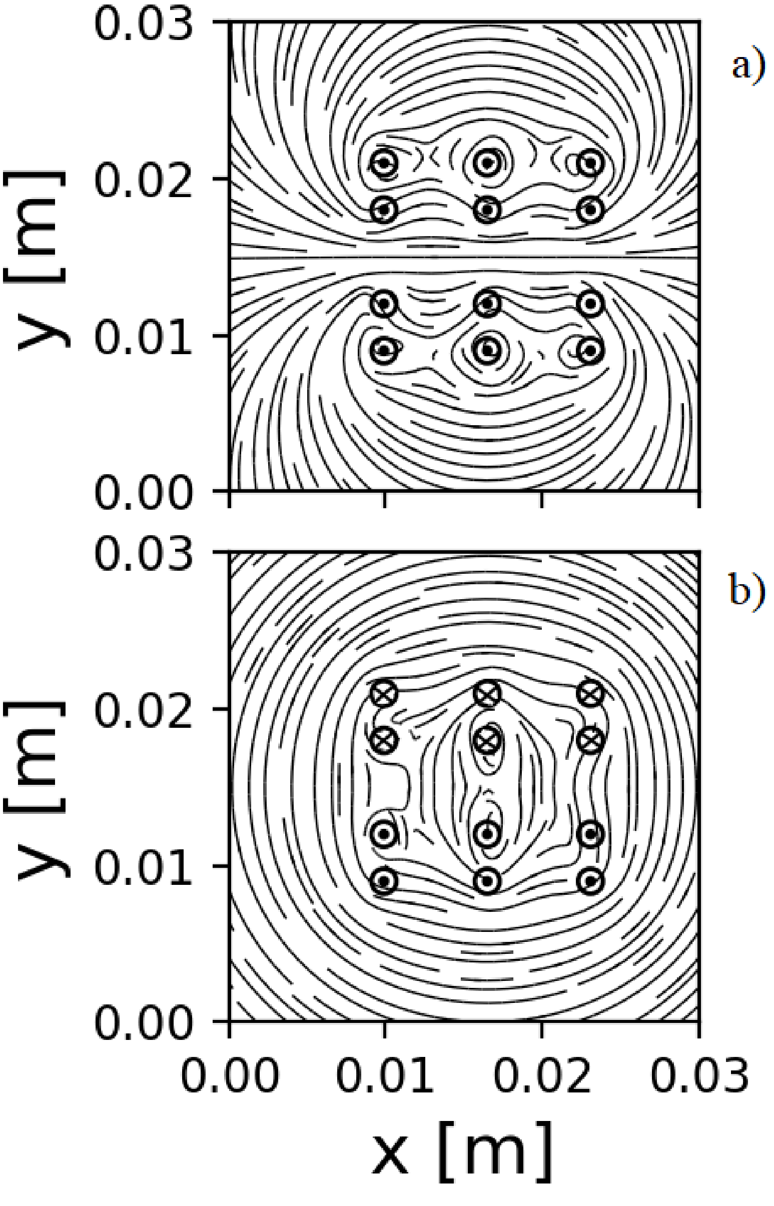

Figure 4.2: Magnetic field generated by injecting current filaments: a) the same direction of filaments (Case 1), b) opposite direction of filaments (Case 2).

the current intensity, and x_{fil} and y_{fil} are the locations of the filaments in x and y directions, respectively. To avoid a singularity of the magnetic field, at the location of these injecting locations, the strength of the magnetic field is cut down to $|B| = 1\,\mathrm{T}$. Injecting the current filaments changes the directions of magnetic fields in the system. From the straight magnetic field line parallel with the target, the current filaments change the magnetic structure in the simulation box as shown in Fig. 4.3. The magnetic structure in the simulation domain is different in these two cases. In the case of the same direction of current filaments, the magnetic field is bending in the same direction around the injecting locations toward the target. When opposite direction of current filaments is used, as in Case 2, the magnetic fields above and below $y = L_y/2$ are different. The opposite tendency of the magnetic field line in these two cases leads to different behavior of plasma flow, which is caused by the injection of current filaments. Staring from $t = 0\,\mathrm{s}$, the simulation will terminate when the system reaches the equilibrium stage in which all the field quantities remain stable. We compare the particle quantities, such as particle flux with and without injecting current filaments, to study the effects of the current filaments on the particle and heat fluxes to the wall.

4.3 Simulation results

$\Gamma_{s,\alpha}$ and $Q_{s,\alpha}$ are defined as the particle and heat fluxes of the species s in the direction α, which are given as

$$\begin{aligned} \Gamma_{s,\alpha} &= \int_{-\infty}^{\infty} dv_x \int_{-\infty}^{\infty} dv_y \int_{-\infty}^{\infty} dv_z v_\alpha f_s(\mathbf{r}, \mathbf{v}, t), \\ Q_{s,\alpha} &= \int_{-\infty}^{\infty} dv_x \int_{-\infty}^{\infty} dv_y \int_{-\infty}^{\infty} dv_z \frac{m_s}{2}(v_x^2 + v_y^2 + v_z^2) v_\alpha f_s(\mathbf{r}, \mathbf{v}, t), \end{aligned} \tag{4.2}$$

where $f_s(\mathbf{r}, \mathbf{v}, t)$ is the particle distribution function at position $\mathbf{r}$, velocity $\mathbf{v}$, and time t, and m_s is the mass of the particle of species s. In numerical studies, these fluxes can be computed in each cell (j, k) at the location

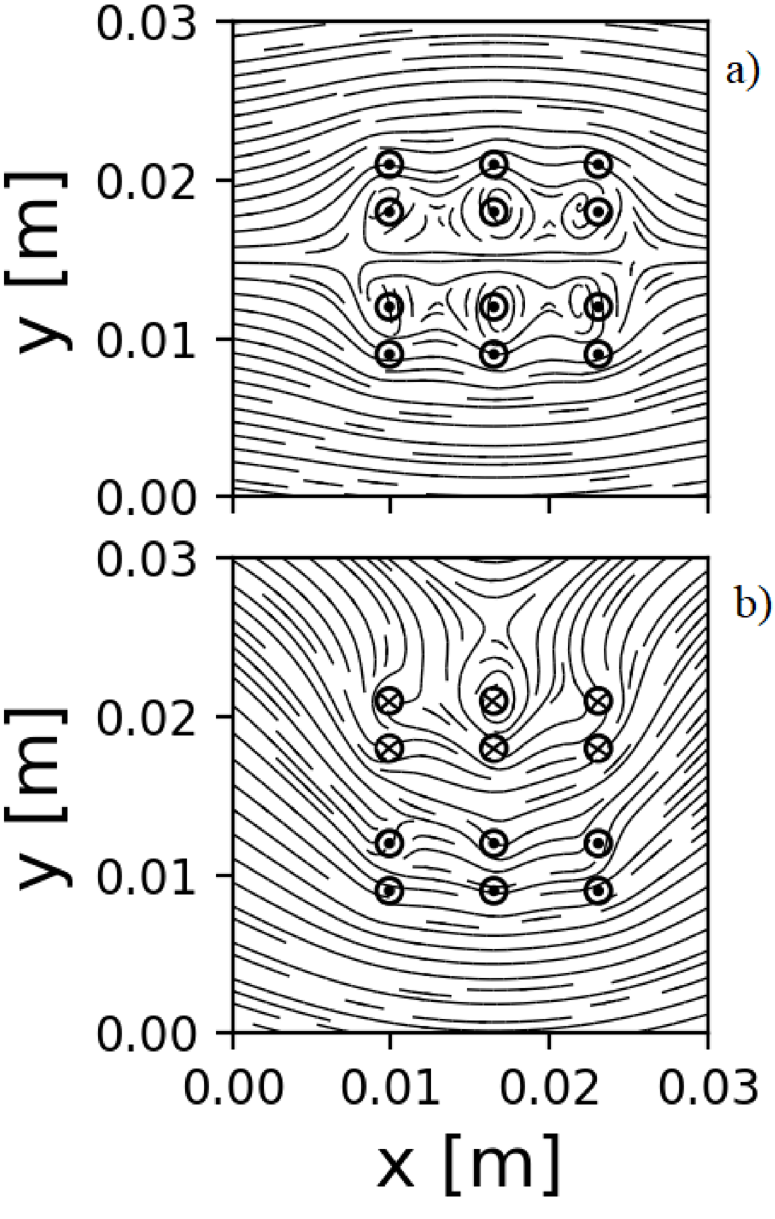

Figure 4.3: Total magnetic field in the simulation domain after injecting current filaments in two cases: a) the same direction of filaments (Case 1), b) opposite direction of filaments (Case 2).

(X_j, Y_k) as follows:

$$\begin{aligned} \Gamma_{s,\alpha}(j,k) &= \sum_{i=1}^{N_s} v_{s,\alpha,i} S(X_j - \mathrm{x}_{s,i}, Y_k - \mathrm{y}_{s,i}), \\ Q_{s,\alpha}(j,k) &= \sum_{i=1}^{N_s} \frac{m_s}{2}(v_{x,i}^2 + v_{y,i}^2 + v_{z,i}^2) v_{s,\alpha,i} S(X_j - \mathrm{x}_{s,i}, Y_k - \mathrm{y}_{s,i}), \end{aligned} \tag{4.3}$$

where $S(x,y)$ is the area weighting function proposed in Chapter 2 and N_s is the number of simulated particles of the species s [49]. The normalized particle flux $\hat{\Gamma}_x$ at $x = 0$ is fixed to be constant with time and has the same value for electrons and ions, which is given by

$$\hat{\Gamma}_x(y) = \hat{\Gamma}_0 \exp\left[-\frac{(y - L_y/2)^2}{2}\right]. \tag{4.4}$$

$\hat{\Gamma}_x(y)$ has a strong peak value at the mid region where $y = L_y/2$. The values of $\hat{\Gamma}_0$ only affect the amount of particle fluxes entering the simulation box. They do not affect the direction of particle flow or impact of the current filaments in the simulation domain. Therefore, in this simulation, we adopted $\hat{\Gamma}_0 = 1.0$ for simplicity. Figure 4.4 shows the particle density in the simulation box. Without the injection of current filaments, because of no magnetic B_y component, the particles bombard straightly to the target (see Fig. 4.4 a) for electron density and Fig. 4.4 d) for ion density). When the current filaments are added into the simulation, the magnetic structure changes. In magnetized plasma, particles move along the magnetic field lines with a gyro motion. The magnetic structure in the two cases of injection is different, resulting in different plasma flow in these two cases. Consider the first case when current filaments with the same direction are injected. In this case, as displayed in Fig. 4.3 a), most of the magnetic field lines bend in the same direction toward the target. Starting from $x = 0$, the magnetic field line in this case is convergent toward the current location. Therefore, once the plasma enters the simulation domain from the left boundary, particles move along these bending magnetic field lines. The flow of plasma in the simulation box is downward and tightened as the structure of the magnetic field, which is shown in Figs. 4.4 b) and e) for electron and ion densities, respectively.

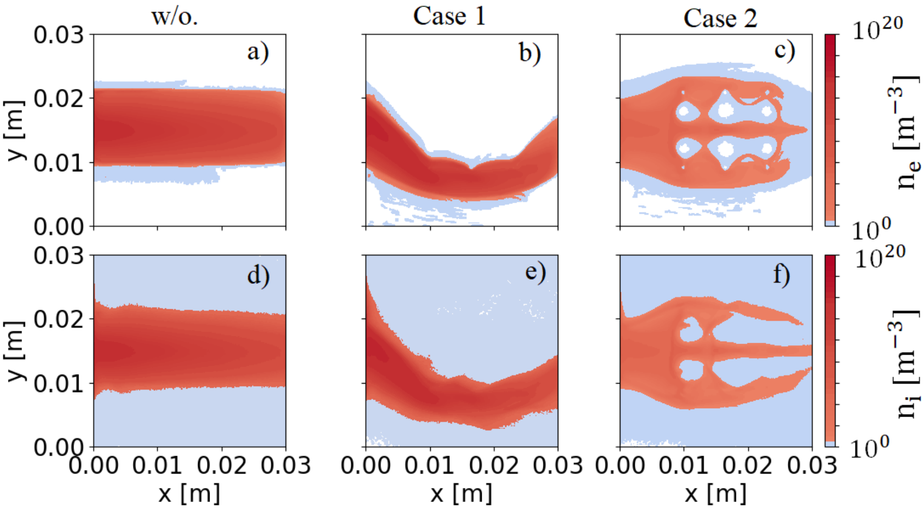

Figure 4.4: Particle densities at the equilibrium state with and without injecting current filaments. Figures a), b), and c) show the electron density, whereas Figs. d), e), and f) show the ion density. The flow of the particle transport depends on the magnetic field structure generated by current filaments. A sharpened profile is obtained by using the same direction of filaments (Case 1). The opposite direction of current filaments broadens the particle flow in the simulation (Case 2).

Electrons have smaller Larmor radius, and most of the electron transport follows the magnetic field line. In the collisionless case, electrons barely move from one magnetic field line to another. As a result of this limitation, none of the electrons penetrate in the upward direction (white color in the Fig. 4.4 b)). An ion has much higher Larmor radius than an electron. Once it makes the gyro motion, the ion can move with a large displacement in the y direction. Because of the magnetic mirrors formed between current filaments, low-parallel-velocity ions are kept in the simulation domain; only particles having high parallel velocity can quit the mirror to reach the target. For the energy conservation, the low-parallel-velocity particles might have high perpendicular velocity. When the perpendicular velocity of the ion is sufficiently large to cancel the magnetic mirror effects, the ion can quit the main plasma flow and jump into the whole simulation domain while making a circular orbit. The number of particles which can escape the main stream is smaller than the number of particles remaining in the main stream. The electrostatic interaction with electrons along the magnetic field lines causes the asymmetry in the ion figure. This process is also captured in Fig. 4.4 e).

When the opposite direction of current filaments is used, as in Case 2, the magnetic field lines are divergent from the source to the middle region. Therefore, the flow of plasma toward the wall is expanded inside the simulation region based on the magnetic field line, as shown in Figs. 4.4 c) and f). This expansion near the source region helps to expand the strong localized fluxes entering the simulation box, and relaxes the particle fluxes toward the wall. This can help to decrease the number of particles reaching the target or reduce the burden of the strong localized flux toward the target. Even though in front of the target the magnetic field line is convergent toward the target, the particle density is still reduced in this case because most of particles are trapped by the magnetic mirror effects, and the plasma flow is expanded. In both, injecting the current changes the particle flow in the simulation box and reduces the number of particles reaching the target. Therefore, the particle flux to the target is affected by the injection of the current filaments

Figures 4.5 a), 4.5 b), and 4.6 show the fluxes of electrons, ions, and

(a) Electron flux at the wall target

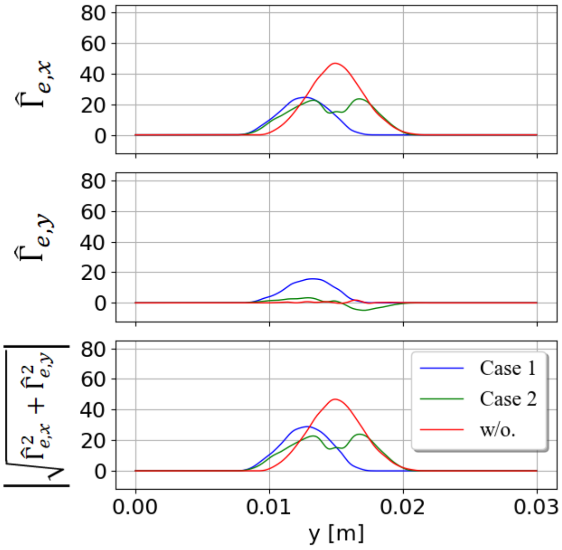

(b) Ion flux at the target.

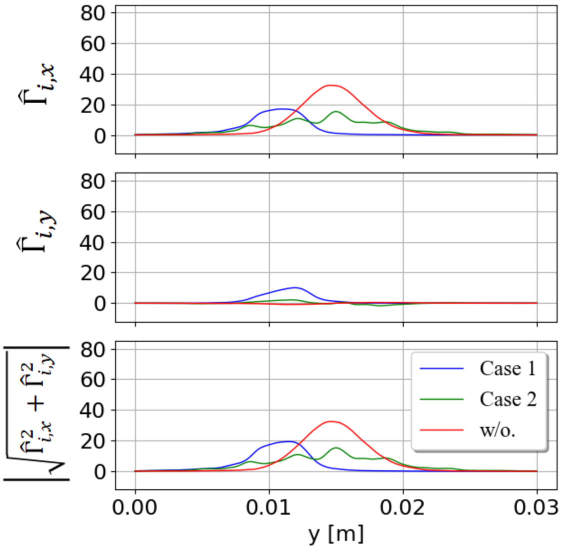

Figure 4.5: Electron, and ion fluxes at the wall target. Injecting the current filaments reduces the particle flux in the x direction while changing the flux in the y direction.

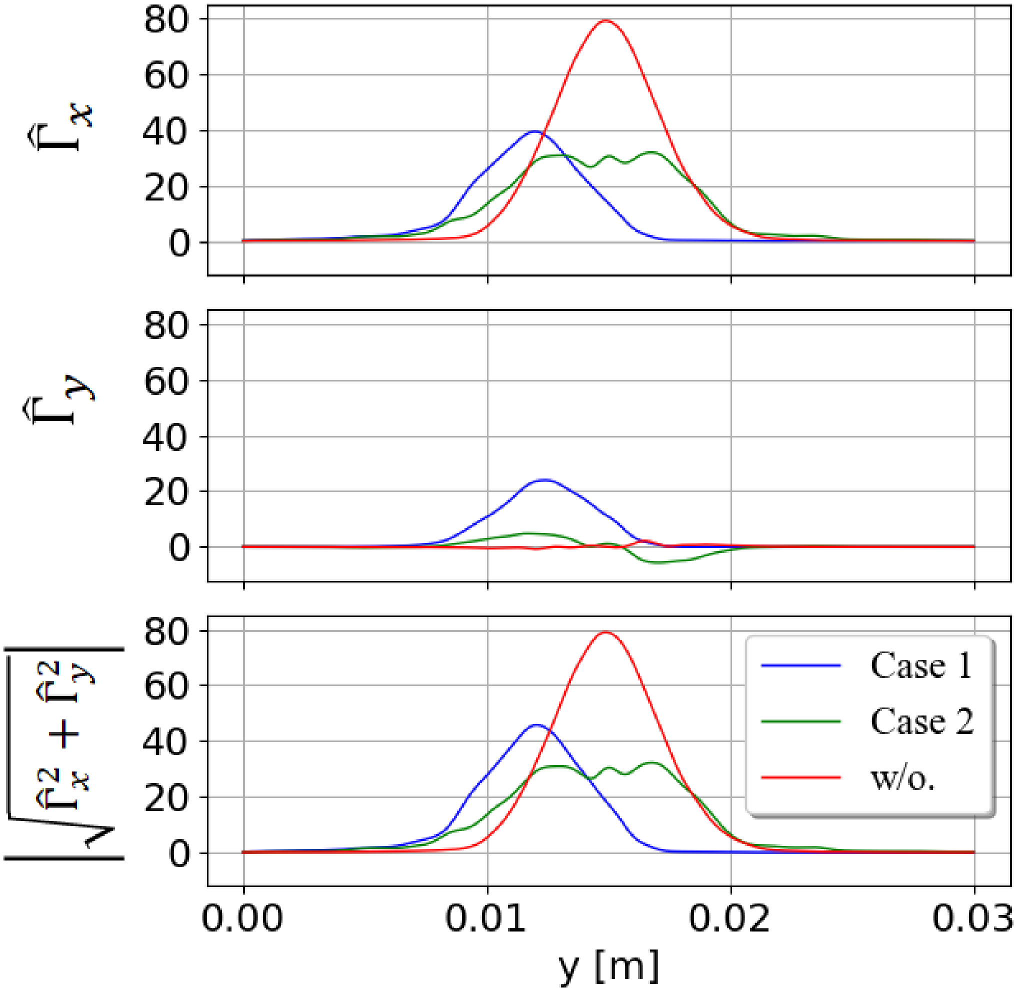

Figure 4.6: Total particle fluxes at the wall target. The total flux to the wall is reduced by using the current filaments. Using the opposite direction of filaments (Case 2) can expand the flux along the target.

total particles along the wall target, respectively. Without injecting current filaments, the localized flux enters the simulation domain straightly. At the end target, the particle flux still remains in the localized shape. The high peak of particle flux is reduced by injecting the current filaments into the simulation domain. Because the particles are trapped inside the simulation domain, rather than reaching the wall, the particle flux at the target is decreased in the case of injection of current filaments compared with when no current filaments are injected. The peak value of particle flux is reduced nearly by half in the presence of current filaments. Current filaments change the direction of the plasma flow in the simulation box, and the center of the particle flux at the target is shifted compared with the case without injection of current filaments The magnetic field in the y direction B_y is generated by injecting the current filaments. A movement of particles in the y direction occurs. Consequently, the flux in the y direction, in other words Γ_y, is not zero, as in the middle figures of Figs. 4.5 a), 4.5 b), and 4.6 when comparing the cases with and without injection of current filaments. This flux Γ_y is higher in Case 1, and mostly is positive because the magnetic field B_y in this case has the same positive direction in front of the target. In Case 2, B_y near the wall has the opposite direction from the middle line $y = L_y/2$. The flux in the y direction has opposite direction from the middle line. Even though injecting the current filaments reduces the particle fluxes in the x direction and produces a flux in the y direction, the total particle flux at the target $\sqrt{\Gamma_x^2 + \Gamma_y^2}$ is still reduced in both cases under consideration.

A similar behavior is obtained for the heat flux profile, as displayed in Fig. 4.7. The injection of current filaments reduces the high peak of the heat fluxes at the target. Using current filaments with the same direction produces larger heat fluxes in the y direction and sharpens the localized distribution of the fluxes. meanwhile, current filaments with opposite direction expand the fluxes along the target to reduce the peak burden for the materials. Therefore, to reduce the high peak fluxes to the target, injecting current filaments in the same direction into the system can be applied. For both flux reduction and expansion, using filaments with opposite direction is a better choice. The injection of current filaments can be implemented in

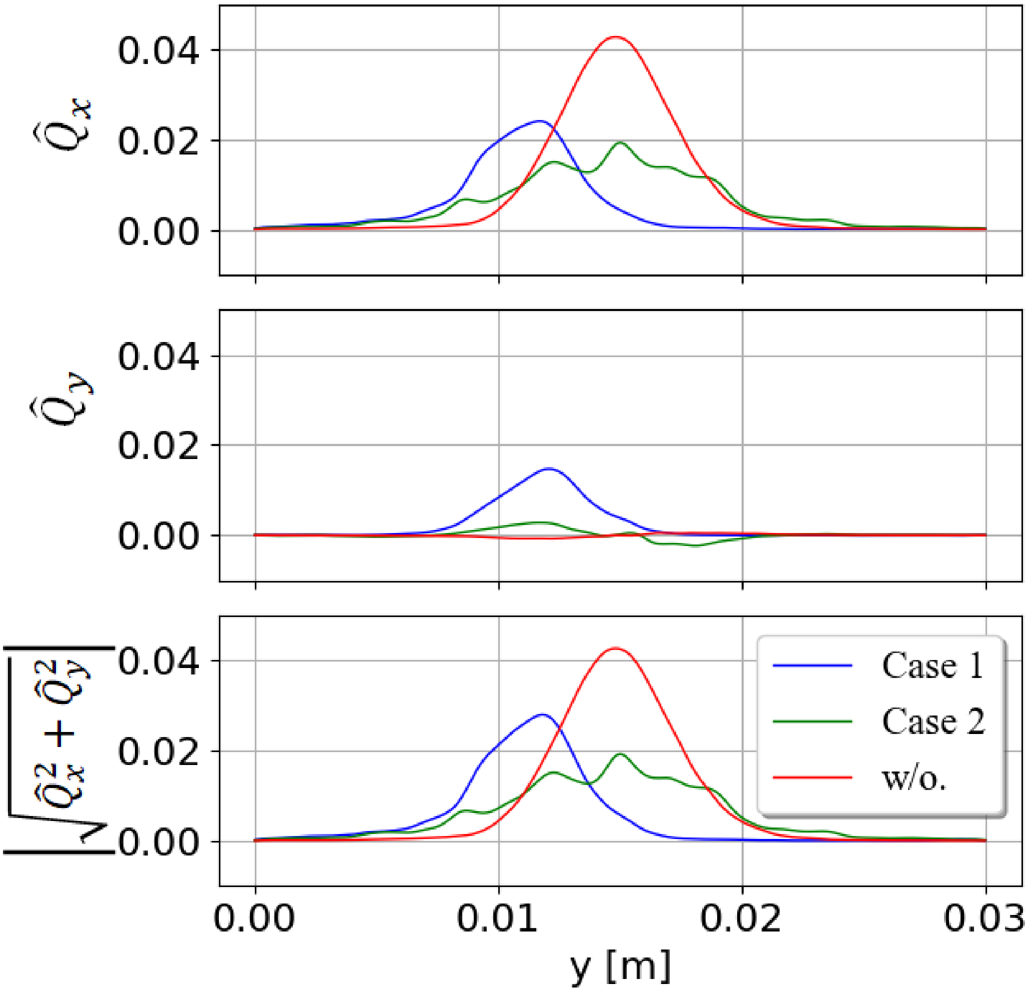

Figure 4.7: Total heat flux at the target. This is reduced by injecting current filaments. The same direction sharpens the fluxes, whereas the opposite direction expands the fluxes to a wider area along the wall.

(a) Different current strengths

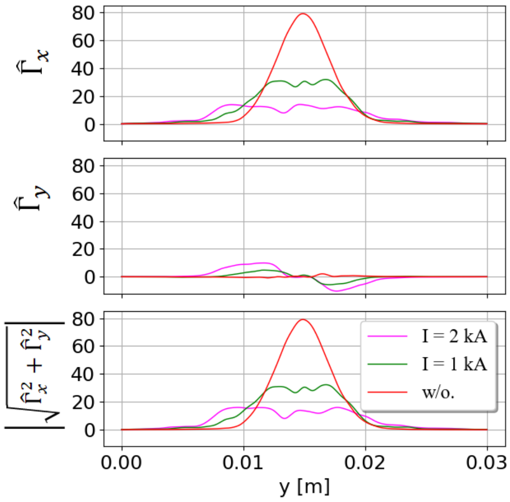

(b) Different number of current filaments

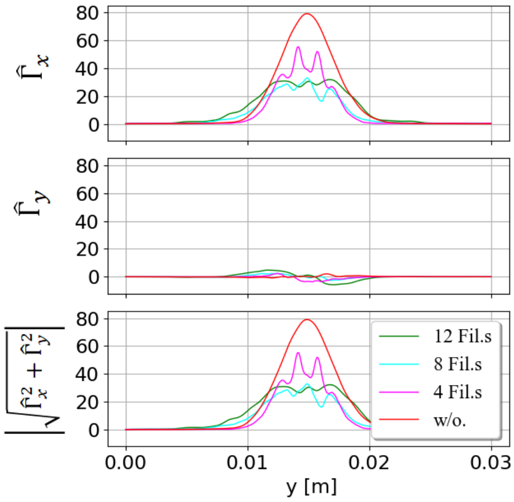

Figure 4.8: Comparison of total particle fluxes at the wall target using different current strengths and different numbers of current filaments. The strength and number of current filaments affect the reduction of particle flux at the targets.

the experiment, for example, based on the idea of using lower hybrid waves (LHWs) [55]. In the EAST, the LHW system is installed at the low field side midplane, which can produce the same direction of current filaments. For the case of opposite direction of filaments, a special treatment is required to change the direction of filaments when performing the experiments.

The magnetic field generated by the current filaments depends not only on their direction but also on their strength and number. Figures 4.8 a) and b) show the particle fluxes at the target using different current strengths and different numbers of current filaments, respectively. The opposite direction of the current filaments is used in this comparison. A stronger current is applied and a higher reduction of the peak fluxes at the targets is obtained. This reduction comes from the wider expansion along the target for the stronger current strength, resulting in a higher discrepancy of fluxes in the y direction. Similarly, increasing the number of injected current filaments is proportional to a reduction in the particle flux at the target. A greater number of injected current filaments generates a larger number of magnetic islands in the simulation domain. By increasing the number of filaments, the particles become trapped in the simulation domain, rather than moving toward the wall target. Overall, the reduction and expansion of the particle flux at the target depends on the strength and number of the current filaments. Depending on the shape of the devices, values of particle flux, and magnetic configuration, the strength and number of current filaments should be considered to obtain high efficiency in the particle flux reduction to the targets in the experiments. Because of the magnetic configuration generated by the injecting current filaments, the particles are trapped mostly in the region from the source to the first current filament location. To study how the length of the simulation box affects the particle flux, we attempt to expand the simulation box in the x and/or y directions maintaining the same locations of current filament to the wall. Again, the opposite direction of twelve current filaments is used. The flux at $x = 0$ is equal through all of the test lengths. Figure 4.9 shows the particle densities with and without injecting the current filament with using different system lengths. From the original case where $L_x = L_y = 0.03\,\mathrm{m}$, we expand the simulation box

(a) Electron density

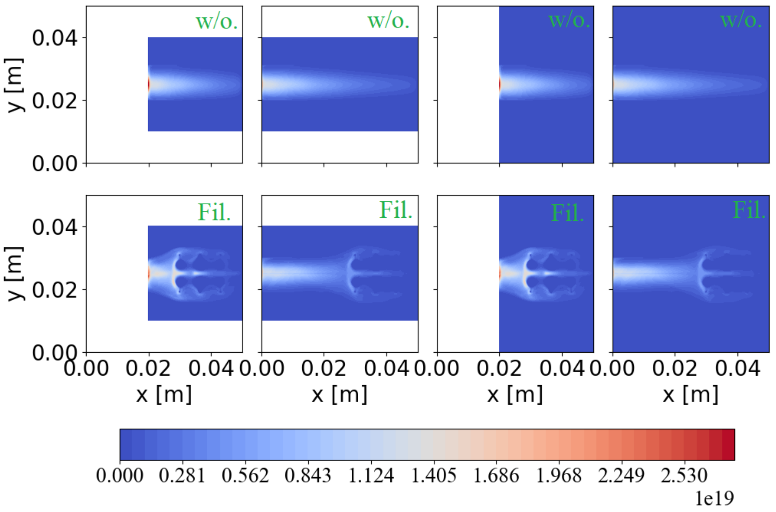

(b) Ion density

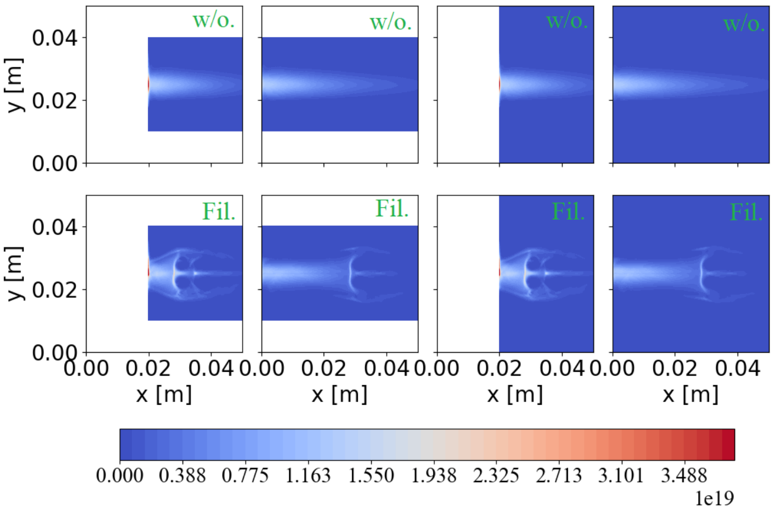

Figure 4.9: Electron and ion densities with different system lengths in both cases, with and without using current filaments.

a) Particle flux at the target

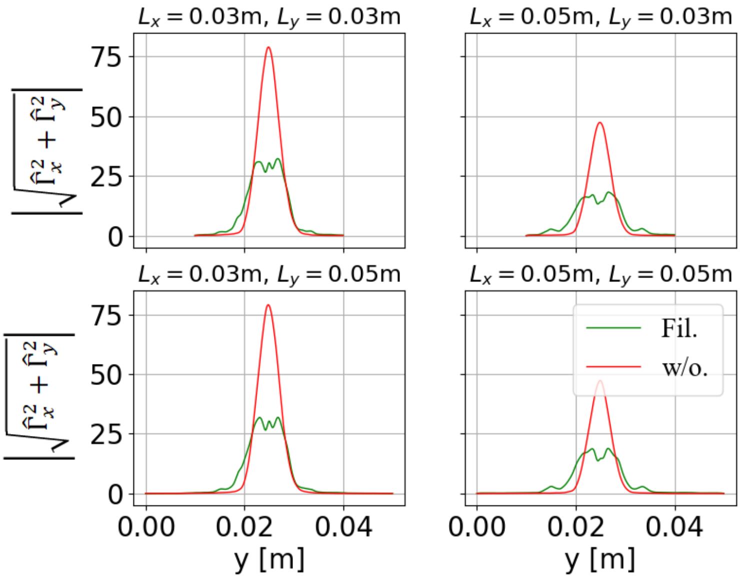

b) Heat flux at the target

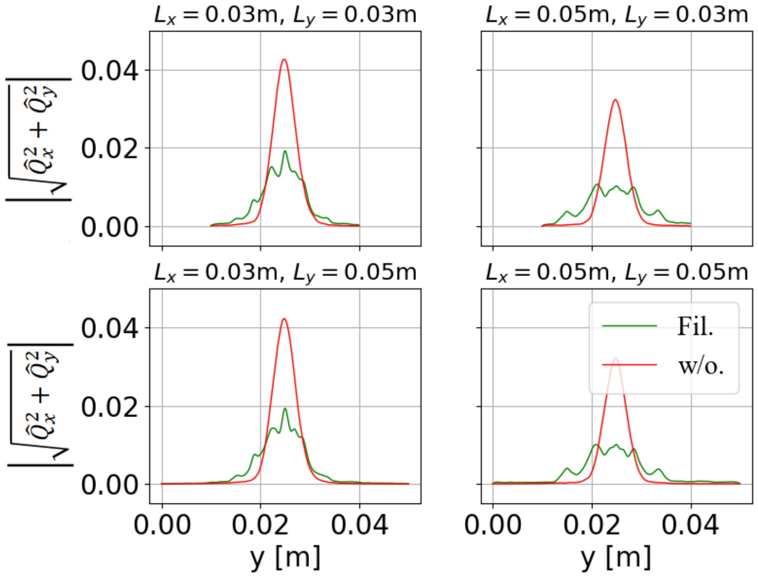

Figure 4.10: Particle and heat fluxes at the target with different system lengths with and without current filaments.

into three other cases as follows: a) expand the x direction to $L_x = 0.05\,\mathrm{m}$ $L_y = 0.03\,\mathrm{m}$, b) expand only the y direction to $L_x = 0.03\,\mathrm{m}$ $L_y = 0.05\,\mathrm{m}$, and c) expand both x and y directions to $L_x = 0.05\,\mathrm{m}$ $L_y = 0.05\,\mathrm{m}$. We compare the particle fluxes at the target as shown in Fig. 4.10. We find that by the same amount of the flux at the source, the plasma in the system with larger length in the x direction has lower flux at the target. This occurs mainly because the distance from the source to the wall is longer, and the particle flow near the target becomes smaller. Expanding the simulation box in the y direction does not affect to the distribution of the particle in the simulation. Therefore, the boundary in the y direction does not influence the flow of the localized flux to the target. In all these length expansions, the injection of current filaments still work well for reducing the strongly localized flux at the target.

4.4 Summary and discussion

The effects of injecting current filaments on particle and heat fluxes are studied using the 2D3V PIC simulation. We model a simple situation, assuming that particles are entering the simulation domain at $x = 0$ and are fully absorbed at the wall. The particles are injected from the left side with localized fluxes, which are equal for ions and electrons and are constant with time. It is concluded that current filaments change the magnetic structure in the system, and then influence the particle transport toward the target. Because of the magnetic mirror formed between current filaments, the particles are reflected back into the source region instead of reaching the wall target. Therefore, injecting current filaments can help to decrease the number of particles reaching the wall and reduce the high particle and heat fluxes to the wall. The reduction and expansion of the particle flux by injecting the current filaments depend on the strength and number of current filaments. Deeper reduction and larger expansion of the particle flux can be obtained by changing the strength and number of current filaments. To perform real experiments, different strengths and numbers of current filaments will be used, based on the wall boundary conditions or system input parameters. Using current filaments with the same direction reduces the peak of the fluxes at the wall, whereas the localized fluxes are sharpened. Using current filaments with opposite direction, as proposed in this work, high peak fluxes to the wall can be reduced and these localized fluxes can be expanded along the targets. In summary, the injection of current filaments is a good option to reduce the high heat fluxes to the target. This method can be applied for shielding satellites or spacecraft from high energy particles. Table 4.1 presents the some of the advantages and disadvantages of our proposed method and other methods for reducing particle fluxes to the target [39, 56, 57, 58, 59, 33]. Except for divertor biasing, where only one species of fluxes is reduced while the other is increasing, most of the methods are acceptable techniques for high heat flux reduction. However, each technique has its own issues in relation to the experimental work. Based on the configuration and design of each device, different methods for heat flux reduction might be used to avoid technical challenges or physical issues.

Table 4.1: Advantages and disadvantages of injecting current filaments and some widely used methods for reducing high particle fluxes to the target.

		Fusion				Space	
	Injecting current filaments	Divertor biasing (negative bias)	Plasma detachment	RMPs	Snowflake Divertor	Active Shielding method	Chaotic magneitc field
Advantages	Reduce both electron and ion fluxes	Electron flux reduces	Shielding fluxes from the target	Shielding fluxes from the target	Particle flux to the target is divergent	Protects particles from solar and galactic rays	Shielding particles
Disadvantages	Technical issues (location and direction of filaments)	Increases ion flux	Physical issues (plasma pressure)	Physical issues (effects of stochastic field)	Need to change the divertor geometry	Unstable for GCR shielding	Damage GCR spectrum

GCR: Galactic cosmic ray

Chapter 5

Potential formation with 2D magnetic field

5.1 Introduction

In magnetically confined plasma, particles move along the field line with a circular gyro motion. The magnetic field affects the particle orbit, and then changes the transport of particles. Usually, the magnetic field lines in the edge of the fusion plasma are opened. Because electrons have higher thermal velocities and are lighter than ions, the losses of both particles in the open field line are not balanced. Based on this difference of particle transport, an electrical potential is formed in the edge region. In a large aspect ratio limit, particles drift off the flux surface because of the effect of the toroidally induced ∇B and curvature drifts [28]. The neoclassical effect, which is the classical transport including the effects of toroidal geometry, increases plasma transport coefficients. Grad-B drift coming from the toroidicity is one of the key factors that affect particle transport in cases where no anomalous transport and turbulence effects are considered. Because the grad-B drift is in the opposite direction for electrons and ions, it is considered one of the candidates to break down the symmetric behavior of the particle transport in the presence of a symmetric magnetic field. The fluid description has been widely used to study the particle transport. However, the fluid model does

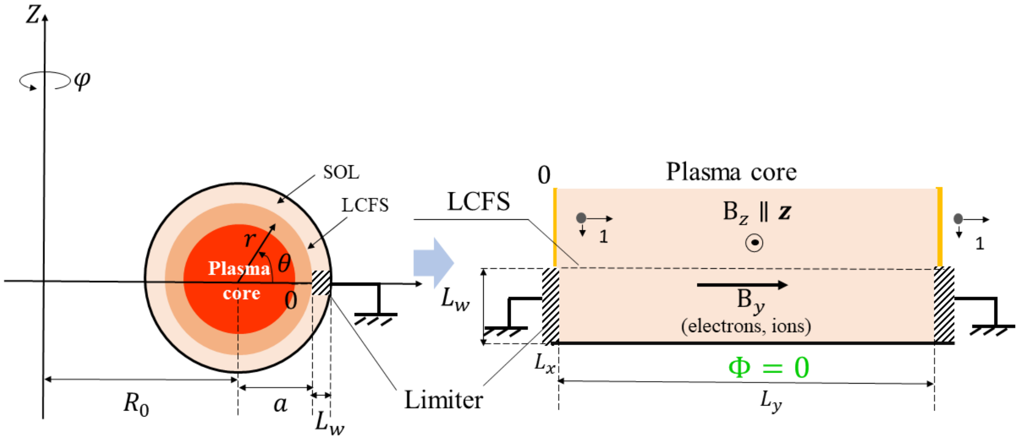

a) Torus geometry
(r, θ, φ)

b) Slab geometry
(x, y, z)

Figure 5.1: Simulation domain. Part a) shows the torus geometry for the toroidal limiter, whereas b) displays the slab geometry used in the simulation.

not include the drift effects. The effect of gyro motion and drift cannot be obtained by using the fluid model.

This chapter shows how the Larmor radius and aspect ratio affect the symmetry of the potential in the edge region using PIC simulation. Because PIC simulation uses the fully kinetic description, the drifts affecting the particle motion such as $\mathbf{E} \times \mathbf{B}$ and $\mathbf{B} \times \nabla \mathbf{B}$, and the particle gyro motion can be computed with high accuracy. We model a flow of plasma consisting of ions and electrons in the edge region by a 2D3V PIC simulation. We adjust the Larmor radius by changing its temperature and modify the inverse aspect ratio to alter the drift effects.

5.2 Simulation model

The basic model consists of a single, flat-sided toroidal ring limiter plasma. We consider a small region inside and outside the Last Closed Flux Surface (LCFS). In the scrape-off layer (SOL) region, the magnetic field line is opened. For simplicity, the SOL has been straightened out; the torus geometry is transferred to a two-dimensional slab geometry, as shown in Fig. 5.1. Figure 5.1 a) shows the torus geometry we want to study, while Fig. 5.1 b) displays the transferred slab geometry of the torus that is used in this work. The simulation domain has a small size, $L_x = 0.06\,\mathrm{m}$, including $L_w = 0.03\,\mathrm{m}$, which is the length of the limiter, and $L_y = 1.0\,\mathrm{m}$ in the y direction. We assume that the limiter is connected to the ground and the electric potential at $x = L_x$ is zero. The electric potential at $x = 0$ is assumed to satisfy floating potential conditions. Particles are fully absorbed at the limiter and at the end boundary, $x = L_x$. Inside the LCFS where $x < L_w$, a periodic boundary condition is used at the two boundaries in the y direction, in which the new position of a particle, which is out of the simulation domain at time t, is computed as $y^t_{new} = y^t_{old} - L_y$ for $y^t > L_y$ or $y^t_{new} = y^t_{old} + L_y$ for $y^t < 0$. Ions and electrons with real mass ratio $m_i/m_e = 1836$ are included in this simulation. The collision of charged particles is approximated by the Monte Carlo method. We consider the Coulomb collision between ion–ion, electron–electron and electron–ion. The Coulomb collision is treated as a successive binary collision using Nanbu's theory of Coulomb collisions [60]. The radial, poloidal, and toroidal magnetic fields (B_r, B_θ, B_ψ) in a torus correspond to B_x, B_y, B_z in the two-dimensional slab geometry, respectively. Consequently, an approximation with a torus configuration for the poloidal and toroidal magnetic fields in the simulation system can be written as follows:

$$\begin{aligned} B_\theta = \frac{rB_z}{R_0 q_s} &\to B_y = \frac{B_{0y} a}{2 + 2(\frac{x+a-x_w}{a})^2}, \\ B_\psi = B_{0z}(1 - \epsilon \cos\theta) &\to B_z = B_{0z}\left(1 - \frac{x + a - x_w}{R_0} \cos(\frac{2\pi y}{L_y})\right), \end{aligned} \tag{5.1}$$

where q_s is the safety factor adopted as $q_s = 2$. $a = 0.2\,\mathrm{m}$ and $R_0 = 1.0\,\mathrm{m}$ are the minor and major radii of the torus, $\epsilon = a/R_0$ is the inverse aspect ratio, $B_{0y} = B_{0z} = 1.0\,\mathrm{T}$ is the applied magnetic field, and $x_w = L_x - L_w$, respectively. We do not consider the magnetic field in the x direction in this simulation (i.e., $B_x = 0$ T). This magnetic field is depicted in Fig. 5.2. The poloidal magnetic field B_y depends on x only. The toroidal magnetic field is symmetric in the y direction from the mid line $y = L_y/2$. In a torus, the

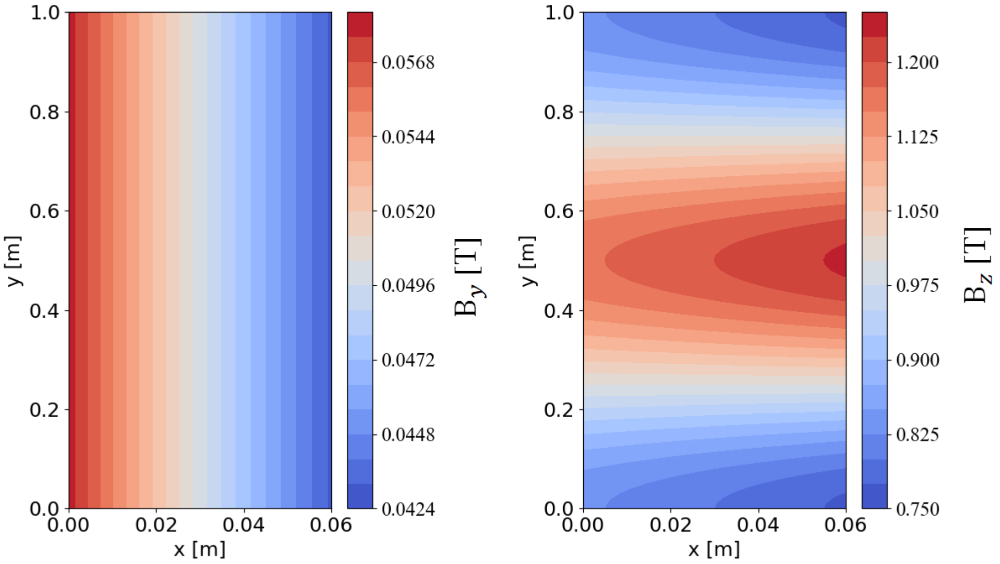

Figure 5.2: Poloidal and toroidal magnetic fields in the simulation domain. This profile of the magnetic field includes the curvature drift and toroidal gradient. B_y is dependent only on the x position, whereas B_z is symmetric in the y direction from the mid-line $y = L_y/2$.

field includes the toroidal effects. The toroidal magnetic field varies as $1/R$ because of the toroidicity. The toroidal magnetic field is strong inside the torus and weak outside. For the slab model, the magnetic field B_z, then, is high in the middle region and low near the limiters. Even though the values of all input parameters are not as exact as in any real devices, this profile of the magnetic field includes a toroidal gradient and curvature drift similar to the torus geometry. Therefore, the acquired physics behaviors of particles from this small simulation system can illustrate the basic physics behaviors in the torus configuration.

At an initial stage, the particle density n_s and temperature kT_s of species s are given as the exponential function in the x direction and uniformly in the y direction. They are given as:

$$\begin{aligned} n_s(x) &= n_{s,\mathrm{LCFS}} \exp\left(-\frac{x - x_w}{\lambda_n}\right), \\ kT_s(x) &= kT_{s,\mathrm{LCFS}} \exp\left(-\frac{x - x_w}{\lambda_{kT}}\right), \end{aligned} \tag{5.2}$$

where $\lambda_n = 0.02\,\mathrm{m}$, $\lambda_{kT} = 0.03\,\mathrm{m}$ are the scale lengths of the density and temperature profiles, and $n_{s,\mathrm{LCFS}}$, $kT_{s,\mathrm{LCFS}}$ are the particle density and temperature of species s at the LCFS, respectively. The initial velocity of the particles follows a fully Maxwellian distribution function driven from the initial temperature. We adopted $n_{s,\mathrm{LCFS}} = 4 \times 10^{17}\,m^{-3}$ for both ions and electrons through all the simulations in this work. For charge neutrality, we fix the total number of particles to be always constant in time. To do that, the reflection and injection conditions are applied for particles quitting the simulation box, except for those exiting at the periodic boundary inside the LCFS. If a particle is emitted (i.e., $x < 0$), it will be reflected back into the simulation domain. When a particle is absorbed at the limiters or end boundary, a new particle is injected randomly into the region inside the LCFS, using the thermal velocity function based on the initial temperature. Because the plasma has a high density and temperature inside the LCFS and is low on the outside, the plasma slowly diffuses across the LCFS and deposits on the limiter surface, owing to the high parallel transport. Toroidal drifts and collision between charged particles with a random walk result in the perpendicular transport of particles in the straight magnetic field lines. The displacement associated with Coulomb collision is in the order of a Larmor radius $r_\mathrm{L} = mv_\perp/|q|B$. Because electrons and ions have different masses and velocities, their movements are different. The electric field is self-consistently induced and the potential is formed. The next section discusses how the grad-B drift and the Larmor radius affect the perpendicular transport of a particle. The drift and Larmor radius change the particle transport, and then change the symmetry of the potential.

a) Electron density

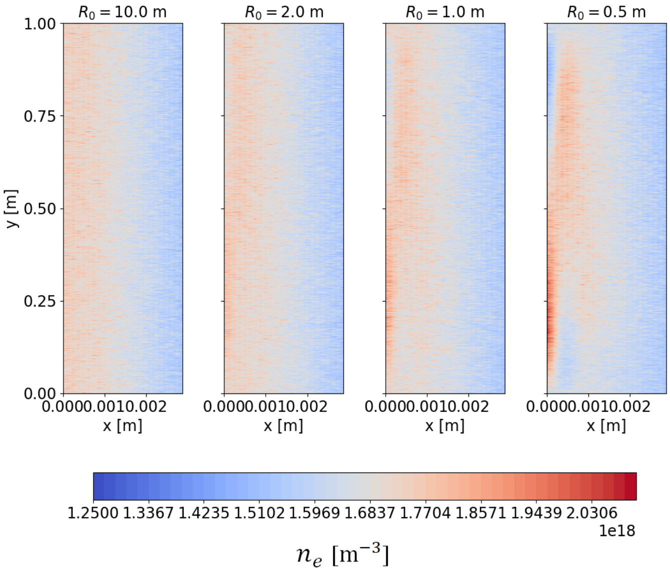

b) Ion density

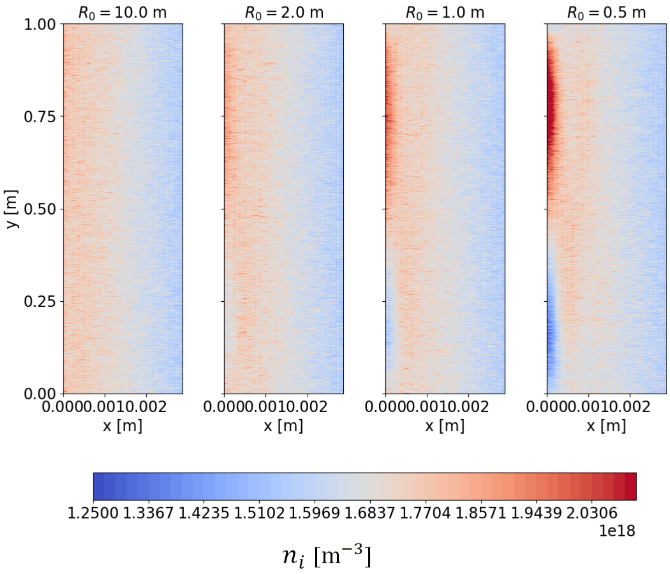

Figure 5.3: a) Electron and b) ion densities near $x = 0$ with different values of the major radius. The asymmetry of densities occurs when the major radius is small.

5.3 Simulation results

In this work, the magnetic field, initial temperatures and densities of particles are symmetric in the y direction from the mid-line $y = L_y/2$. Because the magnetic field B_z is stronger in the middle region and weaker near the limiter, the gradient of $|B|$ has an opposite direction to the mid-line $y = L_y/2$. Therefore, the direction of drift velocity for each species is opposite to the mid-line. To study the effects of this drift, different values of the major radius R_0 are used, while the minor radius remains unchanged ($a = 0.2$ m). These values of R_0 are adjusted such that the toroidal magnetic field is computed from Eq. 5.1, and are changed from the strong toroidal gradient to being approximately constant. When R_0 is small, the inverse aspect ratio is large, and the magnetic field has a strong toroidal gradient. In contrast, the magnetic field is nearly constant when the inverse aspect ratio is sufficiently small. In this case, the grad-B drift can be neglected. The toroidal gradient of the magnetic field is then dependent on the inverse aspect ratio.

The effects of $\mathbf{B} \times \nabla\mathbf{B}$ drift on particle motion can be captured in the PIC simulation, as displayed in Fig. 5.3. The defined lower region extends from 0 to $L_y/2$ and the upper one from $L_y/2$ to L_y. Owing to the grad-B drift, electron and ion transports have opposite directions. In the lower region, where ∇B has upward direction, ions have a tendency to move to the LCFS while electrons tend to enter the plasma core. Therefore, as can be observed in the bottom region of Fig. 5.3, near $x = 0$, the electron density is higher than the ion density. In contrast, in the upper region, where the ∇B has a downward direction, ions are forced to come to the plasma core, while electrons move into the LCFS. The ion density near $x = 0$ is higher than the electron density. The transaction in the upper region is opposite to that of the lower region. This movement is similar to that in the torus, in which because of the toroidal drift, ions will move upward and electrons will move downward in the (R, Φ, Z) coordinates of Fig. 5.1 a). The strength of grad-B drift depends on the value of $\mathbf{B} \times \nabla\mathbf{B}$. When the major radius is large, the gradient of the magnetic field is almost zero. The grad-B drift effect is extremely small, resulting in an invisible difference of

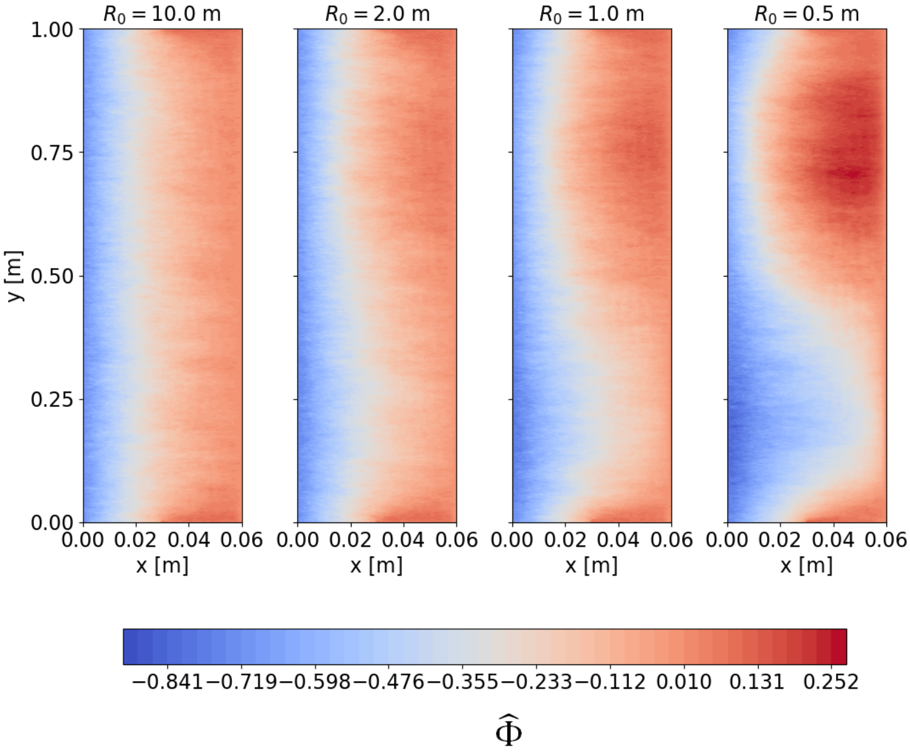

Figure 5.4: Potential profile formed in the simulation. In the large aspect ratio, the potential is symmetric from the mid-line $y = L_y/2$. The low aspect ratio breaks the symmetric structure and causes the asymmetry of the potential from the mid-line.

particle densities between the upper and lower region. When the major radius is small (e.g., $R_0 = 0.5\,\mathrm{m}$), the strong grad-B drift acting on each species leads to a clearer difference of particle densities between these two regions. Consequently, with a reduction of the major radius, the opposite transaction of each species in the upper and lower region becomes stronger. Because the distributions of electron and ion densities are changed, based on the grad-B drift, as computed by Eq. 2.5, the potential profile is different in the lower and upper regions.

Figure 5.4 displays the electrical potential profile in the simulation domain with different values of the inverse aspect ratio. In the case of a small inverse aspect ratio, the grad-B drift is almost zero for each species. The movements of particles in the upper and lower region are nearly familiar. Therefore, the potential is nearly symmetric in the y direction from the mid-line. In other words, when a smaller major radius is used, a greater value of the inverse aspect ratio is added, and the toroidicity of magnetic field B_z is stronger. Particle densities in the upper and lower regions are very different. In comparison with ion density, electron density is greater in the lower region but lower in the upper region, and the Laplacian of the potential profile has an opposite sign between these two regions. As a result, the potential profile is asymmetric in the y direction from the mid-line in the strong magnetic field gradient. Consequently, the symmetry or asymmetry of the potential profile depends on the ∇B drift or the inverse aspect ratio. A greater value of the inverse aspect ratio breaks down the symmetry of the potential profile. Studying the symmetric torus configuration where the magnetic field is also symmetric from the mid-line, we obtain that the asymmetry of the potential profile comes from the grad-B drift. This is one of the advantages of PIC simulation, rather than a fluid model, when considering the drift effects. This result shows a clear relationship between toroidicity and asymmetry in the torus. The higher the toroidicity in the torus, the clearer is the asymmetry of the electrical potential.

In the straight magnetic field line system, transport of magnetized particles perpendicular to the magnetic field line is almost zero in the case with no collision and there are no drift effects. In this case, increasing particle tem-

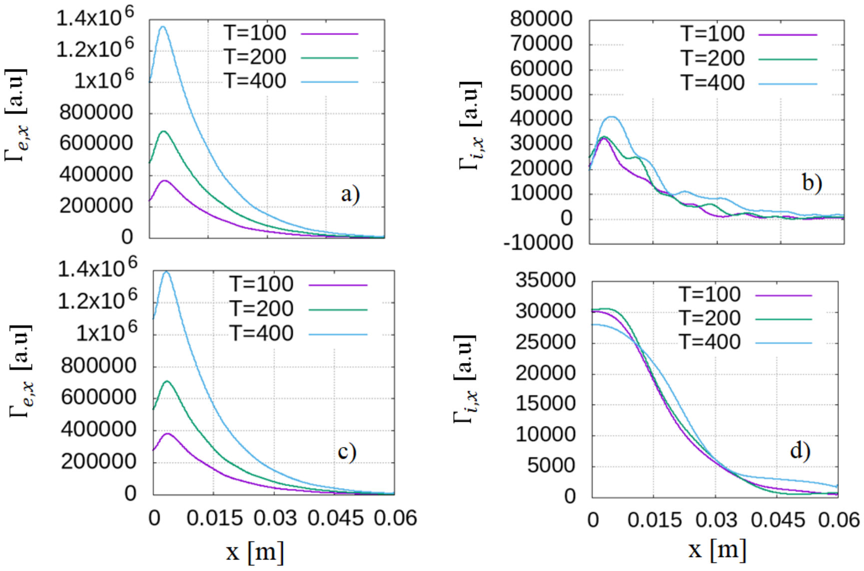

Figure 5.5: One-dimensional average of a), c) electron and b), d) ion fluxes in the x direction with different initial temperatures. The increase in particle temperature rises the radial flux to the LCFS.

peratures does not cause any significant effects in perpendicular transport, in other words, in the radial direction. When a collision between charged particles occurs, they are scattered in a random direction. The perpendicular transport, thereafter, may increase. It has been found that the shifted distance of the particles on the average of the guiding center is comparable to a gyro radius. In other words, the displacement of the particles after collision is in the order of the Larmor radius. The Larmor radius is one of the impacts affecting perpendicular transport of particles in the absence of a radial magnetic field. The Larmor radius affects losses of particles in the radial transport, and then changes the formation of the potential in the simulation. By changing the Larmor radius, the responded particle fluxes and potential formation are reflected. The same simulation domain and boundary conditions in the previous section are used here. To avoid the strong effects of grad-B drift in the simulation, the major radius is assumed to be extremely large, $R_0 = 10.0\,\mathrm{m}$. The grad-B drift is extremely small in the simulation domain. The Larmor radius is adjusted by changing initial temperatures of particles (i.e., changing $kT_{\mathrm{LCFS}} = kT_0$ in Eq. 5.2).

Based on the above assumptions, all the field quantities are also symmetric in the y direction from the mid-line. Therefore, it is reasonable to take one-dimensional average values for particle flux along the y direction from $y = 0.1$ to $0.9\,\mathrm{m}$, to study the effects of the Larmor radius on the perpendicular transport. The regions near the limiter have not been taken into account, to avoid the sheath potential effect in which the field quantities in these regions are different from those in other regions. Three different cases are considered: 1) changing only the electron initial temperature while keeping the same ion initial temperature, 2) changing the ion initial temperature and keeping the same electron initial temperature, and 3) changing both the electron and ion initial temperatures simultaneously. Figure 5.5 illustrates the electron and ion fluxes in the x direction with different initial temperatures. In the case of changing only the electron temperature and maintaining the same ion temperature, the electron radial flux increases with the increase in initial temperatures, as shown in Fig. 5.5 a). A similar behavior is observed for the ion flux in the case of changing ion temperatures while maintaining

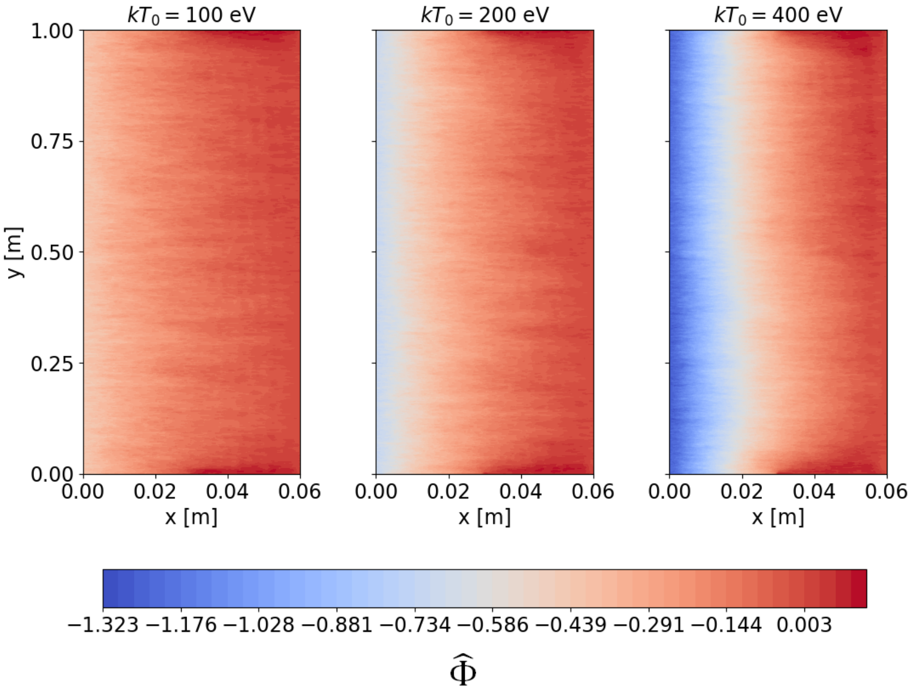

Figure 5.6: Potential profile when the initial temperature of electrons and ions are changed. The potential is symmetric in the simulation domain and has a deeper negative value near $x = 0$ when the higher initial temperature is applied.

the initial electron temperature. The ion radial flux increases when the ion initial temperature rises, as shown in Fig. 5.5 b). In the case of adjusting both the electron and ion initial temperatures simultaneously, the electron and ion Larmor radii change. The radial flux of the electrons and ions increases as the initial temperature rises as shown in Figs. 5.5 c) and d). In all three cases, if the particles have a larger Larmor radius, the perpendicular transport or the radial flux increases. The radial flux to the LCFS is proportional to the initial temperatures. Particles with high thermal velocity have a larger Larmor radius. Owing to the relationship between Coulomb collision and Larmor radius, a longer displacement in the perpendicular transport can be obtained with a larger Larmor radius. Larger Larmor radius changes the losses of electrons and ions across the LCFS and increases the radial transport in the simulation domain. The increase in radial particle transport affects the formation of the potential profile. The potential profile in the simulation domain using different initial temperatures kT_{LCFS} is displayed in Fig. 5.6. The case of changing both the electron and ion initial temperatures simultaneously is depicted in this figure. The same behavior of potential formation is obtained in the case of changing the initial temperature of only one species. Therefore, it will not be displayed again. Because of the extremely small grad-B drift, the electrical potential is symmetric in the simulation domain via the mid-line $y = L_y/2$. As the radial fluxes toward the LCFS increase, the electrical potential near $x = 0$ acquires a deeper negative value.

In all the above simulations, outside the LCFS where the magnetic field is opened, the potential near the limiter is higher than that in the middle region. This result is related with the injection conditions of the particle in the simulation. In the course of time, particles move along the straight magnetic field lines, and are lost at the limiters. Once a particle is lost, a new particle is injected in the closed magnetic field region in $x < x_w$. Because of their unbalanced mass and thermal velocities, the number of electrons lost at the limiter is larger than that of ions. Therefore, electrons dominate in the newly injected particles in each time step. Because an electron has a negative charge, the charge densities in the closed magnetic field region becomes negative. The potential in this region might be negative or close to zero. At several time intervals from the initial stage, the number of lost electrons is greater than that of ions, and might be nearly equal once the simulation reaches the equilibrium stage. Therefore, the number of electrons remaining near the limiter is smaller than the number of remaining ions, whereas there are more electrons than ions in the closed magnetic field region and the middle region. Accordingly, the charge density near the limiter becomes positive. The potential profile has an open downward parabola curve because the Laplacian of the potential should be negative. The potential near the limiter therefore is higher than in the middle region in the open magnetic field region.

5.4 Summary and discussion

A small region inside and outside the LCFS has been considered to study the potential formation in a two dimensional magnetic field configuration, using a 2D3V PIC model. A 2D slab geometry is used to model the torus configuration. The magnetic field used in this slab simulation contains the curvature and toroidal gradient, which are symmetrical in the poloidal direction about the limiter. We use the PIC simulation because it can deal explicitly with the magnetic drifts and compute exactly the particle orbit to study the effects of grad-B drift and finite-size Larmor motion on the potential formation. The asymmetry of the potential profile has been found to be dependent on the toroidicity of the torus. A higher inverse aspect ratio increases the toroidicity of the magnetic field, and then, reinforces the grad-B drift in the simulation domain. Because the direction of grad-B drift for each species is opposite in the two regions separated by the middle line $y = L_y/2$, the particle motions in these regions are in contrast to each other. Subsequently, the symmetry of the potential profile breaks down with a large inverse aspect ratio. The potential profile is asymmetric when the plasma is under a strong influence of grad-B drift. The relationship between the Larmor radius and potential formation is also obtained in this study. In the case of straight magnetic field lines and negligible grad-B drift, the perpendicular transport of particles depends on collision. The particle after collision is shifted with a distance comparable to the Larmor radius. The number of lost particles at the LCFS increases for larger Larmor radius. The significant particle loss enhances the radial transport and forms a deeper negative potential at the closed magnetic field line region. PIC simulation is a more useful model to capture all of these relations than other numerical models. In this PIC model, the radial magnetic field can be added to create magnetic islands. We will study the relationship between potential formation and magnetic islands in the next chapter.

Chapter 6

Potential formation with 3D magnetic field

6.1 Magnetic island in the slab geometry

Extending from the study on the two-dimensional (2D) magnetic field in the previous chapter, here, we concentrate on the effects of the three-dimensional (3D) magnetic field or magnetic island. We still use the transferred slab geometry of the torus. The simulation region and boundary conditions are the same as in the simulation used in the previous chapter to study of the 2D magnetic field. Then, the toroidal magnetic field has the same function as that described in Chapter 5. The strong toroidicity of the torus has been taken into account. We use the major radius $R_0 = 1.0\,\mathrm{m}$ in this chapter. The initial profiles for the density and temperature of the electrons and ions are assumed to follow the exponential profile proposed in Chapter 5. The main difference in this Chapter is that we attempt to perform the magnetic island in the slab geometry system by adding the radial magnetic field. Transferring the magnetic island in the slab geometry, which is exactly as the magnetic island in the torus, is very complicated. To create the magnetic island in the simulation study, we follow the idea of injecting current filaments, as discussed in Chapter 4. This will not give exactly the same magnetic island configurations as those in the torus but can help us to understand the ba-

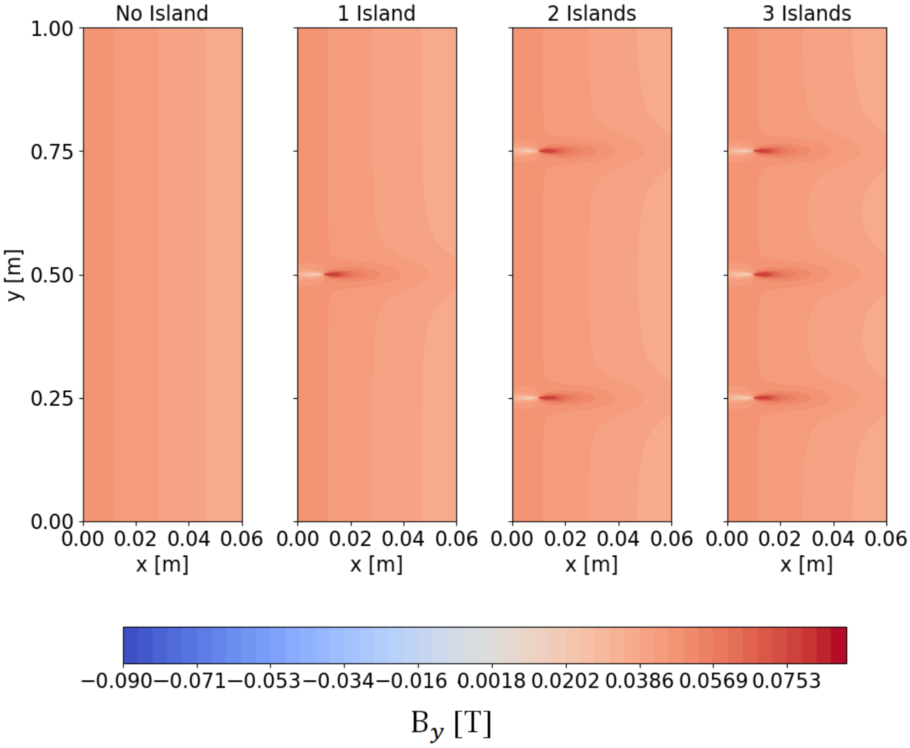

Figure 6.1: Poloidal magnetic field after injecting current filaments. Different numbers of magnetic islands are used in the simulation to study the potential formation.

sic principles of the relationship between potential formation and magnetic island. The current filament is injected in a direction perpendicular to the simulation plane (i.e., the z direction) to generate the radial and poloidal magnetic fields. The total poloidal magnetic field in the system will be the sum of the poloidal magnetic field presented in Chapter 5 and the magnetic field generated by the current filaments proposed in this Chapter. The number and location of magnetic islands can be adjusted based on the number and location of current filaments. Figure 6.1 shows an example of the poloidal magnetic field after adding $N_{current} = 0$, 1, 2, 3 filaments into the simulation.

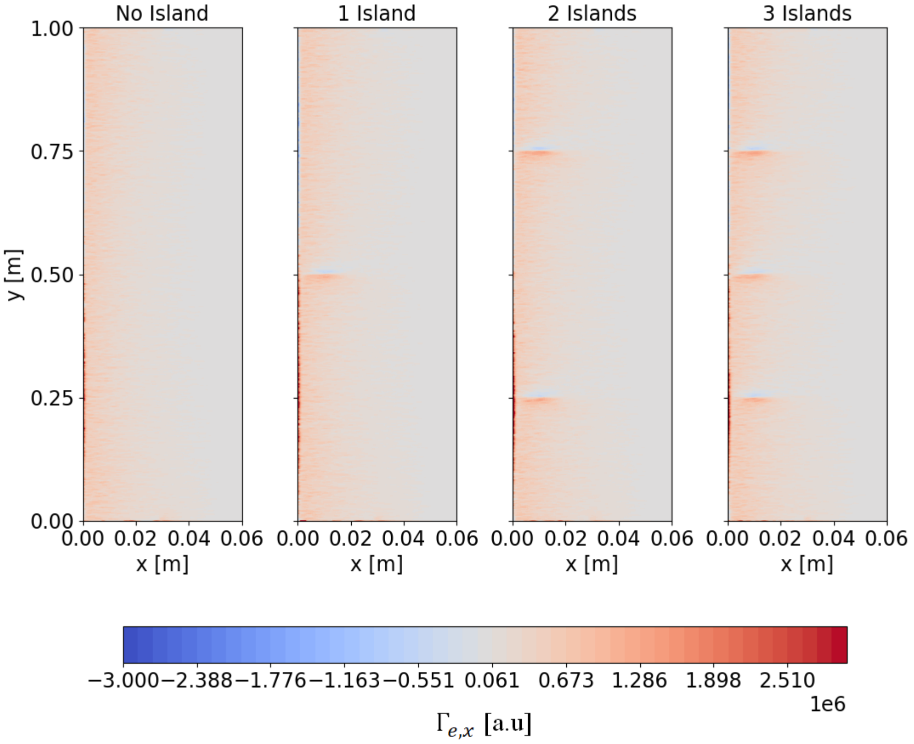

Figure 6.2: Electron radial flux with different numbers of islands.

The main reason for choosing these locations of current filaments rather than other position is the symmetric system in the poloidal direction about the limiter. The magnetic island is created in the closed magnetic field region rather than in the SOR region. We compare the field quantities with and without injecting current filaments to study how the particle transport will be changed in the presence of the magnetic island.

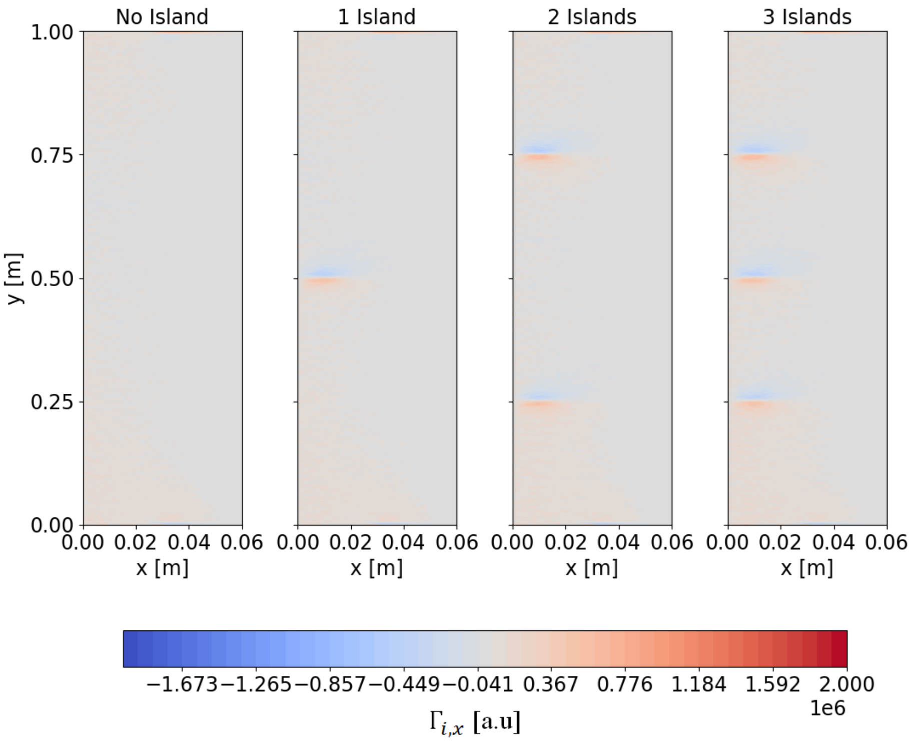

Figure 6.3: Ion radial flux with different numbers of islands.

6.2 Effects of magnetic island on particle transport and potential formation

The current filaments change the magnetic field in the radial and poloidal directions, and therefore, they mainly affect the particle flux in these directions. The magnetic field generated from the current filaments is computed by using the Biot–Savart law, given as

$$B = \frac{\mu_0 I}{2\pi r} = \frac{\mu_0 I}{2\pi\sqrt{(x - x_{\mathrm{I}})^2 + (y - y_{\mathrm{I}})^2}}, \tag{6.1}$$

where $\mu_0 = 4\pi \times 10^{-7}\,\mathrm{Tm/A}$ is the permeability of free space, I (kA) is the strength of the current, and x_{I} and y_{I} are the locations of the current

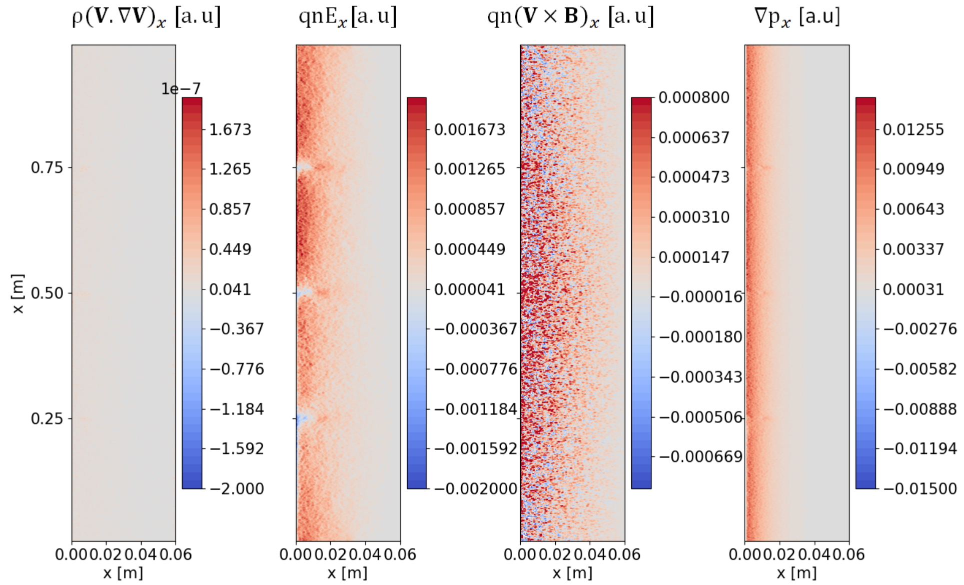

Figure 6.4: Convection terms in the x direction for the electron when using three current filaments.

filaments in the x and y directions, respectively. We inject the current in the edge region rather than in the SOL region for creating the magnetic island. At the beginning, we inject the same current strength $I = 1\,\mathrm{kA}$ for all of the filaments. The radial magnetic field, except near the injected current locations, is much smaller than the poloidal magnetic field. In comparison with the case of no magnetic island, the magnetic field structure mainly differs near the locations of the current filaments. In other regions, the magnetic structure is quite similar. As a result, the particle transport and particle flux are mainly changed in the region near the current locations compared to the case of without magnetic island. We compare the particle fluxes and densities with and without magnetic island based on the number and locations of the current filaments in Fig. 6.1. Figures 6.2 and 6.3 show the electron and ion radial fluxes in the presence of a magnetic island, respectively. In the case

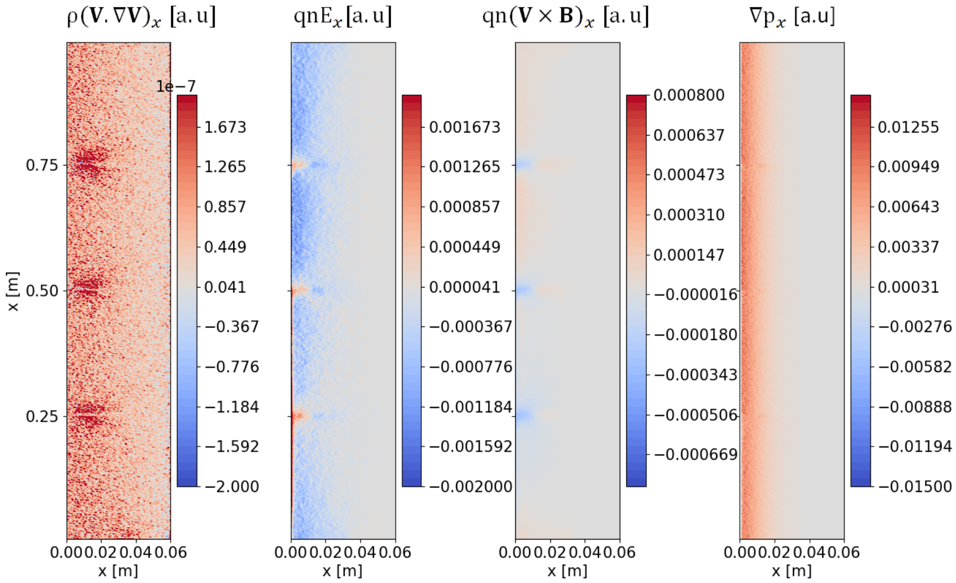

Figure 6.5: Convection terms in the x direction for the ion when using three current filaments.

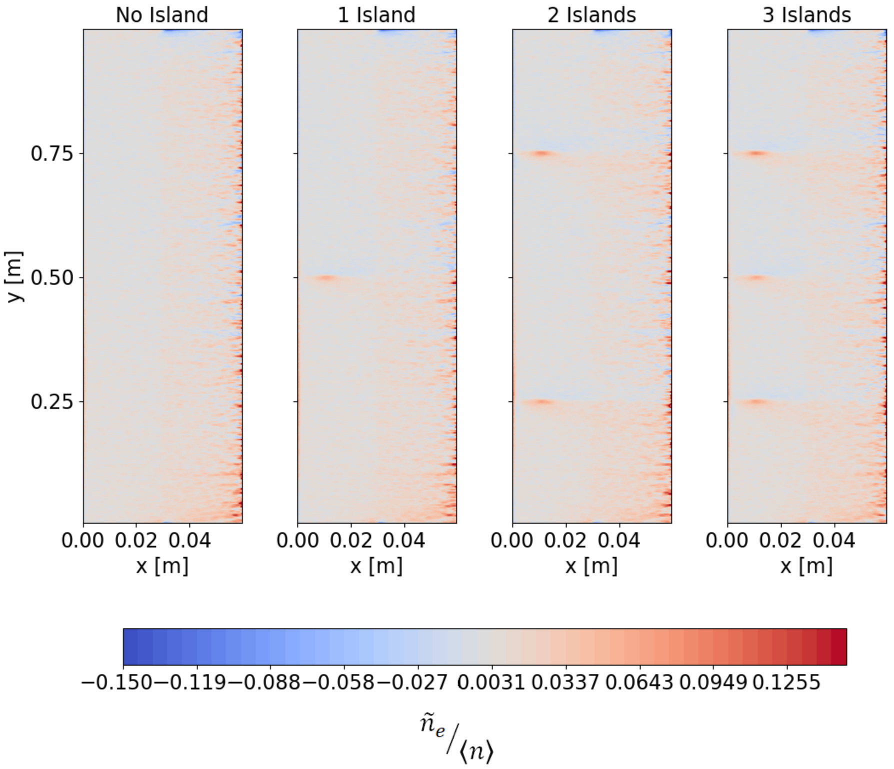

Figure 6.6: Fluctuation of electron density in the simulation domain.

of no magnetic island, the magnetic field line is straight in the y direction and there is no magnetic field in the radial direction. The radial transport, therefore, mainly comes from the particle diffusion and drift effects. Near $x = 0$, the particle profile has a strong gradient of density and temperature, then the radial flux around this region might be stronger than that in the SOL region. Once the current filament is added, the radial magnetic field appears. The radial magnetic field changes the radial flux. The direction of the radial particle flux is the same as the direction of the radial magnetic field. Once the radial magnetic field is negative, the particles have the tendency to move to the core region, whereas a positive B_x accelerates the particle motion. Electrons and ions show a similar influence on the flux while the

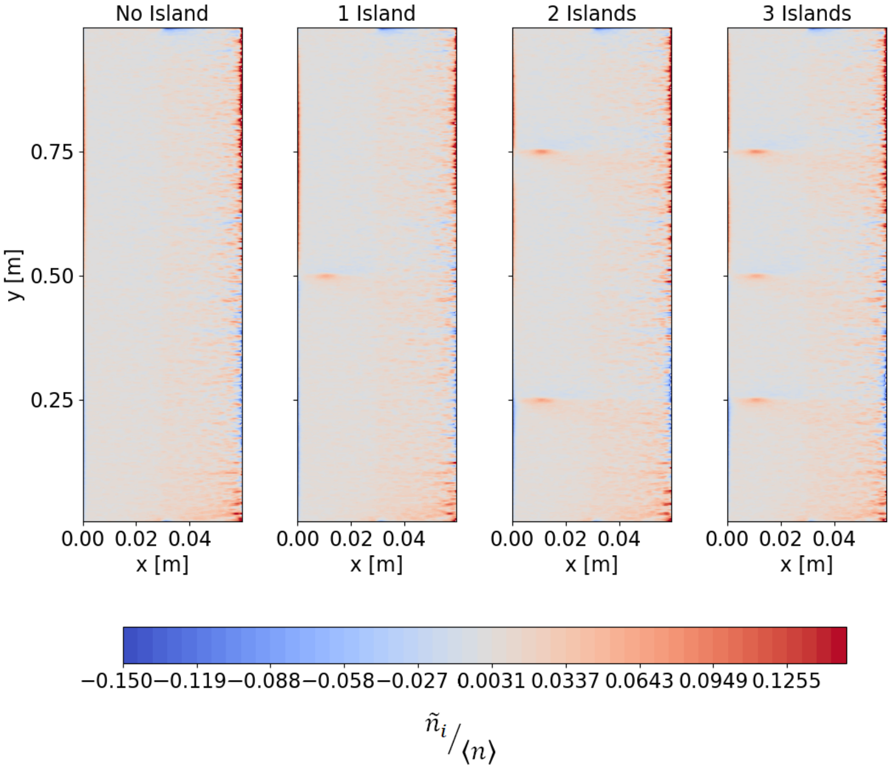

Figure 6.7: Ion density fluctuation in the simulation region.

current filaments are injected. The figure for the ion is more obvious than that for the electron. This arises comes from the much larger Larmor radius of ions than that of electrons. An electron has a much smaller Larmor radius, and hence it can move smoothly through the magnetic island. To clarify the effect of the magnetic field on the transport of each species separately, the convection terms for the electron are proposed in Figs. 6.4 and 6.5. Three injected current filaments are considered in these two figures. The convection term for the electric field, the qE term, has the opposite direction for the electrons and ions. The ∇P term shows the diffusion effect in the simulation domain. The strong ∇P term arises in the region where the gradient of the density and temperature is strong. From these two figures, we found that

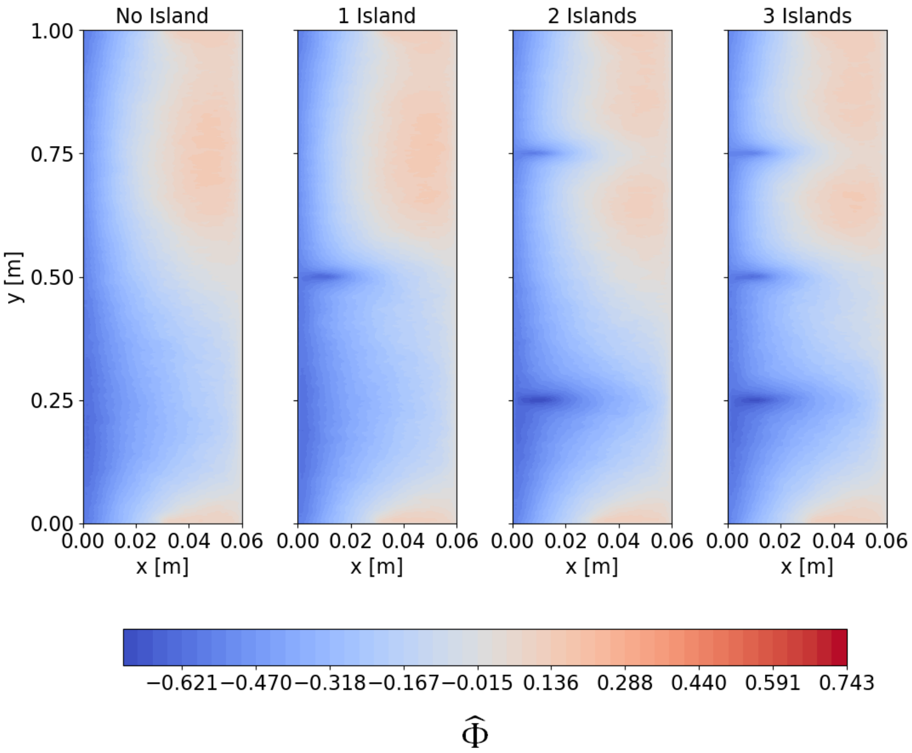

Figure 6.8: Potential formation in the presence of magnetic islands.

the $\mathbf{v} \times \mathbf{B}$ term near the magnetic island is more obvious for the ion than the electron. This occurs because ions are more sensitive to the change of the magnetic field than the electron due to the large Larmor radius.

Based on the different particle fluxes in the existence of the magnetic island, there is a possibility for the particle to be trapped in the magnetic island. Verifying the fluctuation of particle densities $\tilde{n}$ given as

$$\frac{\tilde{n}}{\langle n \rangle} = \frac{n(x,y) - \langle n(x) \rangle_y}{\langle n(x) \rangle_y}, \tag{6.2}$$

it was found that particle densities also change in the magnetic island region, in a similar way to the flux. The fluctuations of electron and ion densities are displayed in Figs. 6.6 and 6.7. Ion and electron densities change in comparison with the no island case. As they are affected by the particle flux, particles relocate their positions; the particle density changes by the magnetic island. Because the particle flux and density change, the potential is responsibly changed as depicted Fig. 6.8 As shown in Fig. 6.8, the potential profile is differently formed in the simulation box. The potential profile is changed near the location of the current filaments The radial transport is changed, and the potential obtains deeper negative values near the current locations. The changes in potential profile depend on the number of magnetic islands.

6.3 Magnetic island width

The size of the magnetic island is changed by adjusting the strength of the current filament. A greater island width occurs when the injected current filament has strong intensity. When the strength of the current filaments is weak, the magnetic island is formed in a smaller region. Once the current strength is close to zero, there is almost no island is created in the system. We inject different current strengths, such as $I = 0.1$, 0.5, and 1.0 kA, so that the total poloidal magnetic field is given as in Fig. 6.9. Three magnetic islands are under consideration. With $I = 1$ kA, the range of magnetic field change is larger than that of the case $I = 0.5$ kA, or smaller.

By comparing the radial flux of the particles, we discovered that the current strength or the magnetic island size alters the affected region of the particle fluxes near the magnetic island (as shown in Figs. 6.10 and 6.11). A weaker current filament does not cause huge impacts on the particle flux because the radial magnetic field is approximately zero in this case. The maximum value of the particle fluxes increases as the island width increases. The gap between positive and negative flux in the magnetic island location becomes greater. A tendency similar to that of the poloidal flux is obtained using different current strengths. Owing to the direction of the magnetic field generated by the current filament, the radial flux changes its direction between the top and bottom, whereas the poloidal flux changes direction at

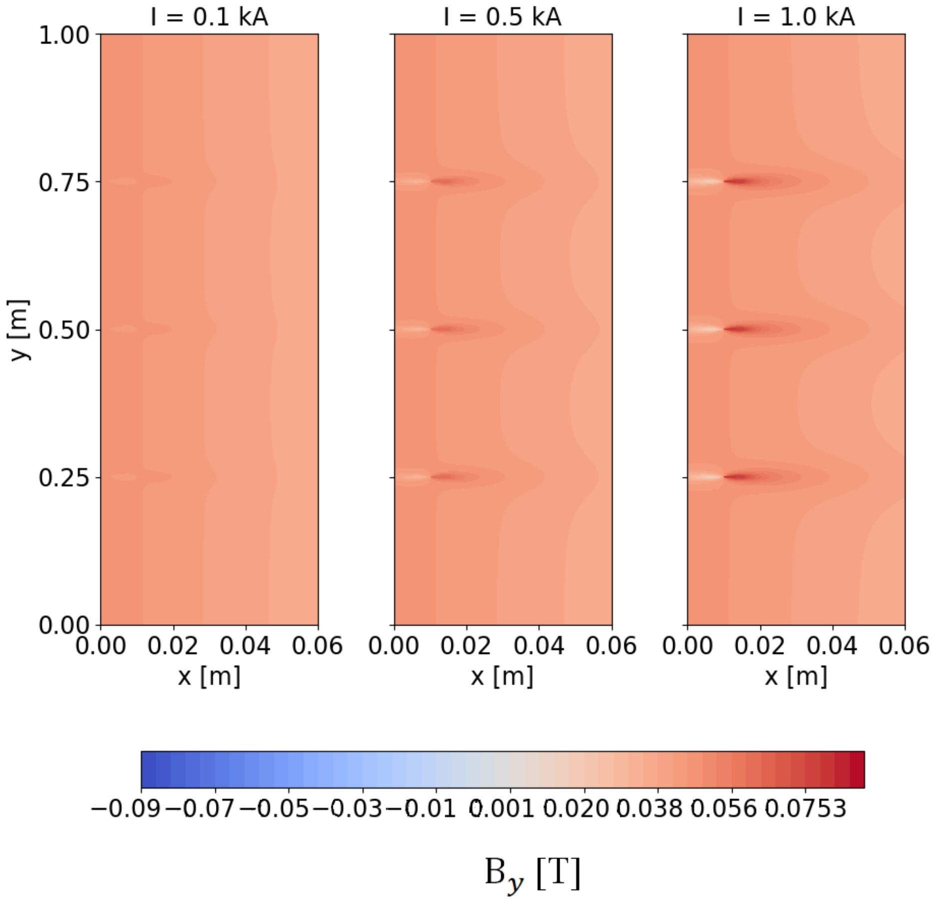

Figure 6.9: Poloidal magnetic field while changing the strength of the current filament.

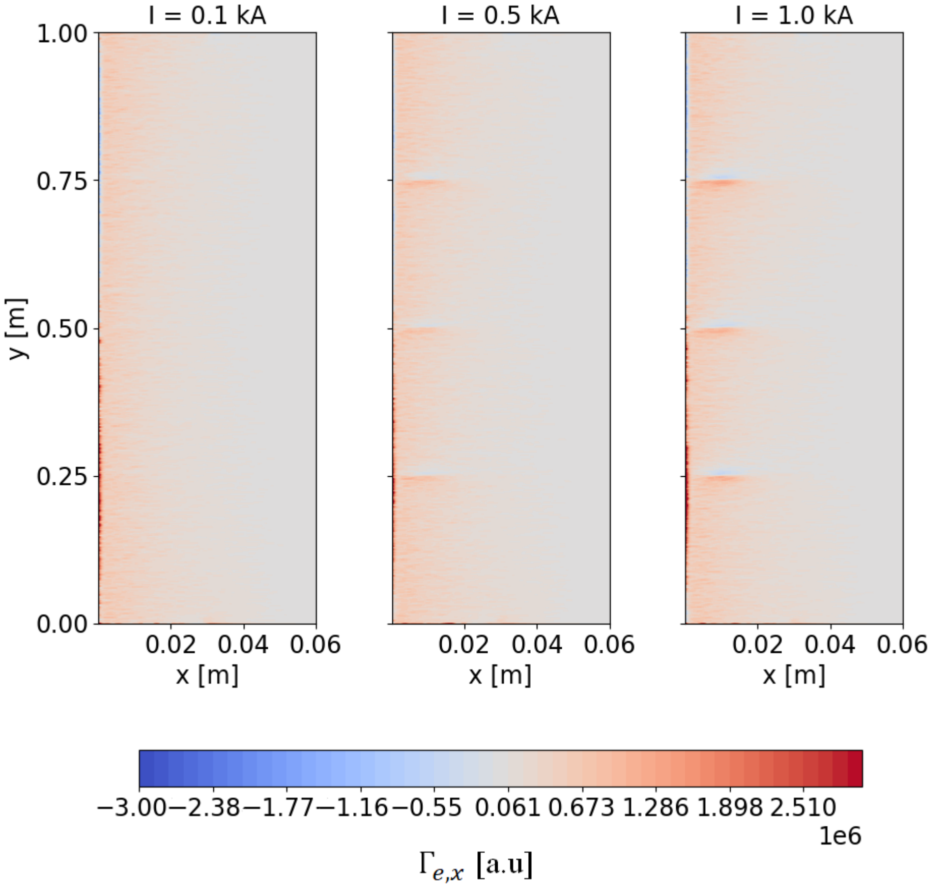

Figure 6.10: Electron radial flux with different current strengths.

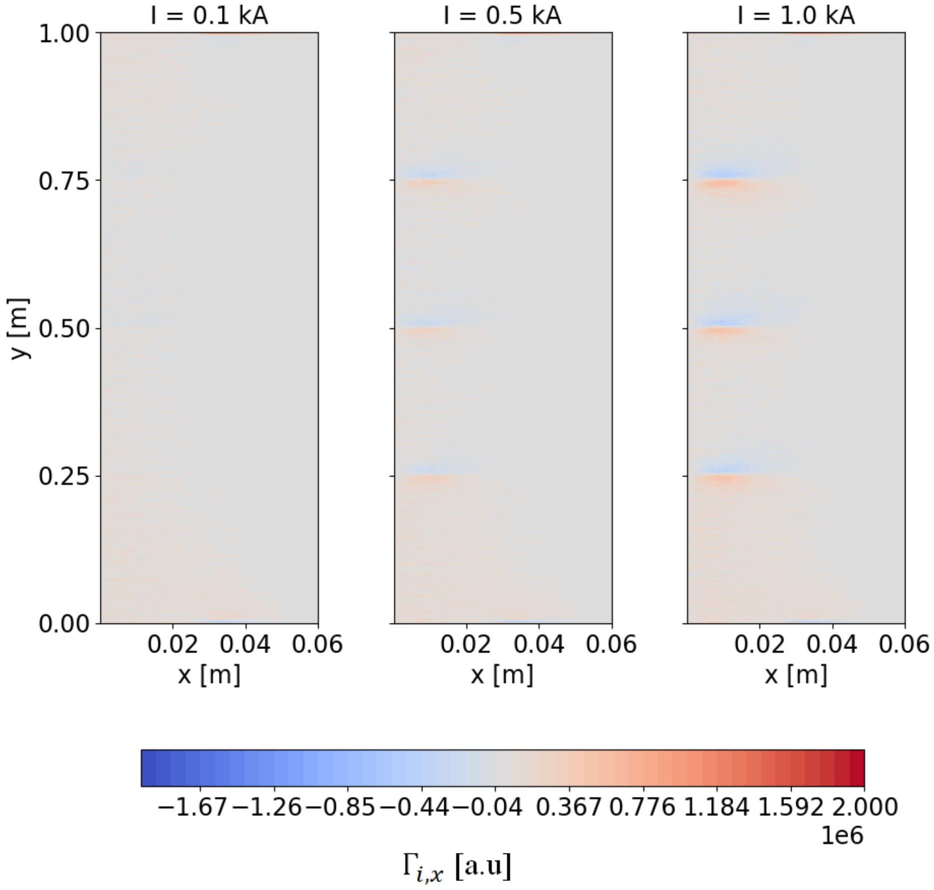

Figure 6.11: Ion radial flux with different current strengths.

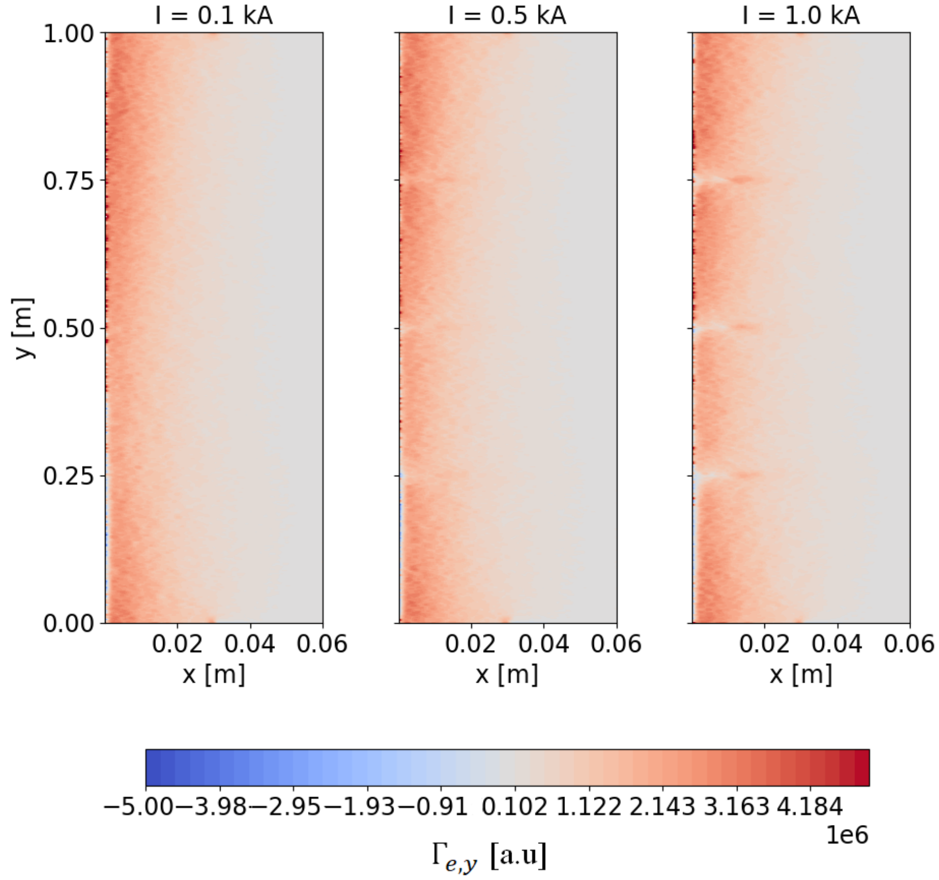

Figure 6.12: Electron poloidal flux with different current strengths.

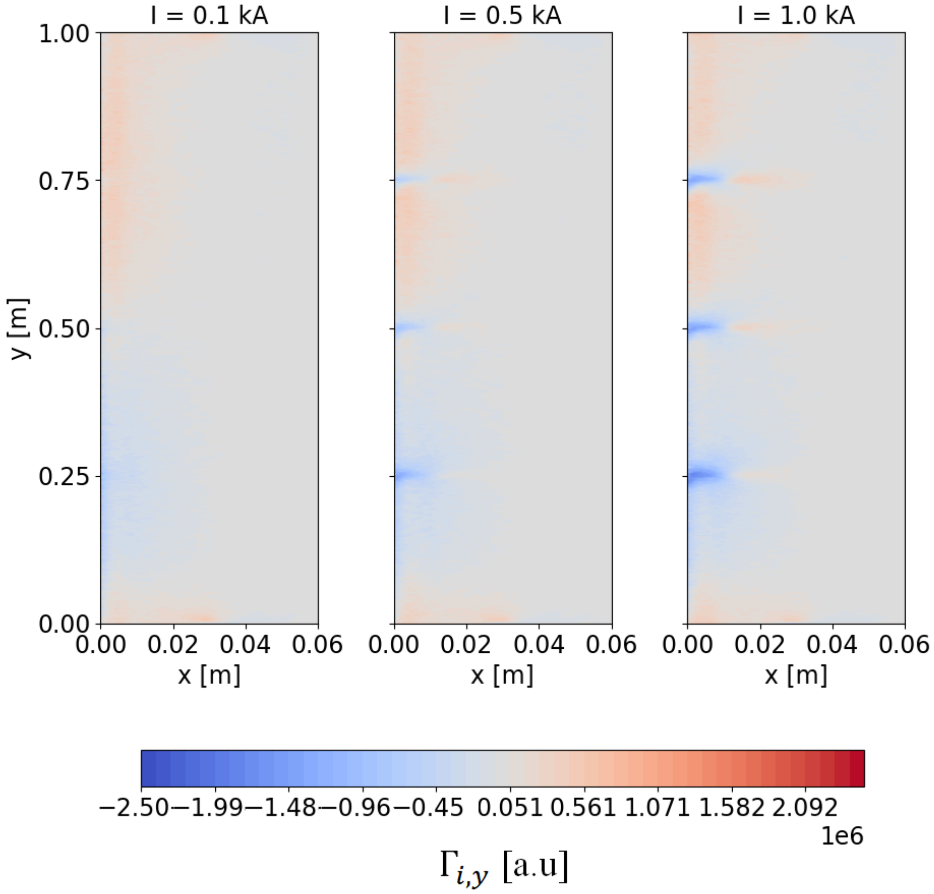

Figure 6.13: Ion poloidal flux with different current strengths.

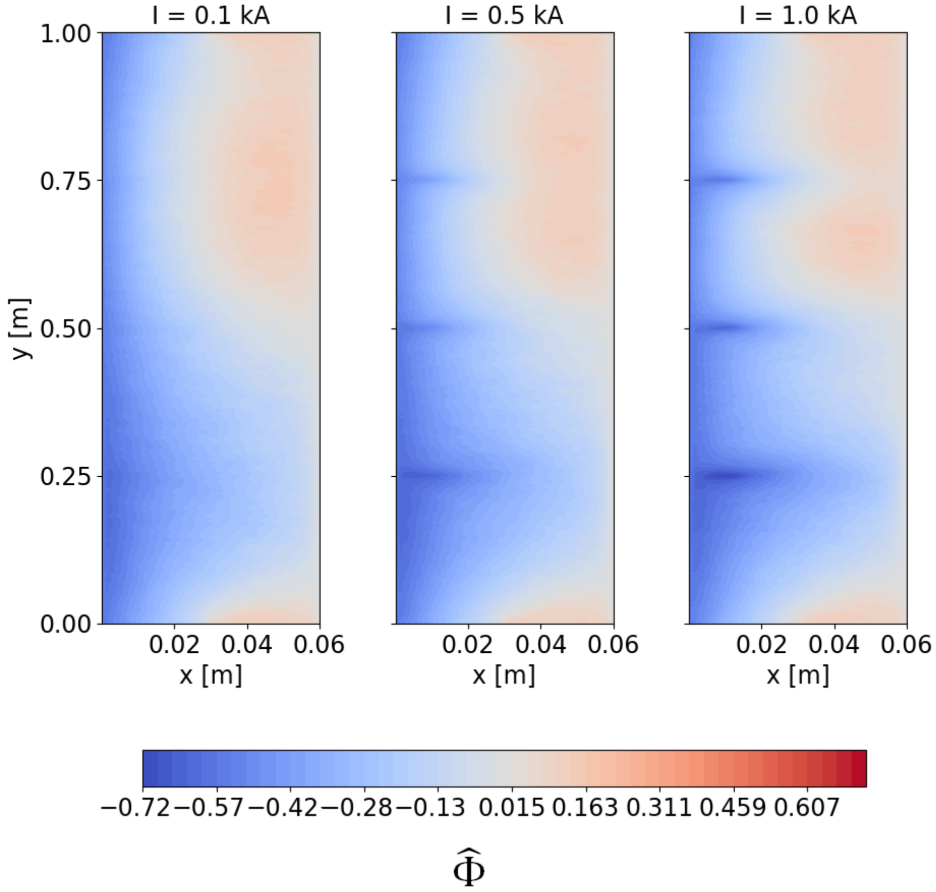

Figure 6.14: Potential formation in the presence of magnetic islands.

the left-side and right-side of the filaments locations. The potential profile clearly reflects this tendency. As plotted in Fig. 6.14, the stronger difference in the potential profile comes from the wider size of the magnetic island. As explained in theory works, the magnetic island changes the divergence of the radial and poloidal magnetic field near the island location. The magnetic island changes the particle transport, maintains the particles in the islands, and then changes their fluxes in both the radial and poloidal directions. The changes in the particle flux affect the formation of the potential.

6.4 Stochastic field and potential formation

A complex phenomenon in the edge plasma region is the existence of the stochastic field. The stochastic field is created to control the instabilities in the edge region. Many experiment works have been performed to study the effects of the stochastic field on particle transport [8, 61, 62]. It has been indicated that the self-consistent radial electric field is one of the essential factors to understand the self-consistent RMP penetration physics [61]. We studied the effects of the stochastic field on the self-consistent potential formation in edge plasma in the numerical simulation. Thanks to the advantages of PIC simulation, the radial electric field or the potential profile is self-consistently computed in the PIC model. The stochastic field occurs when the magnetic islands overlap. The right hand side figure in Fig. 6.15 shows an example of magnetic overlap for generating the stochastic field in the simulation. Rather than performing any complex and complicated stochastic field system as in the real tokamak device, our work focuses on a simple model of the stochastic field. This simple model helps to understand the fundamental principles of how the plasma behaves when magnetic islands overlap. Understanding these basic properties helps explain the complicated plasma behaviors in realistic devices. Considering the simulation where the stochastic field is as shown in Fig. 6.15, when overlapping of the magnetic island takes place, particles can move from one stochastic field to another if the perpendicular velocity is stronger than any drift effects. Similar to the effect of a mag-

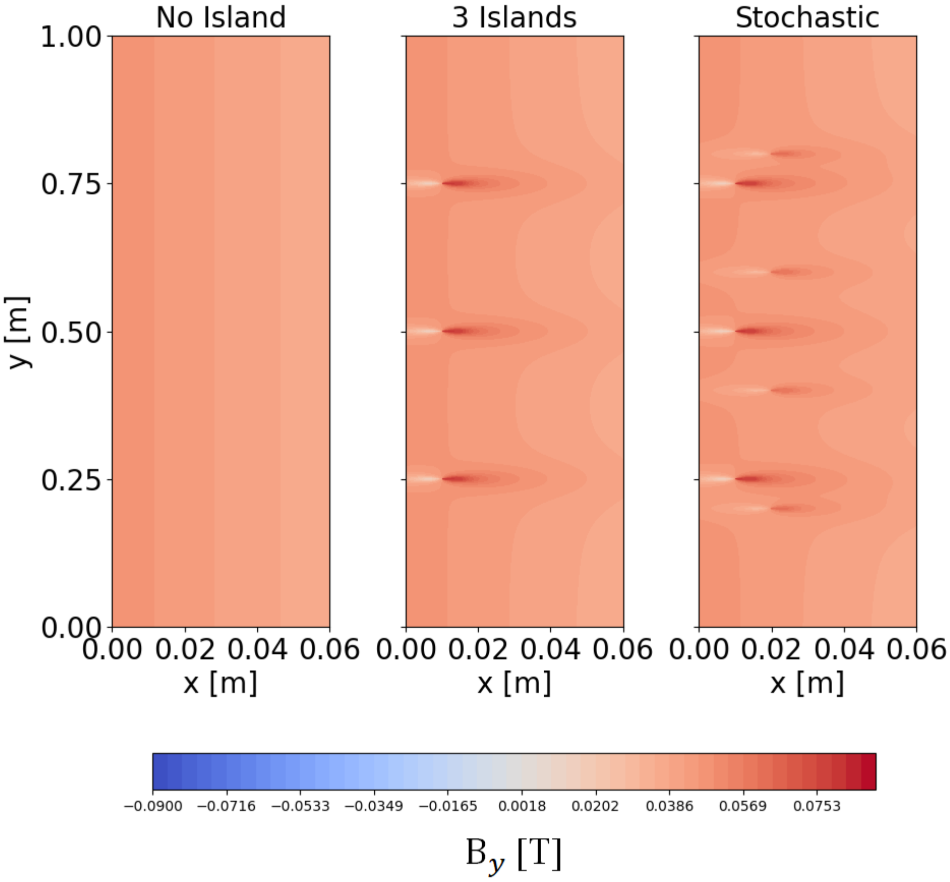

Figure 6.15: Poloidal magnetic field in the cases without magnetic island, with magnetic island, and with stochastic field.

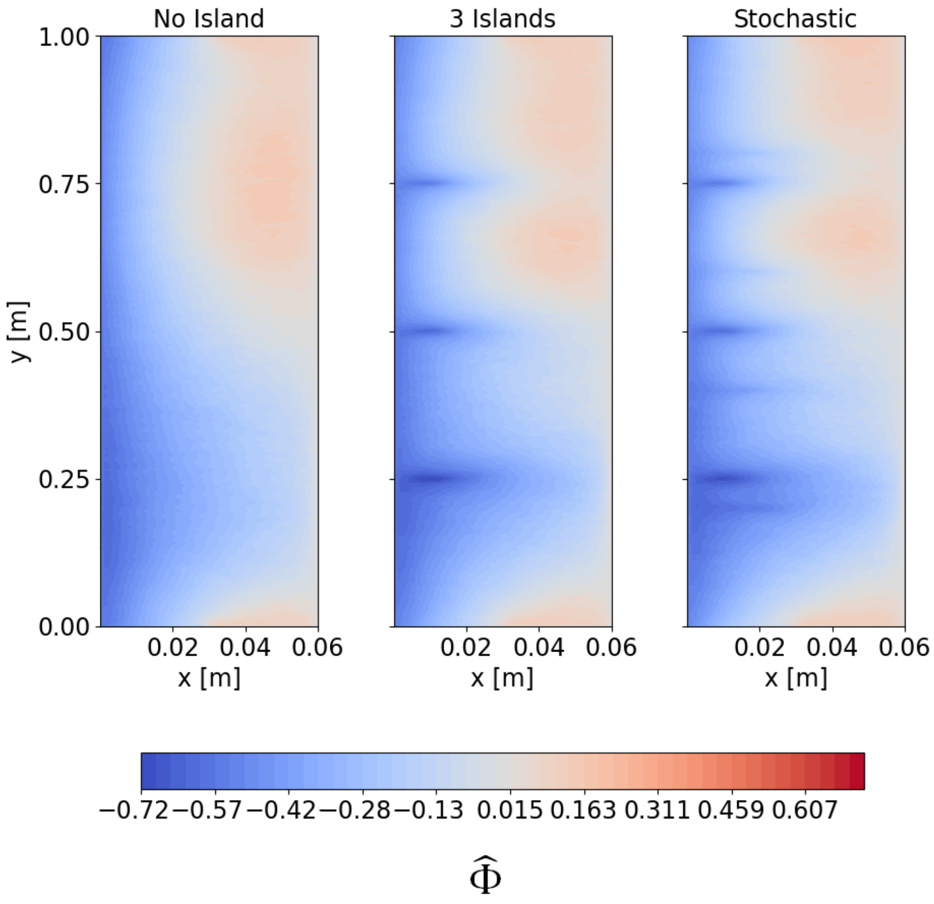

Figure 6.16: Comparison of potential profile in the system between the cases without magnetic island, with magnetic island, and with stochastic field.

netic island on particle transport, the flux and density of the particles are strongly influenced in the presence of the stochastic field. The changes in the particle flux are reflected in the change in the formation of the potential. The potential profile of the simulation system is affected compared with the case of no island, as shown in Fig. 6.16. Magnetized particles move along the field line with gyro motion. In other words, once the stochastic field is dense, the magnetic field line fluctuates strongly, and the particle transport is significantly affected, leading to undesirable behaviors. Therefore, based on the simulation results, a fundamental relationship between the stochastic field and potential formation is proposed.

6.5 Summary and discussion

A small region inside and outside of the LCFS in the torus, which is transferred to the two dimensional slab geometry, is studied using a PIC simulation. All three components in the radial, poloidal, and toroidal directions of the magnetic field are considered. The effects of the magnetic island on the particle transport and potential formation are mainly discussed in this Chapter. The current filament is injected into the simulation domain to generate magnetic islands. Although this magnetic island profile cannot express exactly the magnetic islands in real tokamak, the profile gives us a fundamental understanding of the effect of the magnetic island on potential formation in the edge plasma. The magnetic island traps the particles by changing the particle fluxes in both radial and poloidal directions. Therefore, the magnetic island changes the structure of the potential profile in the edge plasma. The region of the affected potential profile is related to the width of the magnetic island. A larger magnetic island traps more particles inside the island, leading to an unbalance in particle density inside and outside of the magnetic island. As a result, the formation of potential is changed. A simple model of the stochastic field is also presented in this Chapter, where the stochastic field is expressed by the overlapping of magnetic islands. The impacts of the stochastic field on potential formation can be explained based on that of the magnetic island. This is the initial work for studying the potential formation in the edge plasma using PIC simulation. Our study is the fundamental research to understand the impact of the magnetic island on the formation of potential. The relationship between the potential formation and magnetic field is clearly showed. The effects of the magnetic island on the particle transport in the edge may be predicted based on this foundation. The magnetic island of the tokamak is not modelled precisely in the 2D slab geometry when using the current filaments. A model closer to a realistic structure is necessary to consider more quantitatively the effects of the magnetic island on potential formation in the real tokamak. The new model of a magnetic island is discussed in Appendix A. This new model does not exactly generate the magnetic island structure as that in the tokamak yet. However, the new model is appropriate for studying how the magnetic island affects the particle transport in a numerical study.

Chapter 7

Conclusion and discussion

The relationship between magnetic field, particle transport, and potential formation in the edge plasma is presented numerically in our study. To study the self-consistent potential formation in edges plasmas, we develop a PIC simulation code, which uses a fully kinetic description. This is a completely new PIC code because the previous codes are not suitable for our set-up simulation conditions and domain when considering the complicated structures of a toroidal limiter and including the edge magnetic fields with magnetic islands. The process of code development starts from developing a 1D3V PIC simulation code. Then, the 2D3V PIC code is extended from the 1D code. This code development process provides a simpler way to build the 2D3V PIC code rather than developing 2D3V PIC code directly at the beginning. We apply our PIC model to study the effects of the external magnetic field on particle and heat fluxes to the wall targets. In the one dimensional case, the external magnetic field, which is localized and switched from strong negative values to strong positive values at several locations in the simulation region, can control the particle and heat fluxes to the wall. The reduction in fluxes arises from particle reflection at the locations of the strongly localized magnetic field. The external magnetic field forms magnetic mirrors. These magnetic mirrors trap the particles in the simulation domain, and then reduce the particle and heat fluxes to the wall targets. We also perform the same simulation using the 2D3V PIC model. A similar external magnetic field is added by injecting current filaments perpendicular to the plasma flow. Because a strong gradient of the magnetic field occurs near the locations of the injected current filaments, a magnetic mirror forms in between the current filaments. The electrons and ions trapped in the magnetic mirror change the particle and heat transport. Therefore, the high particle and heat fluxes to the wall are reduced and transferred along the wall by applying the current filaments. Injecting current filaments is a good option to reduces the high heat flux to the material.

We parallelize the 2D3V PIC code to study the relationship between magnetic field and potential formation in the edge plasma. The parallelization of the code is needed because PIC consumes a large amount of time and requires huge computer memory when dealing with a large system. To save the computing time and memory, we parallel the code to study the entire edge plasma region. A small region inside and outside the LCFS is considered. The two-dimensional slab geometry is used to model the torus configuration. We find that the particle transport is related to the magnetic configuration. The perpendicular transport of particles depends on the drift and collision between charged particles. The toroidicity of the torus or the Larmor radius of the particle changes the potential structure. We also find that the inverse aspect ratio or the toroidicity of the torus changes the asymmetry of potential in the symmetric system, whereas the Larmor radius affects the potential values in the closed magnetic field region. These behaviors are obviously obtained using the PIC simulation, but cannot be captured using any other fluid theory. To consider the effects of three-dimensional magnetic fields, the radial magnetic field is added to create magnetic islands. In our work, we add current filaments into the simulation system to form the islands. The magnetic islands affect the particle transport to change the particle fluxes, and then, cause differences in the formation of potential. This is the initial work for studying the potential formation in the edge region by using a PIC simulation. Comparison with realistic experiments, the exact configuration of the magnetic island in the torus must be included. Then, an improvement in the magnetic island generator in the simulation study should be carefully considered.

Appendix A

Particle transport in the magnetic island created by the Fadeev equilibrium

Fadeev proposed a formula to make the magnetic islands [63, 64]. The magnetic island can be generated as

$$\begin{aligned} B_x(x,y) &= \frac{\epsilon B_0 \sin ky}{\cosh kx + \epsilon \cos ky + \alpha}, \\ B_y(x,y) &= \frac{B_0 \sin kx}{\cosh kx + \epsilon \cos ky + \alpha}, \end{aligned} \tag{A.1}$$

where ϵ and k are the real parametrization parameters and $0 < \epsilon < 1$, α is the phase space angle, and B_0 is the magnitude of the magnetic field. The width and number of magnetic islands depend on the values of ϵ and k. As only the magnetic field line is considered, the Fadeev equilibrium models the magnetic islands well with clear X-point and O-point as shown in Fig. A.1. However, the poloidal magnetic fields B_y in the left-side and right-side of the magnetic island have the opposite directions. This makes the Fadeev model unrealistic as compared with the real tokamak configuration. The Fadeev equilibrium does not exactly perform the magnetic structure in the tokamak, but the equilibrium is a good model to study the influences of magnetic islands on particle transport in a numerical study. We perform the magnetic island in the 2D system bounded in the x direction and periodic in the y

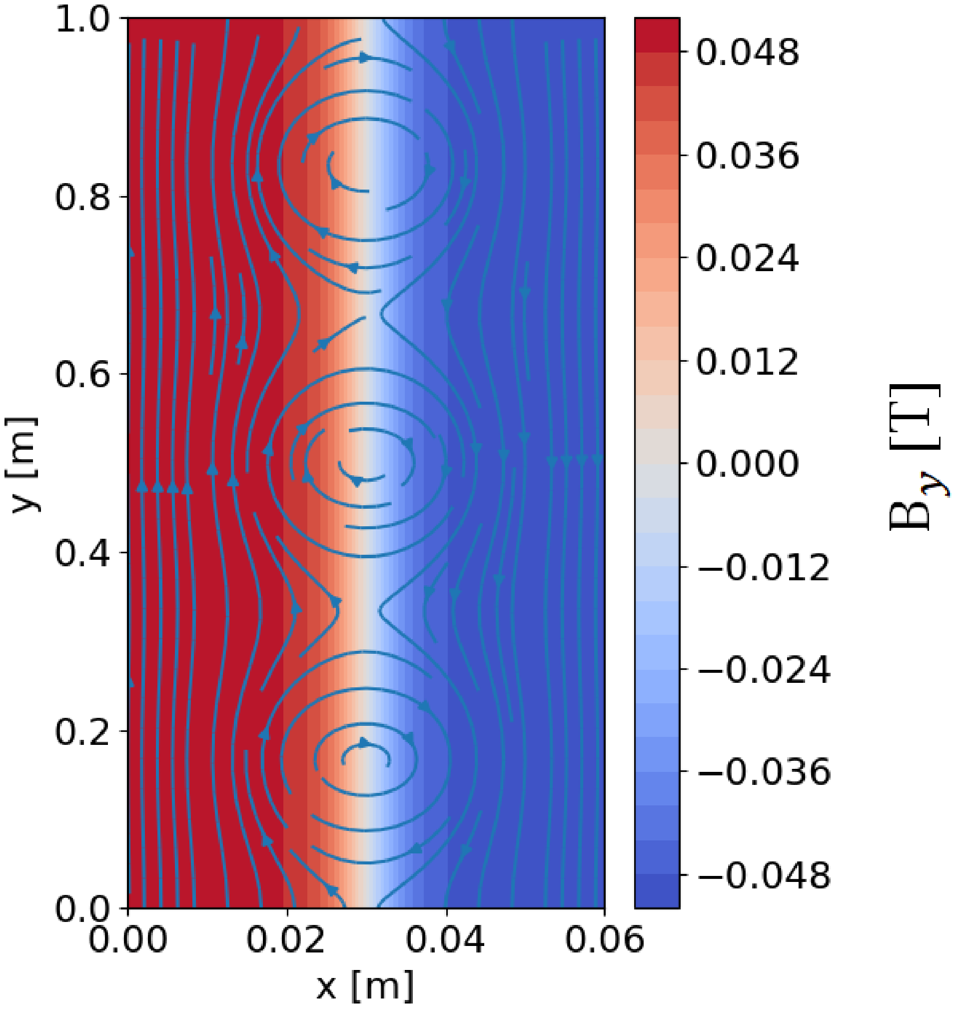

Figure A.1: Poloidal magnetic field computed from the Fadeev equilibrium. The red and blue colors represent the positive and negative magnetic fields. The black line indicates the magnetic field line.

direction. $L_x = 0.06\,\mathrm{m}$ and $L_y = 1\,\mathrm{m}$ are the lengths of the simulation box in each direction. The potential at the two bounded boundaries $x = 0$ and $x = L_x$ is assumed to be zero. The constant magnetic field B_z is considered

a) Particle density

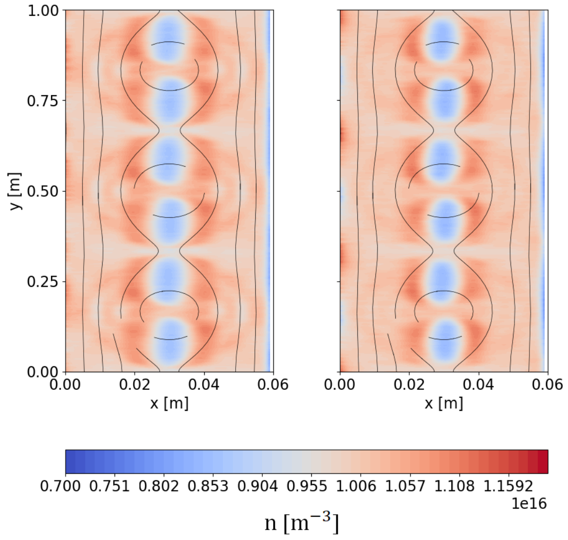

b) Radial flux

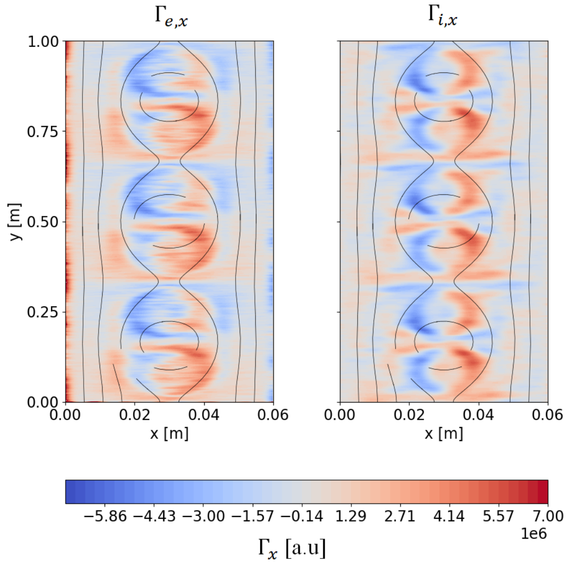

Figure A.2: Particle density and radial flux in the simulation.The black line indicates the magnetic field line. Ions and electrons show similar impacts on the magnetic island effects.

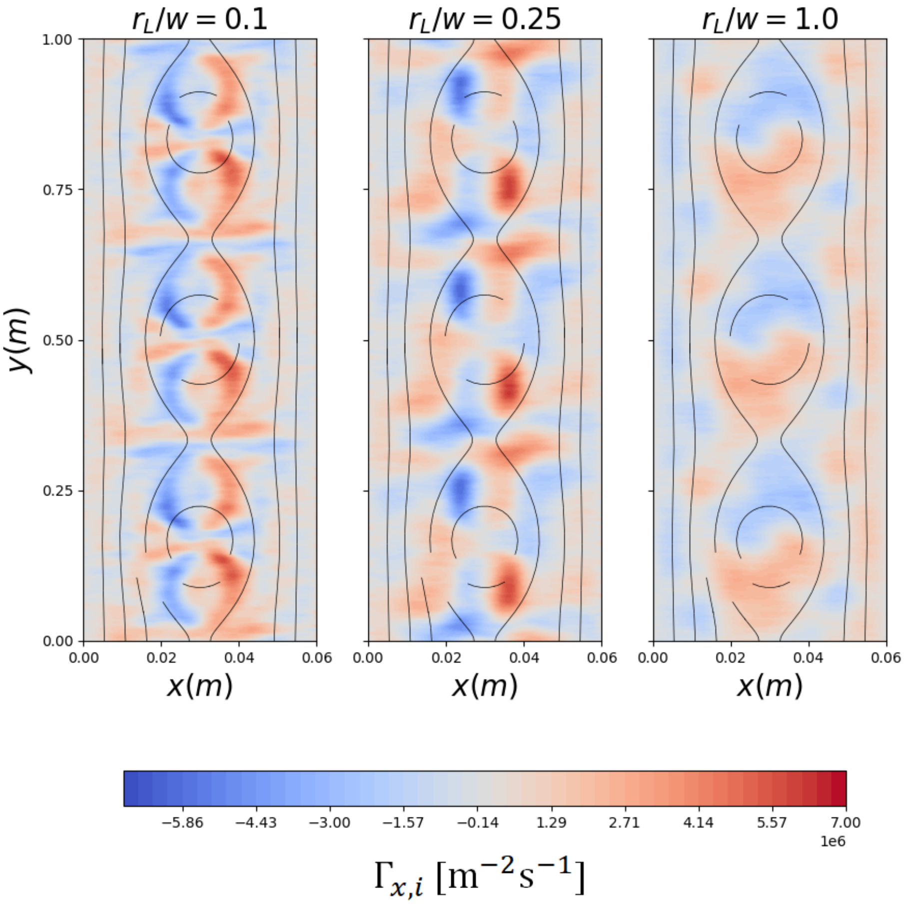

Figure A.3: Radial flux of ion with different ratios of Larmor radius and magnetic island lengths. Ions having large Larmor radius are weakly affected by the magnetic island.

to avoid the drift effects. The magnetic fields B_x and B_y are modified from the Fadeev formula to provide three magnetic islands at the center of the simulation box, as displayed in Fig. A.1.

At the initial stage, the particle density and temperature are constant, are the same for both electrons and ions, and are set as $n_{s,\mathrm{LCFS}} = 10^{16}\, m^{-3}$ ans $kT_0 = 1\,\mathrm{keV}$. Because ions have larger Larmor radius than electrons, ions are more sensitive to the change in the magnetic field. We mainly concentrate on the ion transport in the magnetic island. Adopting the large magnetic field $B_z = 1\,\mathrm{T}$, the ion Larmor radius is much smaller than the width of the magnetic island. The ratio of ion Larmor radius to the magnetic island width $r_{L,i}/w$ is less than 0.1 in this case. The movement of the ions due to magnetic island effects is similar to that of the electrons. As illustrated in Fig. A.2, the density and flux of the ions show a similar tendency to those of the electrons. At the center of the simulation box, where the magnetic field is the smallest, the Larmor radius of particles in this region is the largest. Once making the gyro motion, these large Larmor-radius particles can shift to the left or right region with a large displacement. Because of the strong magnetic field in the boundaries of the island, these particles are trapped in this location. Therefore, the particle density in the boundaries of the island is higher than that in the center of the magnetic island.

Fig. A.3 shows the ion density when different ratios of ion Larmor radius to magnetic island width are considered. Ions having larger Larmor radius might escape from the magnetic island when composing the circular motion. The magnetic island cannot be effective when trapping the large Larmor-radius particles. Therefore, the ions having large Larmor radius are weakly affected by the magnetic island.

Acknowledgment

The work is the result during of five years of study at the National Institute for Fusion Science (NIFS), Toki, Japan. Throughout the work on this research, I have received a great deal of support and assistance. I take this opportunity to express my deep appreciation to all those who helped me complete my research work.

First of all, this work would not have been possible without the financial support of the Monbukagakusho scholarship from the Japanese government.

This doctoral thesis was under the guidance of my supervisors: Prof. Yasuhiro Suzuki, Prof. Hiroaki Ohtani, Prof. Hiroki Hasegawa, and Prof. Toseo Moritaka. I was extremely fortunate to work under their supervision. Without their guidance, this work cannot be completed.

I would like to express my deepest gratitude to my supervisor, Prof. Yasuhiro Suzuki for giving me a great opportunity to work with him and for supporting me to finish my doctoral research. He always provides useful ideas for completing my research, improving the presentations, writing the papers, and preparing this doctoral thesis. His professional knowledge and excellent guidance lead me to go in the correct way for getting the Ph.D. Thank for being patient and motivating me during the study. Besides, I am also thankful for sharing the helpful experience of my living in Japan. I appreciate all his contributions of time, ideas, patience, and guidance to make my research work possible. I was extremely fortunate to work under his supervision.

I am grateful to my co-supervisor, Prof. Hiroaki Ohtani for support and insightful discussions during the last year of my study. His fruitful suggestions help to improve the quality of my research work. Thank for always giving the key comments related to the physics consideration to upgrade my work to more informatics, valuable, and precise.

Great gratitude also goes to my vice supervisors, Prof. Hiroki Hasegawa, and Prof. Toseo Moritaka for all of the guidance through each stage of the process. Their guidance led me to the field of study of particle simulation. Thank for checking my program and helping me with how to perform the code on the supercomputer. The code was not well optimized and correctly ran without their powerful suggestions. I am so thankful for always pointing out my mistakes, and giving professional discussions and comments for analyzing the physics phenomena based on the modeling results.

I would also like to give a special thanks to Prof. Seiji Ishiguro and Dr. Gakushi Kawamura for all of their suggestions regarding the code development. Without their suggestions and comments, this works would not have been performed correctly.

I would like to extend my acknowledgment to professors in NIFS for teaching interesting lectures on plasma physics, computer programming, and scientific English writing. I also express my deep thank to the administrative staff of both NIFS and SOKENDAI with whom I interacted during my work. Thank for providing the best environment for my research.

I wish also to thank the colleagues I met in this country. Many thanks to my tutors, Junki Morimoto and Toyo Yamasita for their help in dealing with the work related to my daily life in Japan. My sincere thanks go to my colleagues, Dr. Nilam Nimavat, Dr. Yuki Goto, Dr. Yasuaki Haba, Dr. Jie Huang, Dr. Bing Ma, Dr. Kawase Hiroki, Engrhyt Rattanawongnara, Hanzheng Li. Thank you for sharing wonderful moments during my study in Japan.

Last but not least, I would like to express my gratitude to my grandparents, parents, sisters, and relatives for all the love and encouragement. Thank for supporting and motivating me to pursue this journey.

References

[1] Todd E Evans, Richard A Moyer, Keith H Burrell, Max E Fenstermacher, Ilon Joseph, Anthony W Leonard, Thomas H Osborne, Gary D Porter, Michael J Schaffer, Philip B Snyder, et al. Edge stability and transport control with resonant magnetic perturbations in collisionless tokamak plasmas. nature physics, 2(6):419–423, 2006.

[2] G Ciaccio, O Schmitz, SS Abdullaev, H Frerichs, M Agostini, P Scarin, G Spizzo, N Vianello, and RB White. Plasma edge transport with magnetic islands—a comparison between tokamak and reversed-field pinch. Nuclear fusion, 54(6):064008, 2014.

[3] A Wingen and KH Spatschek. Influence of different ded base mode configurations on the radial electric field at the plasma edge of textor. Nuclear fusion, 50(3):034009, 2010.

[4] JW Coenen, O Schmitz, B Unterberg, M Clever, MA Jakubowski, U Samm, B Schweer, H Stoschus, M Tokar, et al. Rotation and radial electric field in the plasma edge with resonant magnetic perturbation at textor. Nuclear fusion, 51(6):063030, 2011.

[5] RD Hazeltine, P Helander, and Peter J Catto. Plasma transport near the separatrix of a magnetic island. Physics of Plasmas, 4(8):2920–2927, 1997.

[6] A Bañón Navarro, L Bardóczi, TA Carter, F Jenko, and TL Rhodes. Effect of magnetic islands on profiles, flows, turbulence and transport

in nonlinear gyrokinetic simulations. Plasma Physics and Controlled Fusion, 59(3):034004, 2017.

[7] Y Xu, RR Weynants, S Jachmich, M Van Schoor, M Vergote, Peter Peleman, MW Jakubowski, M Mitri, D Reiser, B Unterberg, et al. Influence of the static dynamic ergodic divertor on edge turbulence properties in textor. Physical review letters, 97(16):165003, 2006.

[8] MZ Tokar, TE Evans, R Singh, and B Unterberg. Particle transfer in edge transport barrier with stochastic magnetic field. Physics of plasmas, 15(7):072515, 2008.

[9] DJ Ward. Lh transition theories and theory of h-mode. Plasma Physics and Controlled Fusion, 38(8):1201, 1996.

[10] KH Burrell, EJ Doyle, P Gohil, RJ Groebner, J Kim, RJ La Haye, LL Lao, RA Moyer, TH Osborne, WA Peebles, et al. Role of the radial electric field in the transition from l (low) mode to h (high) mode to vh (very high) mode in the diii-d tokamak. Physics of plasmas, 1(5):1536–1544, 1994.

[11] KH Burrell. Effects of e× b velocity shear and magnetic shear on turbulence and transport in magnetic confinement devices. Physics of Plasmas, 4(5):1499–1518, 1997.

[12] Guido Van Oost. Importance of radial electric fields for magnetically confined plasmas. Computational nanotechnology, (1):82–90, 2018.

[13] Katsumi Ida. Experimental studies of the physical mechanism determining the radial electric field and its radial structure in a toroidal plasma. Plasma Physics and Controlled Fusion, 40(8):1429, 1998.

[14] K Kamiya, K Ida, M Yoshinuma, C Suzuki, Y Suzuki, M Yokoyama, LHD Experiment Group, et al. Characterization of edge radial electric field structures in the large helical device and their viability for determining the location of the plasma boundary. Nuclear Fusion, 53(1):013003, 2012.

[15] Yasuhiro Suzuki, K Ida, K Kamiya, M Yoshinuma, S Sakakibara, KY Watanabe, H Yamada, LHD Experiment Group, et al. 3d plasma response to the magnetic field structure in the large helical device. Nuclear Fusion, 53(7):073045, 2013.

[16] Y Suzuki, K Ida, K Kamiya, M Yoshinuma, H Tsuchiya, S Inagaki, S Sakakibara, KY Watanabe, Y Narushima, S Ohdachi, et al. Investigation of radial electric field in the edge region and magnetic field structure in the large helical device. Plasma Physics and Controlled Fusion, 55(12):124042, 2013.

[17] XZ Yang, BZ Zhang, AJ Wootton, PM Schoch, B Richards, D Baldwin, DL Brower, GG Castle, RD Hazeltine, JW Heard, et al. The space potential in the tokamak text. Physics of Fluids B: Plasma Physics, 3(12):3448–3461, 1991.

[18] V Rozhansky. Drifts, currents, and radial electric field in the edge plasma with impact on pedestal, divertor asymmetry and rmp consequences. Contributions to Plasma Physics, 54(4-6):508–516, 2014.

[19] Y Kikuchi, MFM De Bock, KH Finken, M Jakubowski, R Jaspers, HR Koslowski, A Kraemer-Flecken, M Lehnen, Y Liang, G Matsunaga, et al. Forced magnetic reconnection and field penetration of an externally applied rotating helical magnetic field in the textor tokamak. Physical review letters, 97(8):085003, 2006.

[20] M Bécoulet, G Huysmans, X Garbet, E Nardon, D Howell, A Garofalo, M Schaffer, T Evans, K Shaing, A Cole, et al. Physics of penetration of resonant magnetic perturbations used for type i edge localized modes suppression in tokamaks. Nuclear Fusion, 49(8):085011, 2009.

[21] E Nardon, P Tamain, M Bécoulet, G Huysmans, and FL Waelbroeck. Quasi-linear mhd modelling of h-mode plasma response to resonant magnetic perturbations. Nuclear Fusion, 50(3):034002, 2010.

[22] T Takizuka, K Shimizu, N Hayashi, M Hosokawa, and M Yagi. Two-dimensional full particle simulation of the flow patterns in the scrape-off-layer plasma for upper-and lower-null point divertor configurations in tokamaks. Nuclear fusion, 49(7):075038, 2009.

[23] T Takizuka, M Hosokawa, and K Shimizu. Two-dimensional particle simulation of the flow control in sol and divertor plasmas. Journal of nuclear materials, 313:1331–1334, 2003.

[24] T Takizuka and M Hosokawa. Two-dimensional full particle simulation of the formation of electrostatic field in a tokamak plasma. In 11th IAEA Technical Meeting on H-mode Physics and Transport Barriers, Tsukuba, 2007.

[25] T Takizuka. Development of the parasol code and full particle simulation of tokamak plasma with an open-field sol-divertor region using parasol. Plasma Science and Technology, 13(3):316, 2011.

[26] Christine Charles. Plasmas for spacecraft propulsion. Journal of Physics D: Applied Physics, 42(16):163001, 2009.

[27] Richard A Gerwin. Integrity of the plasma magnetic nozzle. Technical report, 2009.

[28] Jeffrey P Freidberg. Plasma physics and fusion energy. Cambridge university press, 2008.

[29] Peter C Stangeby et al. The plasma boundary of magnetic fusion devices, volume 224. Institute of Physics Pub. Philadelphia, Pennsylvania, 2000.

[30] Hong-Fei Chen, Hong Zou, Wei-Hong Shi, Ji-Qing Zou, Xiang-Qian Yu, and Zuo Xiao. High energy charged particle experiment–a payload proposal to kuafu-b mission. Advances in space research, 44(1):39–45, 2009.

[31] Tsoline Mikaelian. Spacecraft charging and hazards to electronics in space. arXiv preprint arXiv:0906.3884, 2009.

[32] Phillip C Anderson. Characteristics of spacecraft charging in low earth orbit. Journal of Geophysical Research: Space Physics, 117(A7), 2012.

[33] LW Townsend. Overview of active methods for shielding spacecraft from energetic space radiation. Physica Medica, 17:84–85, 2001.

[34] SI Krasheninnikov, AS Kukushkin, and AA Pshenov. Divertor plasma detachment. Physics of Plasmas, 23(5):055602, 2016.

[35] ME Rensink and TD Rognlien. Plasma heat-flux dispersal for act1 divertor configurations. Fusion Science and Technology, 67(1):125–141, 2015.

[36] T Takizuka, K Tani, M Azumi, and K Shimizu. Particle simulation of divertor plasma. Journal of Nuclear Materials, 128:104–110, 1984.

[37] TW Petrie, SL Allen, ME Fenstermacher, RJ Groebner, CT Holcomb, E Kolemen, RJ La Haye, CJ Lasnier, AW Leonard, TC Luce, et al. Application of the radiating divertor approach to innovative tokamak divertor concepts. Journal of Nuclear Materials, 463:1225–1228, 2015.

[38] O Schmitz, M Becoulet, P Cahyna, TE Evans, Y Feng, H Frerichs, A Loarte, RA Pitts, D Reiser, ME Fenstermacher, et al. Three-dimensional modeling of plasma edge transport and divertor fluxes during application of resonant magnetic perturbations on iter. Nuclear fusion, 56(6):066008, 2016.

[39] GF Matthews. Plasma detachment from divertor targets and limiters. Journal of nuclear materials, 220:104–116, 1995.

[40] TW Petrie, TE Evans, NH Brooks, ME Fenstermacher, JR Ferron, CT Holcomb, B Hudson, AW Hyatt, TC Luce, CJ Lasnier, et al. Results from radiating divertor experiments with rmp elm suppression and mitigation. Nuclear Fusion, 51(7):073003, 2011.

[41] AJ Thornton, A Kirk, P Cahyna, IT Chapman, JR Harrison, Yueqiang Liu, MAST Team, et al. The effect of resonant magnetic perturba-

tions on the divertor heat and particle fluxes in mast. Nuclear Fusion, 54(6):064011, 2014.

[42] M Kobayashi, R Seki, S Masuzaki, S Morita, HM Zhang, Y Narushima, H Tanaka, K Tanaka, T Tokuzawa, M Yokoyama, et al. Impact of a resonant magnetic perturbation field on impurity radiation, divertor footprint, and core plasma transport in attached and detached plasmas in the large helical device. Nuclear Fusion, 59(9):096009, 2019.

[43] M Rack, L Zeng, P Denner, Y Liang, A Wingen, KF Gan, L Wang, FK Liu, B Shen, BN Wan, et al. Modelling of lhw-induced helical current filaments on east: study of an alternative method of applying rmps. Nuclear fusion, 54(6):064016, 2014.

[44] Y Liang, XZ Gong, KF Gan, E Gauthier, L Wang, M Rack, YM Wang, L Zeng, P Denner, A Wingen, et al. Magnetic topology changes induced by lower hybrid waves and their profound effect on edge-localized modes in the east tokamak. Physical review letters, 110(23):235002, 2013.

[45] John P Verboncoeur, Maria Virginia Alves, Vahid Vahedi, and Charles Kennedy Birdsall. Simultaneous potential and circuit solution for 1d bounded plasma particle simulation codes. Journal of Computational Physics, 104(2):321–328, 1993.

[46] Y Miyake, CM Cully, H Usui, and H Nakashima. Plasma particle simulations of wake formation behind a spacecraft with thin wire booms. Journal of Geophysical Research: Space Physics, 118(9):5681–5694, 2013.

[47] Yohei Miyake and Hideyuki Usui. New electromagnetic particle simulation code for the analysis of spacecraft-plasma interactions. Physics of Plasmas, 16(6):062904, 2009.

[48] Raed Kafafy and Joseph Wang. A hybrid grid immersed finite element particle-in-cell algorithm for modeling spacecraft–plasma interactions. IEEE transactions on plasma science, 34(5):2114–2124, 2006.

[49] Charles K Birdsall and A Bruce Langdon. Plasma physics via computer simulation. CRC press, 2004.

[50] D Tskhakaya, K Matyash, R Schneider, and F Taccogna. The particle-in-cell method. Contributions to Plasma Physics, 47(8-9):563–594, 2007.

[51] Hong Qin, Shuangxi Zhang, Jianyuan Xiao, Jian Liu, Yajuan Sun, and William M Tang. Why is boris algorithm so good? Physics of Plasmas, 20(8):084503, 2013.

[52] William S Lawson. Particle simulation of bounded 1d plasma systems. Journal of Computational Physics, 80(2):253–276, 1989.

[53] Guang-Hong Lu, Long Cheng, Kameel Arshad, Yue Yuan, Jun Wang, Shaoyang Qin, Ying Zhang, Kaigui Zhu, Guang-Nan Luo, Haishan Zhou, et al. Development and optimization of step—a linear plasma device for plasma-material interaction studies. Fusion Science and Technology, 71(2):177–186, 2017.

[54] Yuki Hayashi, Noriyasu Ohno, Shin Kajita, and Hirohiko Tanaka. Plasma flow in peripheral region of detached plasma in linear plasma device. Physics of Plasmas, 23(1):012511, 2016.

[55] Yunfeng Liang, XZ Gong, KF Gan, E Gauthier, L Wang, M Rack, YM Wang, L Zeng, P Denner, A Wingen, et al. Magnetic topology changes induced by lower hybrid waves and their profound effect on edge-localized modes in the east tokamak. Physical review letters, 110(23):235002, 2013.

[56] AW Leonard. Plasma detachment in divertor tokamaks. Plasma Physics and Controlled Fusion, 60(4):044001, 2018.

[57] GM Staebler. Divertor bias experiments. Journal of nuclear materials, 220:158–170, 1995.

[58] GM Staebler. Transport modelling of divertor bias experiments. Nuclear fusion, 31(4):729, 1991.

[59] BJ Xiao, Y Guo, and G Calabro. First quasi-snwoflake divertor experiment on east. Technical report, 2015.

[60] K Nanbu and Shigeru Yonemura. Weighted particles in coulomb collision simulations based on the theory of a cumulative scattering angle. Journal of Computational Physics, 145(2):639–654, 1998.

[61] G Park, Choong-Seock Chang, I Joseph, and RA Moyer. Plasma transport in stochastic magnetic field caused by vacuum resonant magnetic perturbations at diverted tokamak edge. Physics of Plasmas, 17(10):102503, 2010.

[62] B Unterberg, C Busch, M De Bock, JW Coenen, KH Finken, MW Jakubowski, Y Kikuchi, A Krämer-Flecken, M Lehnen, U Samm, et al. Impact of stochastic magnetic fields on plasma rotation and radial electric fields in the plasma edge of the tokamak textor. Journal of nuclear materials, 363:698–702, 2007.

[63] VM Fadeev, IF Kvabtskhava, and NN Komarov. Self-focusing of local plasma currents. Nuclear fusion, 5(3):202, 1965.

[64] Hubert Baty. On the sweet-parker model for incompressible visco-resistive magnetic reconnection in two dimensions associated to ideal magnetohydrodynamic instabilities. arXiv preprint arXiv:2201.01135, 2022.